Detection of beta decay in laser oriented trapped radioactive isotopes for the MORA project

Nishu Goyal

Normandie Université

UNIVERSITÉ CAEN NORMANDIE

THÈSE

Pour obtenir le diplôme de doctorat

Spécialité PHYSIQUE

Préparée au sein de l'Université de Caen Normandie

Detection of beta decay in laser oriented trapped radioactive isotopes for the MORA project

Présentée et soutenue par
NISHU GOYAL

Thèse soutenue le 22/05/2023 devant le jury composé de		
M. BERTRAM BLANK	Directeur de recherche au CNRS, UNIVERSITE BORDEAUX 1 SCIENCES ET TECHNOLOGIE	Rapporteur du jury
MME SARAH NAIMI	Directeur de recherche, Labo. de Physique des 2 Infinis Irène Joliot-Curie	Rapporteur du jury
M. PIERRE DELAHAYE	Chargé de recherche HDR, 14 GANIL de CAEN	Membre du jury
MME FAIROUZ HAMMACHE	Chargé de recherche au CNRS, UNIVERSITE PARIS 11 PARIS-SUD	Membre du jury
M. ETIENNE LIENARD	Professeur des universités, Université de Caen Normandie	Président du jury
M. FRANCOIS DE OLIVEIRA SANTOS	Directeur de recherche au CNRS, 14 GANIL de CAEN	Directeur de thèse

Thèse dirigée par FRANCOIS DE OLIVEIRA SANTOS (Grand accélérateur national d'ions lourds)

ED 591 PSIME

GANIL laboratoire commun CEA/DRF spiral2 CNRS/IN2P3

Table of Content

List of Figures

Acknowledgement

The time has finally arrived to pack my bags and explore new horizons. A significant amount of time has passed since I arrived at GANIL, and it still seems like yesterday. Undoubtedly I made a family with no blood relations.
I want to express my deepest gratitude and appreciation to all those who have supported me throughout my journey of pursuing my Ph.D. degree. This thesis work would not have been possible otherwise.

First and foremost, I sincerely thank my thesis supervisors, M. Francois de OLIVEIRA, and M. Pierre DELAHAYE, for their invaluable guidance, and continuous support. Their open-door policy and genuine interest in my well-being have fostered a positive and nurturing environment. Their encouragement during moments of doubt and their belief in my abilities have been genuinely inspiring. I am forever grateful for their mentorship and encouragement throughout these years. I would also like to express my sincere gratitude to Mme. Christelle STODEL, who despite her major responsibilities towards the physics group of GANIL, always stood up for my betterment.

I am immensely grateful to the members of my thesis committee, Mme. Sarah NAIMI, M. Bertram BLANK, Mme. Fairouz HAMMACHE and M. Etienne LIENARD, for their valuable insights and constructive criticism, which helped me to strengthen my arguments and improve the clarity of my writing, which has significantly contributed to improving my manuscript.

I extend my heartfelt appreciation to the GANIL community for creating an enriching environment that fostered my growth as a student. A lot of appreciation for my fellow researchers and colleagues for their engaging discussions with a cup of coffee to make this journey all the more fulfilling.

My gratitude extends to my family to Er. Rajesh K. GUPTA, whose support, understanding, and love have constantly motivated and strengthened me. I am forever grateful for your presence in my life.

I warmly thank my extended family, who ensured my well-being despite their busy schedules. Even in moments full of frustration, they were always there to provide words of reassurance and motivate me to push forward. Thanks a lot to Rikel CHAKMA, Mukul DHIMAN, Louis M. MOTILLA, Neeraj KUMAR, Rojeeta DEVI, Abhilasha SINGH, Saba ANSARI, and my best friend/critic Bernadette REBEIRO for being a constant source of encouragement.

No words are enough to thank my partner Alvaro Adrian. I want to acknowledge his sacrifices, often putting aside his own aspiration. I am indebted to your detailed feedback on countless drafts of this manuscript. Your insightful suggestions have undoubtedly improved the quality of my work. I am fortunate to have such an incredible individual by my side who has supported me not just academically but emotionally throughout this long journey.

Additionally, I would like to express my gratitude to the funding agencies to support my research financially. Their support enabled me to achieve experimental objectives, attend conferences, and access necessary resources, which was vital in completing this thesis.

Last, I extend my sincerest gratitude to all the participants who willingly contributed their time and expertise to the MORA project specially the LPC and the IGISOL group. Their willingness to participate and share their experiences and knowledge has been integral in this process.

In conclusion, I would like to acknowledge the collective efforts of all those mentioned above, as well as anyone else who has played a part, however small, in shaping this thesis. Your support and encouragement have been invaluable, and your contributions humble me. Thank you all for being an integral part of my Ph.D. journey and helping me reach this significant milestone.

Introduction

One of modern physics's greatest challenges is figuring out why the Universe we see is made entirely out of matter and not antimatter. According to the predominant models, the Universe was created in the so-called "Big Bang" from pure energy. It is commonly considered that the Big Bang and its after-effects created equal numbers of particles and its counterpart. Yet, today's universe tells us a different story.

The fact that one cannot explain the dominance of matter over antimatter is one of the significant shortcomings of the Standard Model (SM). To mention only some of the *SM*'s other most prominent shortcomings, it describes only three of the four fundamental interactions. Indeed, the theory of gravitation is not yet defined at a quantum level. The *SM* has 19 free parameters, such as the number of generations of elementary particles, and their masses are not predicted but are based on experimental observations. However, the model has stayed almost unchanged for more than thirty years. Its unprecedented predictive power makes it the most robust theory to describe elementary particles and how they are and the way they interact.

The only quantity in the *SM* that distinguishes between matter and antimatter is the *CP*-violating phase in the *Cabbibo Kobayashi Maskawa (CKM) matrix* [7], and it does not appear to be enough to explain the observed asymmetry. On the other hand, many physics models beyond the *SM* contain new sources of *CP* violation. In some cases, these can be enough to account for the significant matter-antimatter asymmetry. The discovery of *New Physics* (NP) at colliders and many new experiments searching for *CP* violation may provide clues to this mystery.

This thesis work is part of the experimental tests at low energy of the *SM*. The whole community now eventually knows that it is not the ultimate theory since it has been recently challenged thanks to the observation of neutrino oscillations. The *SM* undergoes two types of tests: high-energy and low-energy. In the first case, the goal is to reach the highest possible energy to produce new particles in lepton (e^+e^-) or hadronic (proton-proton) collisions. In the second case, precision measurements are performed in the context of nuclear processes or rare decays to show a significant difference concerning the *SM* predictions.
We can cite some significant successes of this theory with the discovery of the weak interaction in 1973 [8]. The mediator of the strong interaction in 1979 [9], and finally, the bosons of the weak interaction (W^+, W^-, Z_0) in 1983 [10]. Recently, the *Higgs-boson* was discovered, confirming the mechanism that bears its name and gives mass to particles.

The study of β decays in nuclei is among the best probes of weak interaction. Indeed, in the kinematics description, different correlation parameters appear and have

a value defined by the *SM*. Precision measurements allow us to test the limits of these predictions and assign certain constraints to them. One of the great successes of testing these correlations is the V-A theory [11], which describes the weak interaction and postulates that only vector and axial-vector currents exist. Other currents, the scalar, pseudo-scalar, and tensor currents, are called exotic and vanish in the frame of the *SM*. In full generality (i.e., beyond the *SM*), they are allowed by the invariance of the general Hamiltonian of the interaction by low energy Lorentz transformation, for which the precision of the constraints is not yet sufficient to exclude them definitively.

This work aims to study the detection configuration utilized for the precision measurement of a correlation that constrains or discovers new sources of *CP* violation. The setup of *MORA*, installed at the *IGISOL* line of Jyväskylä Accelerator Laboratory in Finland, uses an innovative technique: a transparent Paul trap, which is an optimized trapping setup inspired by the one of LPCTrap [12], where ions are confined in a small volume, almost at rest, and polarized in-situ by advanced techniques of laser manipulation of their hyperfine transitions.

We propose to measure the triple *D* correlation parameter, which is in the form of $\overrightarrow{J} \cdot (\overrightarrow{p_e} \times \overrightarrow{p_\nu})$ with $\overrightarrow{p_e}$ and $\overrightarrow{p_\nu}$ being respectively the momenta of the (e^- and $\bar{\nu}$) or (e^+ and ν) and $\overrightarrow{J}$ the nuclear spin. The *D* correlation violates time reversal. While such violation has been predicted to occur in the *SM* via the quark mixing mechanism, experimental constraints are much lower than needed to explain the observed matter-antimatter asymmetry [13]. There is a large window where *D* and *R* [14]correlations, and neutron-EDM searches can contribute to the search for other sources of *CP* violation at a much higher level [15–17]. The best constraints on *D* come from the neutron decay [18, 19]. Lower constraints have been obtained from a compilation of experiments probing ^{19}Ne decay [20].

With the expected beam production rates from the IGISOL facility of Jyväskylä and the future upgraded SPIRAL facility at GANIL, an experiment aiming at D-correlation measurement with an unprecedented sensitivity of $< 10^{-4}$ is planned. We commissioned the apparatus and attempted the first proof-of-principle of the laser polarization method employing the laser systems of *IGISOL* at JYFL, together with an optimized trapping and detection setup, in 2022.

The structure of this thesis work is the following:

- We first focused on studying the theoretical context and comprehensively describing the *MORA* Project in **chapter 1** . Progressively we focused on the detection setup consisting of beta and recoil ion detectors for measuring the *D* parameter and a set of annular segmented silicon detectors for polarization degree monitoring/measurement.

- The so-called RIDE: Recoil Ion DEtectors are thoroughly discussed in **chapter 2** , including their assembly, characterization, and applied methods for detector image reconstruction to obtain the Position resolution. We also discussed the test methodology and acquired results concerning the absolute Efficiency of the detection setup.

- **Chapter 3** is committed to annular silicon detectors and their characterization with offline radioactive sources at our home ground in GANIL before the final move of the detection system to the *IGISOL* facility.

- In **chapter 4**, we describe the progress made during the first months following the installation of the *MORA* setup at the *IGISOL* facility during the commissioning experiments.
  Starting with a short overview of ion beam manipulation at *IGISOL*, Chapter 4 focuses on each contributing parameter and the advancement of the detection setup in the first two allocated beam times at the beginning of 2022. Taking advantage of the first data recorded during the last run, we attempted to achieve a preliminary estimate of the degree of polarization (P). This first investigation estimates the envisaged precision value for forthcoming measurements. Future perspectives are also discussed concerning the progress cited during the initial phase of experiments with *MORA*.

- Finally, we documented a **conclusion** for this thesis work.

Introduction (Français)

L'un des plus grands défis de la physique moderne est de comprendre pourquoi l'Univers que nous voyons est entièrement constitué de matière et non d'antimatière. Selon les modèles prédominants,l'Univers a été créé dans ce que l'on appelle le "Big Bang" à partir d'énergie pure. On considère généralement que le Big Bang et ses conséquences ont créé un nombre égal de particules et de son équivalent d'antiparticules. Pourtant, l'univers actuel nous raconte une histoire différente.

Le fait que l'on ne puisse pas expliquer la prédominance de la matière sur l'antimatière est l'une des principales lacunes du modèle standard (MS). Pour ne citer que quelques des autres lacunes les plus importantes du modèle standard, il ne décrit que trois des quatre interactions fondamentales. En effet, la théorie de la gravitation n'est pas encore définie au niveau quantique. Le MS comporte 19 paramètres libres, tels que le nombre de générations de particules élémentaires, et leurs masses ne sont pas prédites mais basées sur des observations expérimentales. Cependant, le modèle est resté pratiquement inchangé depuis plus de trente ans. Son pouvoir prédictif sans précédent en fait la théorie la plus robuste pour décrire les particules élémentaires, leur nature et leurs interactions.

La seule quantité dans le MS qui distingue la matière de l'antimatière est la phase violant CP dans la matrice de Cabbibo Kobayashi Maskawa (CKM) [7], et elle ne semble pas suffisante pour expliquer l'asymétrie observée. D'autre part, de nombreux modèles physiques au-delà du MS contiennent de nouvelles sources de violation de CP. Dans certains cas, ces sources peuvent suffire à expliquer l'importante asymétrie matière-antimatière. La découverte de la Nouvelle Physique (NP) dans les collisionneurs et de nombreuses nouvelles expériences à la recherche de la violation de CP peuvent fournir des indices sur ce mystère.

Ce travail de thèse fait partie des tests expérimentaux à basse énergie de la nouvelle physique. L'ensemble de la communauté sait désormais qu'il ne s'agit pas de la théorie ultime puisqu'elle a été récemment remise en question grâce à l'observation des oscillations des neutrinos. Le MS subit deux types de tests : à haute énergie et à basse énergie. Dans le premier cas, l'objectif est d'atteindre la plus haute énergie possible pour produire de nouvelles particules leptoniques (e^+e^-) ou hadroniques (proton-proton). Dans le second cas, des mesures de précision sont effectuées dans le contexte de processus nucléaires ou de désintégrations rares afin de montrer une différence significative par rapport aux prédictions du MS.
On peut citer quelques succès significatifs de cette théorie avec la découverte de l'interaction faible en 1973 [8]. Le médiateur de l'interaction forte en 1979 [9], et enfin, des bosons de l'interaction faible (W^+, W^-, Z^0) en 1983 [10]. Récemment, le boson de Higgs- a été découvert, confirmant le mécanisme qui porte son nom et qui donne une

masse aux particules.

L'étude des désintégrations β dans les noyaux est l'une des meilleures sondes de l'interaction faible. En effet, dans la description cinématique, différents paramètres de corrélation apparaissent et ont une valeur définie par le MS. Des mesures de précision nous permettent de tester les limites de ces prédictions et de leur attribuer certaines contraintes. L'un des grands succès des tests de ces corrélations est la théorie V-A [11], qui décrit l'interaction faible et postule que seuls les vecteurs et les axes sont pris en compte. postule que seuls les courants vectoriels et vectoriels axiaux existent. Les autres courants, le scalaire, pseudo-scalaires et tensoriels, sont dits exotiques et s'évanouissent dans le cadre du MS. En général (c'est-à-dire au-delà du modèle SM), ils sont autorisés par l'invariance de l'hamiltonien général de l'interaction par le modèle MS. l'hamiltonien général de l'interaction par la transformation de Lorentz à basse énergie, pour laquelle la précision des contraintes n'est pas suffisante. pour laquelle la précision des contraintes n'est pas encore suffisante pour les exclure définitivement.

Ce travail vise à étudier la configuration de détection utilisée pour la mesure de précision d'une corrélation qui contraint ou découvre de nouvelles sources de violation du CP. Le dispositif de MORA, installé sur la ligne IGISOL du laboratoire de l'accélérateur de Jyväskylä en Finlande, utilise une technique innovante : un piège de paul transparent, qui est un dispositif de piégeage optimisé inspiré de celui de LPCTrap [12], où les ions sont confinés dans un petit volume, presque au repos, et polarisés in situ grâce à des techniques avancées de manipulation laser de leur structure hyperfine.

Nous proposons de mesurer le paramètre de corrélation triple D, qui se présente sous la forme suivante $\overrightarrow{J} \cdot (\overrightarrow{p_e} \times \overrightarrow{p_\nu})$ avec $\overrightarrow{p_e}$ and $\overrightarrow{p_\nu}$ étant respectivement les moments du (e^- & $\bar{\nu}$) ou du (e^+ & ν) et $\overrightarrow{J}$ le spin nucléaire. La corrélation D viole le renversement du temps. Alors que bien qu'il ait été prédit qu'une telle violation se produise dans le MS via le mécanisme de mélange des quarks, les contraintes expérimentales sont bien inférieures à ce qui est nécessaire pour expliquer l'asymétrie observée entre la matière et l'antimatière [13]. Il existe une large fenêtre où les corrélations D et R [14], et les recherches de n-EDM peuvent contribuer à la recherche d'autres sources de violation de CP à un niveau d'aujourd'hui beaucoup plus élevé [15–17]. Les meilleures contraintes sur D proviennent de la désintégration des neutrons [18,19]. Des contraintes plus faibles ont été obtenues à partir d'une compilation d'expériences sondant la désintégration de ^{19}Ne [20].

Avec les taux de production de faisceaux attendus de l'installation $IGISOL$ de Jyväskylä et de la future installation SPIRAL améliorée, il est possible d'obtenir des données sur la désintégration des neutrons. De Jyväskylä et de la future installation SPIRAL au GANIL, une expérience visant à mesurer la corrélation D avec une sensibilité sans précédent $<10^{-4}$ est prévue. Nous avons mis en service l'appareil et tenté la première preuve de principe de la méthode de polarisation laser en utilisant les systèmes laser d'IGISOL au JYFL, ainsi qu'une configuration optimisée de piégeage et de détection, en 2022.

La structure de ce travail de thèse est la suivante :

- Nous nous sommes d'abord concentrés sur l'étude du contexte théorique et sur la description complète du projet MORA dans le **chaiptre 1**. Progressivement, nous nous sommes concentrés sur le dispositif de détection composé de détecteurs d'ions bêta et de recul pour mesurer le paramètre D et d'un ensemble de détecteurs annulaires en silicium segmenté pour le contrôle et la mesure du degré de polarisation.

- Les dénommés RIDE : Les détecteurs d'ions à recul sont examinés en détail au **chaiptre 2**, y compris leur assemblage, leur caractérisation et les méthodes appliquées pour la reconstruction de l'image du détecteur afin d'obtenir la résolution de position. Nous avons également abordé la méthodologie d'essai et les résultats obtenus concernant l'efficacité absolue de l'installation de détection.

- Le **chaiptre 3** est consacré aux détecteurs annulaires au silicium et à leur caractérisation avec des sources radioactives hors ligne sur notre site d'origine au GANIL avant le transfert définitif du système de détection vers l'installation IGISOL.

- Dans le **chaiptre 4**, nous décrivons les progrès réalisés au cours des premiers mois qui ont suivi l'installation de MORA dans les locaux d'IGISOL pendant la commission d'enquête.
  Commençant par un bref aperçu de la manipulation du faisceau d'ions à IGISOL, le chapitre 4 se concentre sur chaque paramètre contributif et sur les progrès de la détection au cours des deux premiers temps de faisceau alloués au début de l'année 2022. Profitant des premières données enregistrées lors de la dernière campagne, nous avons tenté d'obtenir une estimation préliminaire du degré de polarisation (P). Cette première étude nous permet d'estimer la valeur de précision envisagée pour les mesures futures. Les perspectives d'avenir sont également discutées par rapport aux progrès cités lors de la phase initiale des expériences MORA.

- Enfin, nous avons documenté une conclusion pour ce travail de thèse.

Theoretical context of the MORA Project

1.1 Introduction to Matter-Antimatter Asymmetry

Matter and antimatter are symmetric states that should have been created in equal quantities during the Big Bang. Today, only a small percentage of matter, equivalent to about one per billion, could survive, as denoted by the ratio between the number of photons and protons in the Universe. Broadly speaking, because antimatter is a

symmetric state of matter, it should follow the same physics laws and should therefore have followed the same evolution as matter. However, the Universe we witness does not follow these rules. Here are a few examples to support this statement as to why we see a matter-antimatter asymmetric Universe:

1. When Neil Armstrong stepped on the moon, he did not annihilate after stepping there. Therefore, the moon is made of matter.
2. Solar cosmic rays from the sun are matter, not antimatter
3. We have sent probes to almost all the planets, and their survival explains that the solar system is made of matter
4. Cosmic rays sample material from the entire galaxy. In cosmic rays, protons outnumber antiprotons by a ratio of 10^4 to 1, again one instance of proof
5. If there were antimatter galaxies in the Universe, we should see gamma emissions from annihilation. The absence of gamma emission is a trace of strong evidence that at least the nearby clusters of galaxies are matter dominated. At larger scales, there is little proof.

But today's reality is called the "annihilation catastrophe," which probably eliminates the possibility of a matter-antimatter symmetric Universe [21]. Effectively, causality prevents the separation of large chunks of antimatter from matter fast enough to prevent their mutual annihilation in the early Universe. So we can convey that the Universe is most likely matter-dominated. Ultimately, the question we are left with is the presence of antimatter, making it one of the biggest mysteries in physics.

Many experiments have shown that some radioactive decay processes do not produce equal particles and antiparticles. But eventually, it is not enough to explain the asymmetry dilemma of the Universe. Consequently, physicists devoted to the experiments at LHC, ATLAS, CMS, and LHCb, and others doing experiments with neutrinos, such as T2K in Japan, are looking for other processes to explain this puzzling mystery. Some groups of physicists, like the Alpha collaboration at CERN, are working at much lower energies to see if the properties of antimatter are the mirror of their matter counterparts as a test of the CPT symmetry.

Nearly all the non-exotic, which means non-dark matter in the Universe, consists of baryons in the form of protons and neutrons. Measurements of the cosmic microwave background radiation result in the baryonic energy density [22, 23]

$$\rho_b / \rho_{tot} = 0.0456 \pm 0.0015. \tag{1.1}$$

This value is confirmed with the nucleosynthesis calculations for light element abundances [24]. In principle, several contending hypotheses exist to explain the asymmetry of matter and antimatter that resulted in baryogenesis. Any mechanism of baryogenesis must satisfy three Sakharov conditions. In 1967, Andrei Sakharov proposed [25, 26] a set of three crucial conditions that a baryon-generating interaction

must benefit from, producing matter and antimatter at different rates. These conditions inspired the recent discoveries of cosmic background radiation [27] and CP violation in the neutral kaon system [28].

1.2 Some theoretical background

1.2.1 Baryogenesis Conditions

Here we have listed the conditions Sakharov gave, which are required to generate a baryon asymmetry [29] and their possible representation in the Standard Model (SM) and its extensions.

Baryon number violation

Baryon number (B) violation[30] is necessary to produce an excess of baryons over anti-baryons. No direct experimental evidence for B violation has come to light. However, B is violated in the Standard Model itself via the non-perturbative electroweak sphaleron process [31]. Even though not experimentally verified yet, the sphalerons are theoretically non-controversial. Additional sources of B violation may be present in Beyond Standard Model physics unless they disagree with the experimental limits, e.g., proton decay.

Violation of C and CP

C-symmetry violation is needed so that the interactions which can produce more baryons than anti-baryons are not counterbalanced by interactions that produce more anti-baryons than baryons. A similar argument for interactions producing chiral fermions implies CP-symmetry violation. In the Standard Model, CP violation has appeared via a quark-mixing mechanism as a complex phase in the quark mixing matrix of the weak interaction[32]. In the neutrino mixing matrix, there can be a non-zero CP-violating phase, for which somewhat contradictory data has been obtained from T2K [33] and NOVA [34] experiments.

Because of CPT symmetry, violation of CP symmetry leads to the violation of time inversion symmetry or T-symmetry. Even though the CP violation is predicted to occur in the SM, it is not sufficient enough to account for the observed baryon asymmetry of the Universe given the limits on the baryon number violation, which implies that beyond-Standard Model or New Physics (NP) sources/ models, is required.

Regardless of the theoretical advancement, experimentally, CP violation was not observed during the twentieth century in any system other than the neutral kaons. However, enormous progress has been witnessed experimentally in the study of CP violation first at the so-called B factories with *beauty* hadrons, with their observation of CP violation in neutral B meson decays [35, 36] by BaBar and Belle groups, and then later at the Large Hadron Collider (LHC). Still, no experimental findings have appeared that can lead to a significant failure of the SM in the flavor sector or elsewhere.

Process out of thermal equilibrium

A self-consistent quantum field theory (Lorentz invariant with a Hermitian Hamiltonian) is necessarily invariant under CPT, indicating that a particle and its antiparticle masses are the same and the energies of the microstates associated with the occupation numbers of both particles and antiparticles are identical.
In thermal equilibrium, the system will occupy the same number of particle and antiparticle microstates, implying that an asymmetry can only evolve if there is a deviation from thermal equilibrium. The expansion of the Universe supports this in the baryogenesis process.

1.2.2 The mystery of CP violation

Having discussed the general conditions necessary for the baryogenesis process, this section will focus on the second condition of C and CP violation in particular.
The non-invariance of the laws of nature under the combined action of charge conjugation C and parity P transformations, so-called CP violation, is a well-established experimental fact for several decades and is well known to be a necessary condition for the dynamical generation of the observed baryon asymmetry of the Universe, as explained in the last section of the three baryogenesis conditions given by Sakharov [37]. The Standard Model of particle physics includes CP violation through an irreducible complex phase in the *Cabibbo–Kobayashi–Maskawa* (CKM) quark-mixing matrix [7].

For many years, it has been presumed that the elementary processes involving the electromagnetic, the strong, and the weak forces exhibited symmetry with respect to both charge conjugation and parity, which should mean that these two properties were always conserved in particle interactions. The same was maintained for a third operation, time reversal (T), corresponding to the reversal of motion [16]. Invariance under time implies that reversed motion is also allowed whenever a motion is allowed by the laws of physics. A series of findings from the mid-1950s caused physicists to change their assumptions about the invariance of C, P, and T.
The first in the list of basic physics principles to be violated was parity P. Until the mid-1950s, parity conservation was taken for granted mostly in every field of particle physics, supported by an assumption of the abundance of examples of parity conservation in electromagnetic and strong interactions, even though there was little evidence in the other types of interactions. A noticeable lack of the conservation of parity in the decay of charged K-mesons into two or three π-mesons prompted the American theoretical physicists Chen Ning Yang and Tsung-Dao Lee to examine the experimental foundation of parity conservation itself. Thanks to Chien-Shiung Wu's experiment [38], in 1956, they showed no evidence supporting parity invariance in so-called weak interactions[39].

Experiments performed the subsequent year established that parity was not conserved in particle decays, including nuclear beta decay, that occurs via weak forces. These experiments also revealed that C symmetry was broken during these decay processes. The CP violation was verified in the 1964 Fitch–Cronin experiments with

neutral kaons [40], which resulted in the 1980 Nobel Prize in physics (*direct CP violation, i.e., violation of CP symmetry in a decay process, was discovered later, in 1999 [41]*).

In this regard, nuclear beta decay has contributed considerably to developing the weak interaction theory. Several basic foundations of the standard electroweak model, i.e., the assumption of maximal parity violation, the two-component theory (viz. the helicity) of the neutrino, and the vector-axial vector character of the weak interaction were discovered in nuclear beta decay processes.
The conflict of the weak interaction theory, based on low energy phenomena, with the results obtained at higher energies, has motivated the development of a gauge theory of the weak interaction and formed a significant step toward building the unified standard electroweak model. The formalism for nuclear β-decay was firmly established and tested more than three decades ago and was implanted into the larger framework of the standard electroweak model.

Since then, the main motivation of new experiments, performed at low energies with ever higher statistical accuracy, has been to provide precision tests of the discrete symmetries, search for non-Standard Model interaction components, and to evaluate distinct inquiries concerning the light quarks which are addressed in the best way in nuclear and neutron decays.

1.3 Correlations and Coupling Constants in Nuclear beta decay

The correlation observables depend on specific and different combinations of the coupling constants for the possible weak interaction types [42]. They deliver complementary information on the structure of the weak interaction and allow for conducting a broad range of symmetry tests. Observables and isotopes can be selected to maximize the sensitivity to a specific type of interaction or symmetry, considering the finest dependence on nuclear structure-related aspects. Using pure Fermi or Gamow–Teller transitions yields the correlation coefficients independent of the corresponding nuclear matrix elements that are then, to first order, independent of nuclear structure effects.

In a β decay, the kinematic observables that can be measured directly are:

- the total energy E
- the momentum p_i
- the spin $\vec{\sigma}_i$
- the nuclear polarization of the parent nucleus $\frac{\langle \mathbf{J} \rangle}{J}$

where i refer to the decay products i = (e^-, ν_e, recoil ion r). These kinematic observables condition the type of symmetries (C, P, and/or T) to which the coefficient terms are sensitive.

Moreover, it is possible to show that these coefficients are directly related to the coupling constants of the interaction. The Standard Model relies on several assumptions, such as those stated in the $V-A$ theory, and needs to be tested experimentally to confirm or question them.

$$\mathcal{H}_{eff} = \frac{G_F V_{ud}}{\sqrt{2}} \sum_{i=S,P,V,A,T} \left(\overline{\Psi_p} O_i \Psi_n\right) \left[\overline{\Psi_e} O_i \left(C_i + \gamma_5 C_i'\right) \Psi_\nu\right] + h.c. \tag{1.2}$$

The theoretical formalism (1.2) allows us to derive several coefficient terms related to the kinematics of the studied β decay. The event rate distributions (see eq. (1.3)), obtained from Fermi's golden rule in the phase space under consideration, highlight several coefficients directly dependent on these kinematics observables. By measuring very precisely the correlation parameters, whose values are predicted by the model, it is possible to highlight very slight divergences. It is within the framework of these tests on the symmetries of the weak interaction that a correlation coefficient will be preferred to another according to the experimental technique adopted. Table 1.1 shows the main coefficients and the associated thematic terms, allowing us to see which coefficients are sensitive to P and/or T symmetries. The N and R terms do not appear in eq. (1.3), but in alternative expressions of the decay rate, as a function of $\vec{\sigma_e}$, as can be found in [42]. Later sections briefly discuss some of these parameters and associated attained precision.

$$\begin{aligned} \omega\left(\langle \mathbf{J} \rangle | E_e, \Omega_e, \Omega_\nu\right) dE_e d\Omega_e d\Omega_\nu = \frac{F(\pm Z, E_e)}{(2\pi)^5} p_e E_e (E_0 - E_e)^2 dE_e d\Omega_e d\Omega_\nu \\ \times \frac{1}{2}\xi \left\{ 1 + a\frac{\mathbf{p}_e \cdot \mathbf{p}_\nu}{E_e E_\nu} + b\frac{m}{E_e} + \frac{\langle \mathbf{J} \rangle}{J}\left[A\frac{\mathbf{p}_e}{E_e} + B\frac{\mathbf{p}_\nu}{E_\nu} + D\frac{\mathbf{p}_e \times \mathbf{p}_\nu}{E_e E_\nu} \right] \right\} \end{aligned} \tag{1.3}$$

Coefficient Terms	Appeared Correlations	P	T
b *(Fierz Interferance Term)*	m_e/E_e	even	even
$a_{\beta\nu}$ *(Beta-neutrino asymmetry)*	$(p_e p_\nu)/(E_e E_\nu)$	even	even
N	$\sigma_e(\vec{J})$	even	even
A *(Beta asymmetry)*	$(p_e J)/E_e$	odd	even
B *(Neutrino asymmetry)*	$(p_\nu J)/E_\nu$	odd	even
D	$\vec{J}(p_e p_\nu)/(E_e E_\nu)$	even	odd
R	$\sigma_e(\vec{J} p_e)/(E_e)$	even	odd

Table 1.1 – Properties of the coefficients under parity transformation and time reversal. The kinematic terms guiding the coefficients are specified.

In the following, a few examples of recent and ongoing or intended experiments concerning these correlation observables studies will be given, showing the complementary approaches that can be opted for in the experimental framework associated

with Table 1.1.

1.3.1 β-neutrino angular correlation

The β–ν correlation, carried by the parameter a as shown in eq. (1.3), does not need the nucleus or neutron polarization. Its measurement is also quite complicated because the neutrino momentum must be determined. This can be done directly by observing the recoiling daughter nucleus [43,44] or its decay products [45–49].

The β-ν correlation has been essential in resolving the nature of the weak interaction. Also, determining the mixing ratio in mixed Gamow Teller and Fermi transitions and searching for NP remains a requirement [2]. Its measurement permits exploring possible scalar or tensor current contributions via the quadratic reliance of a on the coupling constants. This gives information that is independent of the handedness of such currents. Several new results for the β-ν correlation have become available in the past decade, while new projects have also been initiated. Many use atom or ion traps that deliver excellent source conditions for weak interaction experiments[50]. They present well-localized and cooled samples of particles in a vacuum that can often even be purified in situ. They also allow almost continuous observation of the recoil ions and significantly reduce the effects of scattering for β particles, which is usually limiting in experiments with radioactive sources implanted in a material.

For scalar currents, i.e., Fermi transitions, the experiment with ^{38m}K at TRIUMF [51] used a double MOT trap, and produced the most precise result. Currently, it is being upgraded, reaching a sensitivity at the few per mille level [52] The data obtained for ^{6}He, ^{35}Ar [53] and ^{19}Ne [54] with the Paul trap called "LPCTrap" at GANIL is still under analysis. To reduce systematic effects, the setup was upgraded in the 2010s. It allows separating the different charge states produced by shake-off in the β-decay process. The charge-state distribution allows high-precision β-ν correlation measurements with a statistical precision below 0.5%. As another remarkable example, the WISArD experiment presently focuses on the decay of ^{32}Ar [55,56] aims to extend the present limits on scalar and tensor currents with an approach of measuring the proton energy in beta-delayed proton emission, which is sensitive to the β-ν angular correlations as well as to the Fierz interference term. The experimental study uses a method that tries to improve prior studies by considering positron-proton coincidences. This allows for determining the kinematic shift in the energy of the emitted protons. This coincidence technique can measure correlation terms at the per-mil level. In order to improve the overall performance of the setup, many upgrades are continuing.

1.3.2 Fierz-Interference Term

The Fierz interference term b is yet another one of the observables that could be used to probe the physics beyond the Standard Model. So if we go back to the eq. (1.3), we see that the Fierz interference term is the only effect in the shape of the β-energy spectrum, which has a linear dependence on exotic coupling constants. As such, it is bringing the most direct constraints on exotic S, and T couplings, which would be a

sign of beyond Standard Model physics. Although the effect of this term in the total integral, i.e., the *ft*-values, is maximal for very low endpoints, the effect on the shape is feeble in that limit simply because the factor (the correlation term) becomes almost energy independent, namely $m/E \simeq 1$. It was observed in [57] that the sensitivity for New Physics for shape measurements is maximal for endpoints energies ranging around 1–2 MeV. Also, it decreases very abruptly for smaller or larger values. In this regard, a high precision beta spectrum shape study measuring the half-life of ^{6}He at the low energy facility (LIRAT) of GANIL is ongoing [58].

1.3.3 Trapped and Polarized nuclei

When nuclei are polarized, decay correlations other than the β-ν correlation become accessible as well, such as the β-asymmetry parameter, A, and the neutrino-asymmetry parameter, B, or even the D-triple correlation [42]. Regarding precision weak interaction studies, atom traps deliver almost ideal source conditions as they allow for producing isotopically pure and well-localized samples of atoms/ions at room temperature and the few mK range in a vacuum. Such conditions reduce the effects of scattering of β particles, which can be a limitation when radioactive sources are embedded in a material. In older times, polarimeters were mostly used, like NICOLE at CERN [59, 60], or POLAREX, whereas today MOTs [61, 62] have been the most used tool, widely used for atomic and nuclear physics experiments [63–65] where the isotopes can be polarized by optical pumping. Photoionizing atoms from the excited states in the optical pumping process determines the degree of nuclear polarization. Hence this technique found a sensitive application for correlation measurements in nuclear β-decay. This has significantly extended the number of observables accessible with traps, allowing us to perform a new class of parity and time reversal violation tests, taking advantage of the excellent sample conditions [59] and also allowing the detection of the recoil ion. All four traps, namely the magneto-optical atom trap (MOT), Paul and Penning ion traps, and the electrostatic ion beam trap, are now being used for precision weak interaction studies. Other experiments with isotopes polarized by collinear laser optical pumping, not involving traps, have also been performed.

1.3.4 β-asymmetry

The β-asymmetry parameter, A, needs the initial state to be polarized. This asymmetry parameter can be used to perform precise tests of parity violation, therefore searching, for instance, for right-handed V + A currents. Alternatively, assuming maximal parity violation, it can provide information on possible scalar or tensor currents. Mixed transitions provide a means to determine the Gamow–Teller/Fermi mixing ratio, ρ. The kind of physics to be addressed and the sensitivity that can be obtained depends on the specific β transition selected.

In the last decades, several measurements of the β-asymmetry parameter in nuclear decays have been performed, with the nuclei being polarized either by low-temperature nuclear orientation [60] or by the method of optical pumping on atoms

that are trapped using a technique of MOT. The pure Gamow-Teller β transitions of ^{114}In [60], ^{60}Co [66], and ^{67}Cu [67] have recently been used to search for tensor currents.

1.3.5 ν- asymmetry

The neutrino-asymmetry parameter, B, needs the initial state to be polarized and the observation of the β particle and recoil momenta to determine the neutrino kinematics. It is mainly used to search for right-handed currents and, in the case of neutron decay, to extract λ, although it is not very sensitive in this case [68]. The B parameter also contains a Fierz-like term [42, 69], so we can write it as

$$B(E_e) = B_{SM} + b_B me/E_e. \tag{1.4}$$

Measurement of B in the superallowed mirror β decay of ^{37}K was performed at TRINAT [70] where B_{SM} = -0.7692(15) [71]. As for the β-asymmetry parameter measured with the same isotope, the atoms were cooled and confined in the MOT and polarized utilizing optical pumping and photoionization techniques. Some new measurements are being planned at different laboratories, which are expected to yield statistical results in precision approaching 1×10^{-4} [72].

1.3.6 Triple correlation terms

The predictions of CP violation in the SM are 5 to 10 orders of magnitude lower than the experimental accuracy reached so far on this observable [16]. This leaves a non-negligible room for discovering sources of CP violation not described by the SM. In β decays, searching for sources of CP violation is customary via the measurement of several correlation coefficients, which are T reversal odd. Those are via the CPT theorem, sensitive to CP violation. Under the operation of time reversal, spin, and momentum vectors are odd. The measurement of a coefficient, including an odd number of spin and/or momentum products, is required. Only the D and R coefficients are sensitive to this symmetry in this context [42, 73]. These are the so-called "*triple correlation*" coefficients with respect to the kinematical term, with which they are associated.

The R correlation term is related to the correlation $\vec{\sigma}\cdot(\vec{J}x\vec{p}_e)$, requiring the transverse polarization of the β particles to be measured.

The D correlation term [42] is related to the correlation $\vec{J}\cdot(\vec{p}_e\times\vec{p}_\nu)$ in eq. (1.3). It is possible to show that it is sensitive to an imaginary phase between the Vector and Axial couplings

$$D \propto Im\frac{C_A}{C_V} \tag{1.5}$$

assuming that $C'_A = C_A$ and $C'_V = C_V$ (maximal parity violation).

The latter expression shows that the transition studied needs to be mixed to observe a possible non-zero, beyond SM D correlation: C_A only appears in Gamow Teller transitions, while C_V only in Fermi transitions. The present limits on D_n for the

neutron decipher into a limit on the relative phase between the vector and axial couplings $Im(C_V/C_A)$ =$(1.6 \pm 6.3)\times 10^{-4}$ [74]. Experimentally, measuring the correlation coefficient D requires measuring the electron's and the recoil's momentum (indirectly, the neutrino). The necessity to use polarized nuclei further complicates the experiment. Up to now, the study of neutron [18, 19], and ^{19}Ne [20] decays has allowed measuring D, which gives us the best constraints so far, as mentioned in eq. (1.6) & eq. (1.7).

$$D_n = -0.00012 \pm 0.00020 \tag{1.6}$$

$$D_{^{19}Ne} = 0.0001 \pm 0.0006 \tag{1.7}$$

1.4 The MORA Project

1.4.1 Our approach to measure D

The *MORA* project [75], standing for Matter's Origin from the RadioActivity, gets funding from Region Normandie and ANR, the French national research agency. In collaboration with GANIL, LPC Caen, JYFL in Finland, and other laboratories worldwide, *MORA* attempts to find new sources of *CP* violation to explain the large matter-antimatter asymmetry observed in our Universe. The considered approach is the measurement of the D parameter, measuring the angle between positrons and ions emitted during the decay of short-lived and polarized radioactive elements. Therefore, the measurement of D requires a polarized radioactive source, well located in space under vacuum conditions to allow the detection of recoil ions in coincidence with beta particles.

A Paul-type ion trap, such as the one developed for LPCTrap, is well suited to produce such a source. The polarization of the radioactive nuclei confined in the trap will be achieved by optical pumping of ^{23}Mg ions, as done in βNMR experiments like [76–78] using a laser at an appropriate frequency. It is the first time such polarization is expected to be achieved in a 3-dimensional Paul trap, and this technique will also demonstrate the technical originality of this project.

The degree of polarization will be measured for the first time at Jyväskylä in Finland, in the accelerator facility of the university, using the IGISOL instrumentation for radioactive ion beam production [79]. At IGISOL, the available lasers are easily adjusted to the nuclei of interest (^{23}Mg): With its simple polarization scheme, requiring a circularly polarized $\sigma+$ or $\sigma-$ light of wavelength arounf 280 nm, ^{23}Mg fits our requirement for being an appropriate candidate for such measurement for the D parameter. The final measurement of the D correlation parameter, with exceptional precision, will be performed at GANIL at the DESIR facility, to be built soon, where the ^{23}Mg and another appropriate candidate, which is ^{39}Ca, are anticipated to be produced with higher intensity in forthcoming years.

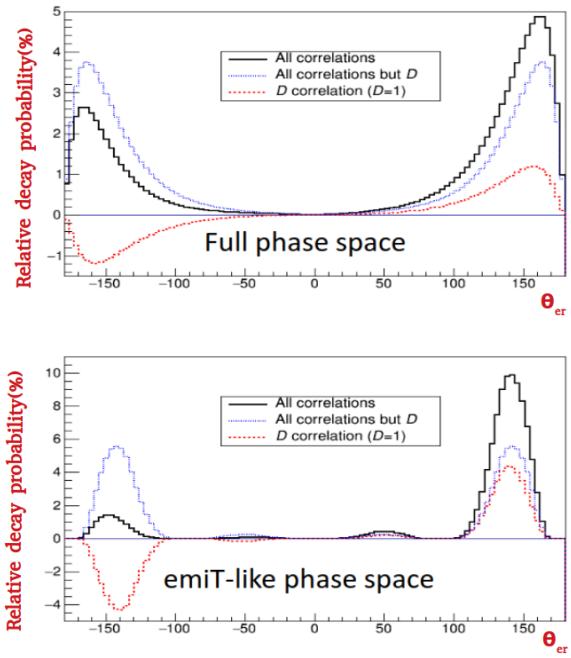

Figure 1.1 – D correlation contribution to the β decay spectrum of $^{23}Mg^{+}$ ion [1]. θ_{er} is the angle between the electron and recoil in the plane perpendicular to the polarization axis. The black line shows here the integral β decay spectrum as a function of θ_{er} , which includes all additional relevant correlations: $a_{\beta\nu}$, A_{β} and B_{ν} from [2]. Blue dotted line: same, without the contribution of the D correlation [1].

1.4.2 Sensitivity to New Physics

In practice, the neutron and nuclear β decays have a very different sensitivity to the relative phase between the vector and axial couplings and can be expressed as in:

$$D(X) = Im(C_V/C_A) \cdot F(X) \tag{1.8}$$

where

$$F(X) = \frac{g_A}{g_V} \cdot \frac{2\rho}{1+\rho^2} \cdot \left(\frac{J}{J+1}\right)^{(1/2)} \tag{1.9}$$

is a factor depending on the nuclear spin and the Gamow-Teller to Fermi ratio and X being the neutron or β decaying nucleus. See [42] for more details. $F(X)$ is also displayed in Table 1.2 for the neutron and different alkali earth element isotopes [80].

New physics can be probed at the level of $D \simeq 10^{-4}$ to constrain the parameter space of the beta decay Hamiltonian, and at the $D \simeq 10^{-5}$ level for specific models, like Leptoquark or Left - Right symmetric ones [17]. The measurement proposed by MORA would also permit the measurement of final state interaction effects (FSI) that have never been observed at the current acquired level of precision on D. These effects are typical of the order of $D_{FSI} \approx 10^{-4}$ to 10^{-5} depending on the system [81, 82]. From recent calculations, an absolute accuracy of 10^{-7} has been verified for the neutron [83].

	n	^{19}Ne	^{23}Mg	^{39}Ca
Sensitivity F(X)	0.43	-0.52	-0.65	0.71
$D_1(\times 10^{-4})$	0.108	2.326	1.904	-0.489
$D_2(\times 10^{-4})$	0.023	0.169	0.099	-0.024

Table 1.2 – Sensitivity F(X) of the D correlation to New Physics for the decay of different X(Neutron/Nuclei) initial states obtained using 1.10

These effects exhibit a dependence on the electron momentum, as shown in eq. (1.10). Their coefficients, estimated in [84], are shown in Table. 1.2 for the neutron, ^{19}Ne and the two candidates for the D correlation measurement with MORA: ^{23}Mg and ^{39}Ca [1].

$$D_{FSI}(P_e) = \left(D_1 \cdot \frac{P_e}{P_e max} + D_2 \cdot \frac{P_e max}{P_e} \right) \tag{1.10}$$

Using Fig. 1.1, we show the contribution of the D correlation to the β decay spectrum of $^{23}Mg^{+}$ ions as a function of the angle between the electron and recoil in the plane perpendicular to the polarization axis.

1.5 The experimental setup

The apparatus of *MORA* consists of a 3-D transparent Paul trap and a dedicated chamber for an orthogonal arrangement of detectors to detect the beta decay of nuclei of interest. The setup is inspired by the one used in the emiT experiment [18] for neutron decay studies. The trap and detection configuration allows us to simultaneously measure the D correlation and monitor the degree of polarization.

1.5.1 Optimized 3-D Paul Trap *(The MORA Trap)*

The *MORA* apparatus's central element in the project's framework is its transparent Paul trap. It is an axially symmetric radio-frequency ion trap designed to confine singly charged radioactive ions to measure the triple correlation parameter D in nuclear β decay of laser-polarised ions. The trap design was inspired by the LPCTrap geometry [12]. LPCTrap was operated at GANIL from 2005 to 2013, with some of the results mentioned in the previous sections and summarized in [53]. The MORATrap, shown in Fig. 1.2, is installed in a vacuum chamber.

In a real (non-ideal) Paul trap, the quadrupole electric potential is imperfect, leading to ion motion instability and affecting the overall trapping efficiency. The RF potential generated in the trapping volume or region of interest (ROI) is not absolutely a quadrupole. Still, it contains some small amplitude, higher-order electric multi-pole components that disturb the ion's motion. Since the ROI's potential depends on the electrode's shape and the applied voltages, optimizing the trap geometry is mandatory to reduce the higher-order harmonics and generate an optimized quadrupole potential.

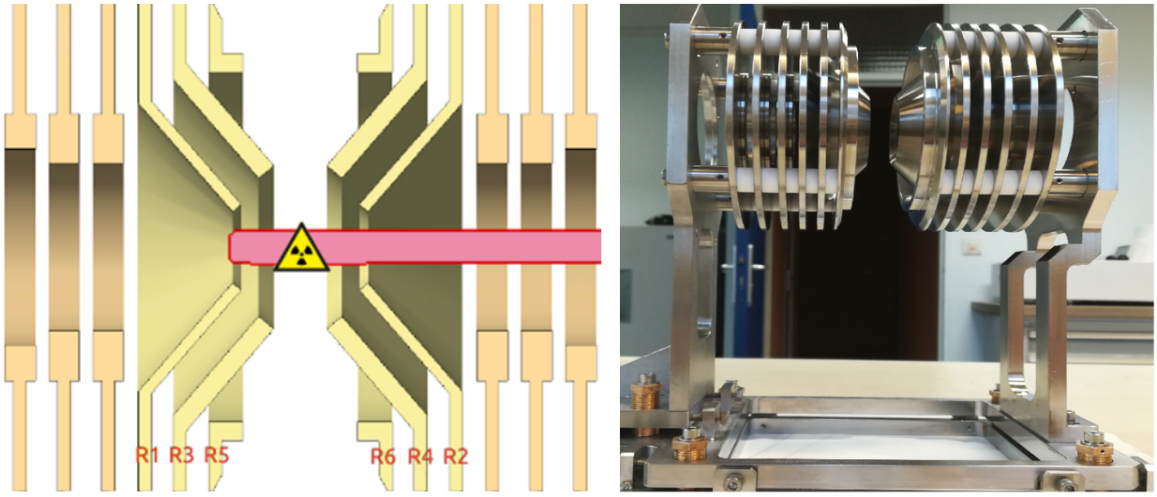

Figure 1.2 – Schematic view of MORATrap showing the trapping electrodes. The trap consists of three-ring electrode pairs (R1 and R2, R3 and R4, R5, and R6) surrounded by two Einzel lens triplets in the center of the *MORA* Detection chamber. The sign of radioactivity shows here the offline radioactive source finger inserted in the trap center, used while detector calibration

With the optimization of geometry, it is possible to reach a quadrupole potential of higher quality, minimize the ion losses from the trap, and increase the trapping lifetime and the space charge capacity. Such improvements are mandatory to reach the statistics required in the *MORA* experiment to search for New Physics. The LPCTrap design [12] has been further optimized by enlarging the quadrupolar region, where higher-order harmonics were controlled to become negligible [85]. Thanks to the conical structure of the trap electrodes, it delivers a slightly larger solid angle for detection. By using the optimized geometry and a more powerful RF, enhanced trapping performances have been expected compared to LPCTrap for instance, increased space charge capacity and a higher trapping lifetime by one order of magnitude.

1.5.2 The *D* correlation measurement

Four pairs of electron and Recoil ion detectors surround the MORATrap. They are arranged alternately in an octagonal geometry assuming 5x5 cm planar surfaces for recoil ion and positron detector at 10 cm from the trap center in the azimuthal plane of the trap, see Fig. 1.3 and 1.4. This detection setup allows close to 20% solid angle coverage for single particle detection. The detection system consists of 4 assemblies of 4 dedicated Phoswich detection systems designed to detect beta particles and four assemblies of MCP based detectors for recoil ion detection. The latter detectors are discussed in detail in the next chapter.

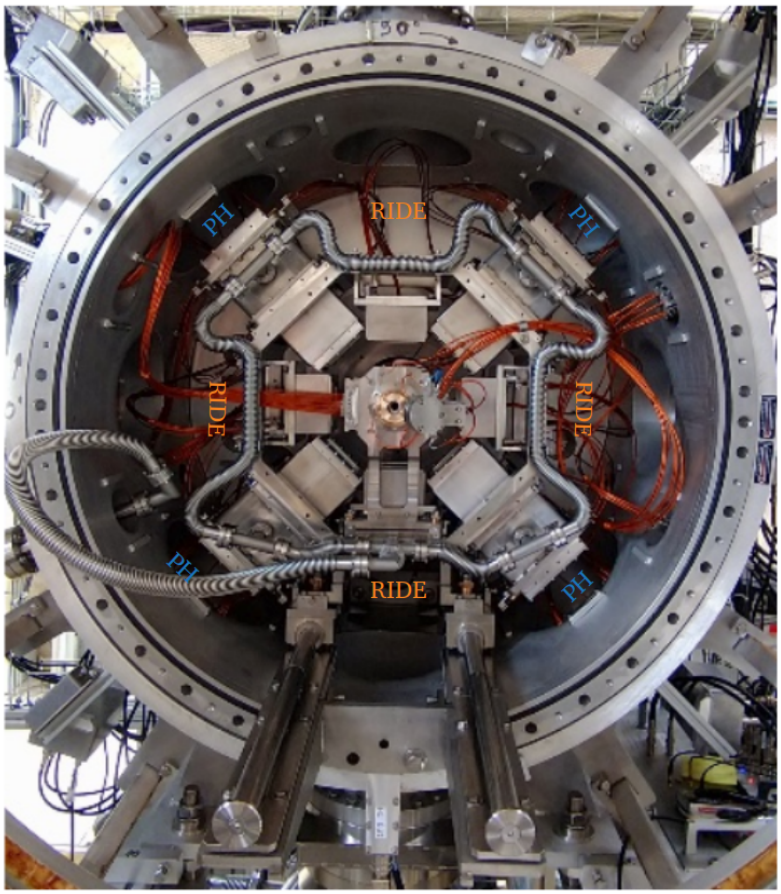

Figure 1.3 – Current installation of *MORA* detection chamber at IGISOL accelerator facility of Jyväskylä in Finland, showing the octagonal arrangement of beta and recoil ion detectors installed on the azimuthal plane of MORATrap.

Given the polarization direction, the D correlation can be inferred from an asymmetry in the number of coincidences recorded at average angles of θ_{er} corresponds +45°, +135° on one side and -45°, -135° on the other side, the sign of θ is defined clockwise with respect to the spin direction (see Fig. 1.4). The D parameter's measurement principle is illustrated using the equation below, where δ is a constant term depending on the detection solid angle and the decay parameters, and P is the polarization degree.

$$D = \frac{1}{\delta.P} \frac{N_{coinc}^{+45} + N_{coinc}^{+135} - N_{coinc}^{-45} - N_{coinc}^{-135}}{N_{coinc}^{+45} + N_{coinc}^{+135} + N_{coinc}^{-45} + N_{coinc}^{-135}} \tag{1.11}$$

The phoswich detection system [86] is designed to witness the beta particles during the decay of trapped and laser-oriented ^{23}Mg ions. The operating principle of such detectors can be interpreted in simple words. Two plastic scintillators, one thin and one thick, are stacked on each other, see Fig. 1.5. Each has different characteristics and is connected to a standard photomultiplier tube which helps to amplify the weak

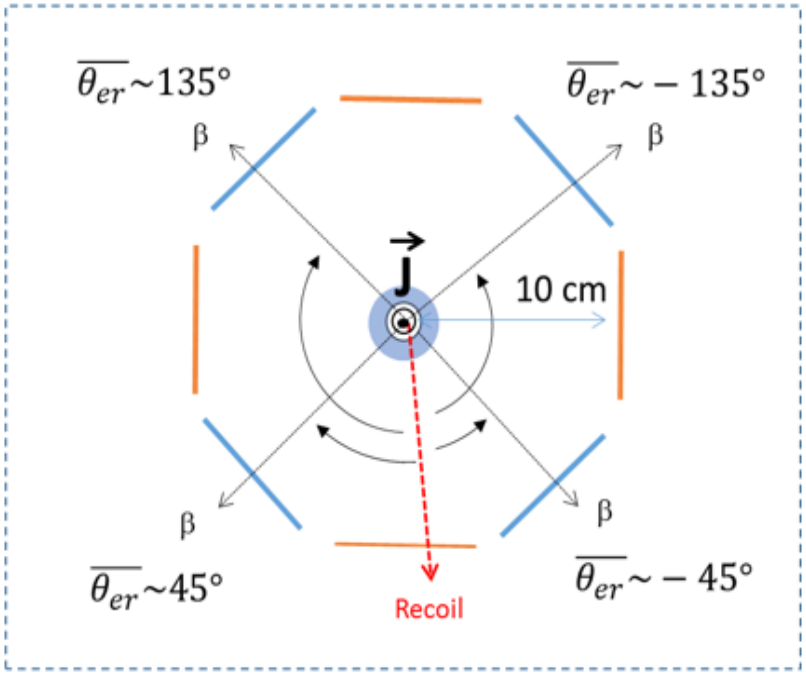

Figure 1.4 – Magnified view of the D correlation detection setup, showing the different types of β-recoil coincidences.

light signal from the phoswich detector by causing a veritable cascade of electrons collected from the last dynode to be sent to the data acquisition system.

We use a thin scintillator with a fast time constant of 1.8 ns and a thick scintillator having a slower time constant of 285 ns. This type of detection configuration is capable of discriminating between γ rays and $e^{-}s$ by a simple principle:

- The gamma rays will have a high probability of interaction in the thick scintillator, especially by the Compton effect; this probability is too limited in the case of a thin one, and hence most of the energy deposition will be accounted for in the thick scintillator part of the Phoswich Detectors.
- The two scintillators will detect the electrons, having a tendency to leave some of their energies in the thin part and further being stopped in the thick part.
- This significant response information gives us the advantage of discriminating electrons and gammas and attaining a good energy selection process.

The Phoswich detectors were tested successfully at LPC, Caen. Monte Carlo simulations using the GEANT4 toolkit have also been developed to study the energy distribution and detector response function. Characterizing such detectors is an amalgamation of the lengthy testing process in the presence of several radioactive isotopes. In Fig. 1.6, we see the illustration of the slow and fast response of the detector and one example of their first calibration with ^{207}Bi source having a mixture of energies

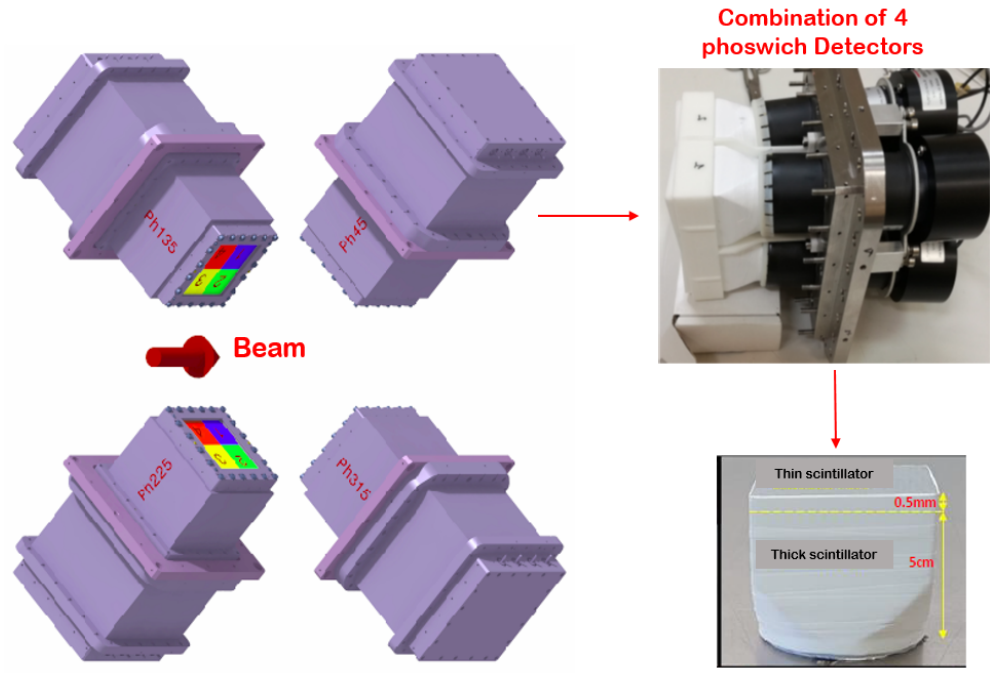

Figure 1.5 – Assembly of 4 phoswich Detectors installed on the azimuthal plane of MORATrap labelled as Ph45, Ph135, Ph225, Ph315 respectively

coming from internal conversion electrons and gammas. We obtained a resolution of 13%, 13.5%, and 11.5% for the conversion electrons peak of 481.7 keV, 994.6 keV, and 1692.2 keV, respectively, in the decay of ^{207}Bi. A comparison of the spectra obtained from GEANT4 simulations and experimental testings with a ^{207}Bi radioactive source is shown in Fig. 1.6. We can see that there is a fair agreement between the two.

1.5.3 P degree measurement

In this experiment, we are presumably able to reach the polarization degree close to 99% because of the extended exposure of the confined ions to the laser light. Thanks to annular silicon detectors installed in and along the axis of the MORATrap, we measure the degree of polarization by considering the beta asymmetry observed between the two silicon detectors. An independent measurement of the degree of polarization would enable us, for instance, the precise measurement of the A_β and B_ν correlations that could be used further for other Standard Model tests, like determining the V_{ud} parameter from mirror transitions [87]. The proof-of-principle of the laser polarization is in an ongoing phase at JYFL at the IGISOL-4 facility with a pulsed laser system.

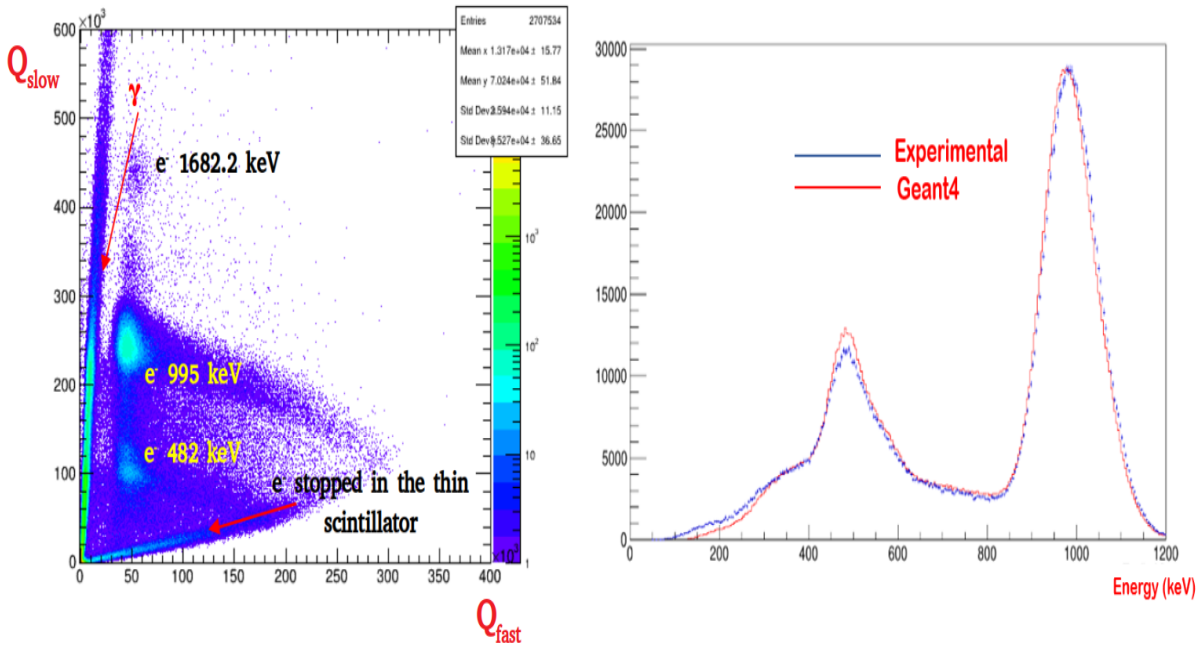

Figure 1.6 – Left: SLOW vs. FAST Phoswich detector response allowing efficient discrimination between detected electrons and gamma; Right: Comparison of the spectra obtained from Geant4 simulations and experimental testings with ^{207}Bi radioactive source.

1.5.4 Laser Polarization of $^{23}Mg^{+}$

Radioactive ion trapping has been proven to be an extremely efficient process, particularly since the dawn of ion cooling techniques in RFQ (Radio Frequency Quadruple) cooler bunchers. The combination of an ion trap and laser polarization is a fairly new concept taking advantage of the high trapping efficiency of the transparent Paul trap and the high degree of polarization from optical pumping.

This method has been implemented for such correlation measurements in nuclear β decay for the first time. However, so far, laser cooling techniques have already been used in an RFQ cooler buncher for collinear laser spectroscopy [88], and also in the case of Paul traps, where ion laser cooling permits the study of quantum phase transitions in crystals for the few trapped ions in the study of new generation atomic clocks [89]

In the *MORA* framework, we first focussed on $^{23}Mg^{+}$, a suitable candidate for laser pumping and β decay correlation measurements. At the IGISOL-4 facility, the employed laser system will consist of a single broadband pulsed (Ti: Sa) laser, whose frequency will be tripled to cover the transitions leading to the maximum magnetic substates $M_F = \pm 2$ as shown in the Fig. 1.7.

The circularly polarized laser beam will be guided through suitable transport optics to the trap. Based on already performed simulations that also considered the Doppler effect, it was assumed that the achieved polarization would be close to 99 %,

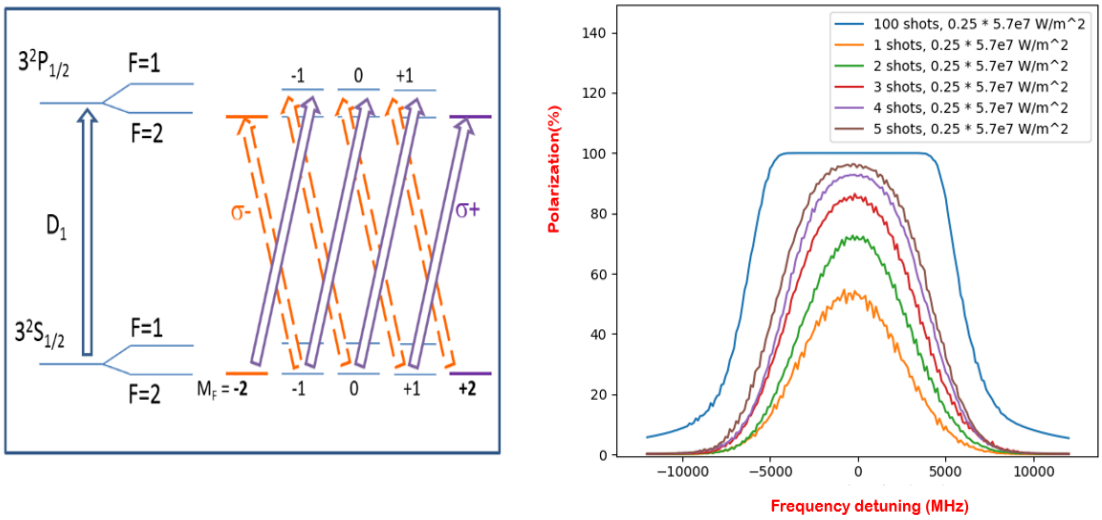

Figure 1.7 – (Left) Illustration of the hyperfine transition used to orient the spin of $^{23}Mg^{+}$ ions (∼280 nm), where F=I+J is the sum of the nuclear spin I and the electron spin J. (Right) The polarization efficiencies for a varying number of 5 μJ pulses spread over an ion cloud of the diameter of 3 mm [1].

with a repetition rate of 10 kHz for every pulse with 0.2 W power.

Ions are cooled down in the trap via collisions with a helium buffer gas at a typical pressure of 10^{-5} mbar, for which we will have no depolarization as the ground state of He is a bosonic state (S=I=J=0). Good care will therefore be taken to monitor the degree of polarization of the laser light by standard optical methods.

The polarization can be inverted by changing the light circular polarization from σ+ to σ-. Helmholtz coils are placed outside the vacuum chamber: they will maintain a B field of the order of a fraction of an mT directed along the axis of the trap to prevent depolarization. A set of annular segmented silicon detectors will take care of the monitoring of polarization degree. These detectors are comprehensively discussed in chapter 3.

1.5.5 Data Acquisition system (DAQ)

In the framework of the *MORA* project, we are utilizing FASTER [90], a new digital modular acquisition system developed at LPC, Caen, designed to handle medium size experiments varying from one to hundred detectors and able to perform tasks in a very versatile manner.

Technically, FASTER is an n-array tree in which nodes function by synchronizing and aggregating the data stream received from the daughter nodes, making decisions

based on the resulting data stream, and then sending the stream back to the parent node. It works as a triggerless system, meaning all the data will be timestamped, allowing nodes to conduct online correlations between measurements over a user-defined time window. FASTER DAQ uses the following standards:

1. UDP/IP protocol
2. Ethernet gigabit connection
3. MicroTCA crate or standalone box
4. VITA 57 daughter boards (the hardware is divided into two parts, i.e., Motherboards and Daughterboards).

The functions of the motherboards are to provide a master clock, a T0 signal, network connections, VITA-57 slots, and FPGAs. The function of the daughter boards is to provide an interface between the detector and the FPGA. Four daughter boards have been developed, but only two are used in *MORA*. *CARAS* provides users with a dual channel 12-bits up to 500 Msps ADC capability, ideally suited for the time of flight, charge, RF, and energy measurement. *MOSAHR* provides users with a four-channel 14-bits up to 125 Msps ADC capability, ideally suited for high-resolution energy measurement.

Currently, six modules are available in the FASTER project: the spectroscopy module, QDC-TDChr, the scaler module, the RF module, the electrometer module, and the decision module. These can be used depending on the user's requirement and the experiment. A module of FASTER is a specific function composed of basically three components:

- A firmware,
- a software controller,
- and a Graphical User Interface

Considering these requirements, histogram declarations are thus performed using a graphical interface.

FASTER utilizes RHB (ROOT Histogram Builder)[91], based on the *ROOT* framework from CERN [92] to declare and fill the histograms without writing any specific source code. One can independently use *RHB* and *FASTER* while communicating over an Ethernet network.

As already mentioned, for the *MORA* setup, we have employed two modules:

- *The QDC-TDChr module*, designed for radiation charge, high-resolution time measurement for the RIDE detectors.
- and *spectroscopy module*, commonly known as the *ADC* module, designed to measure radiation energy spectra composed of a shaper, peak hold, and discriminator functions for annular silicon detectors.

The following chapters will briefly discuss the explicit FASTER modules and important acquisition parameters used in the concerned detection system of *MORA*.

RIDE: The Recoil-Ion Detector

The purpose of this chapter is to present the physics principles behind the so-called RIDE detection system. In addition, we illustrate the critical points regarding the efficient and handy use of MCPs. We discuss in detail the first adaption for the characterizations of this new detector configuration in the GANIL facility, further continued during the first experiment performed in the IGISOL facility of JYFL in Finland.

2.1 General overview of the detector

The Recoil Ion DEtectors, abbreviated as RIDE, are Micro channel plate [93]based detection systems. In the framework of MORA, we use these dedicated detectors for the recoil ion detection in the beta decay of ^{23}Mg. Due to their effective response and significant amplification to detect charged particles ranging from a few eV to higher energies, MCPs propose a firm ground in our experimental studies concerning the detection of recoil ions of a few 100 eV's range.

For the measurement of the D parameter, 4 RIDE detection systems are installed every 90° concerning the direction of the bunched ion beam as shown in Fig 2.1. The nomenclature to address each detector has been defined using their position (angle) concerning the beam direction. For example, the detector installed at 0, 90, 180, and 270 degrees are addressed as RIDE0, RIDE90, RIDE180, and RIDE270, respectively, in the final setup of MORA.
We have modified this detection system by embedding the bare MCP plates provided by *Photonis* [94] along with other suitable components to efficiently detect recoil ions. This modification includes a 90% transmission grid in front of the MCP plate which helps to post-accelerate the ions from the eV to keV energy range. Behind the MCPs, we have mounted a homemade position sensitive flex (PTFI), developed at LPC Caen, which helps to infer the detected particle position, followed by a reflective anode that serves the purpose of minimizing the loss of secondary avalanche electrons by pushing them back to the electrode which is position sensitive.

2.2 Components of an MCP-based RIDE detector

The explanation of the geometry of the whole ride configuration system is illustrated using Fig. 2.2. Each detector that uses MCPs usually consists of three parts:

- A Converter. The Converter is responsible for converting initial particles into electrons or photons that, in turn, efficiently interact with an MCP Plate. We use a MgO coating deposited on the MCP surface in this case. Such coating operates well through the extreme UV and soft X-ray region and low energy ions.

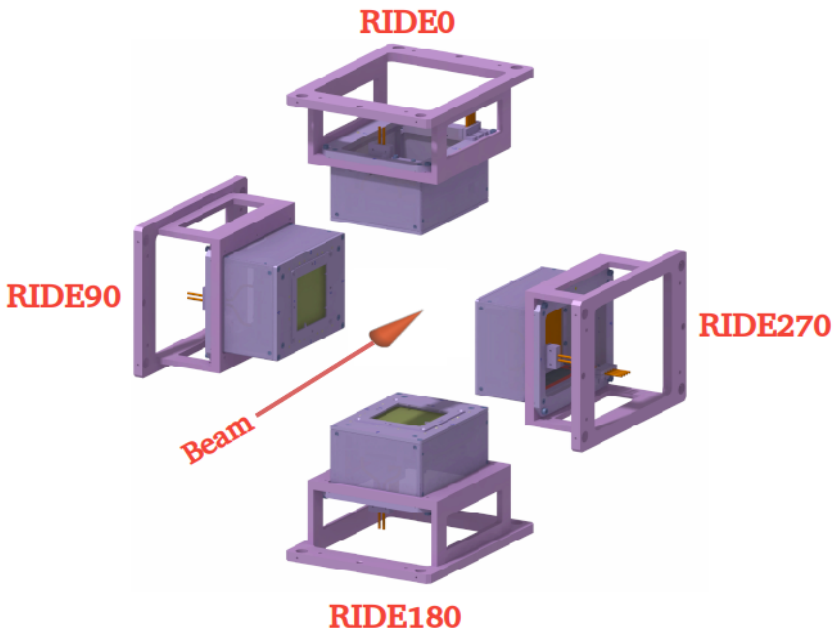

Figure 2.1 – Assembly of 4 RIDE detectors installed on the azimuthal plane of MORATrap

- An assembly of MCPs - providing a mechanism to amplify initial single electron or photon events into an electron pulse. For achieving an exceptionally high again, one often uses a combination of two (so-called Chevron or V-stack) or three (Z-stack) microchannel plates, which are mounted face to face[95], see Fig. 2.4, avoiding any alignment between channels. In our case, we use a chevron stack. In this project, these MCPs were assembled on-site, as shown in Fig. 2.3. The plates are electrically connected in series without metallic coatings at the interface. Compared with simply using a single microchannel plate with correspondingly longer channels, the performance can be substantially better utilizing the combination of two plates because the chevron configuration forbids positive ions to travel backward [95]. The latter are mostly stopped at the interfaces between the plates. Such a configuration eventually helps to achieve a higher gain without excessive noise.

- A Readout Device - providing a mechanism to detect the electron avalanche. In this case, we want to collect comprehensive information about particle behavior, including their detection position. Therefore, we also have integrated a system responsible for this, called PTFI, as position sensitive anode.

The dimensions of the active wafer and other components are represented. More information about the plates and detector specifications, including their operating conditions, are also shown in Table. 2.1.

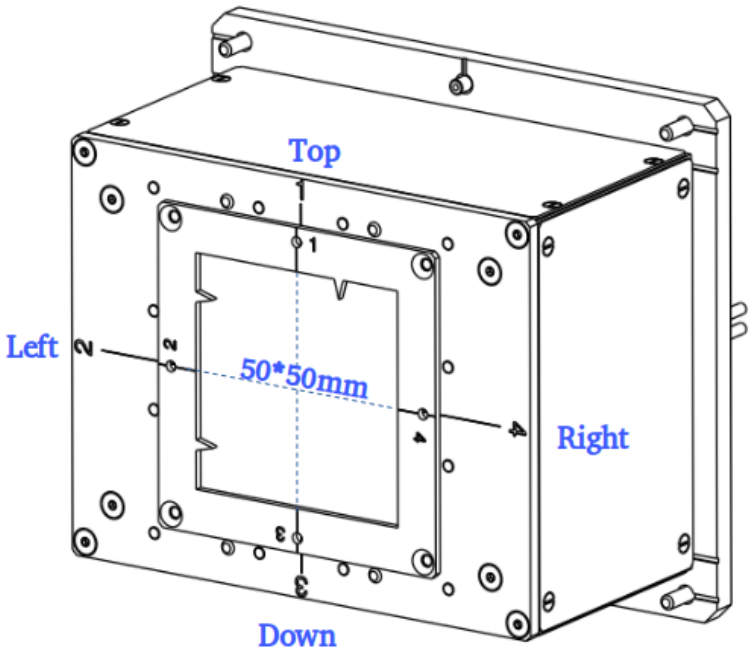

(a) Front view of the detector

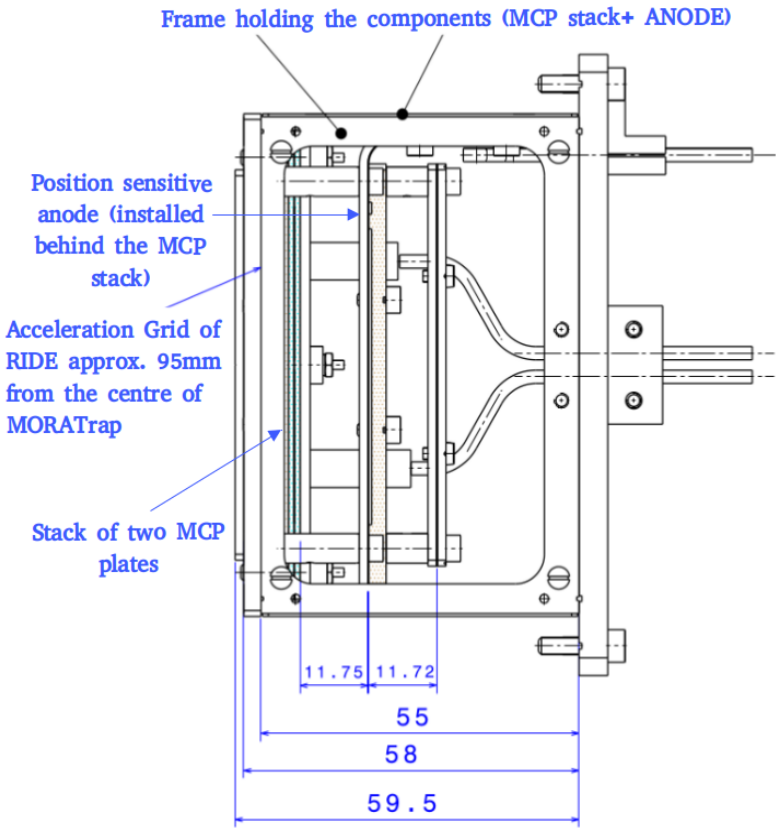

(b) Side-view of the detector

Figure 2.2 – Physical illustration of RIDE detector configuration specifying the dimensions of the geometry including plates and the additional anodes

MCP characteristics	**Specification**
MCP dimension	**(50*50)mm Min.**
Centre-to-centre Spacing	**32μm Nominal**
Pore Size	**25μm Nominal**
Bias Angle	**8$^\circ \pm 1^\circ$**
Open Area Ratio	**50% Minimum**
Detector characteristics	**Specification**
Electron Gain	**4*10^6 @ 2kV**
MCP Resistance	**19-76M-Ω**
Bias Current Range	**26-105μA @2kV**
Dark Counts	**5 counts/sec/cm^2 Max.**
Pulse Height Distribution	**175% Maximum**
Max. Operating Voltage	**2k Volts across MCP's**

Table 2.1 – Micro-channel plates and detector technical specifications

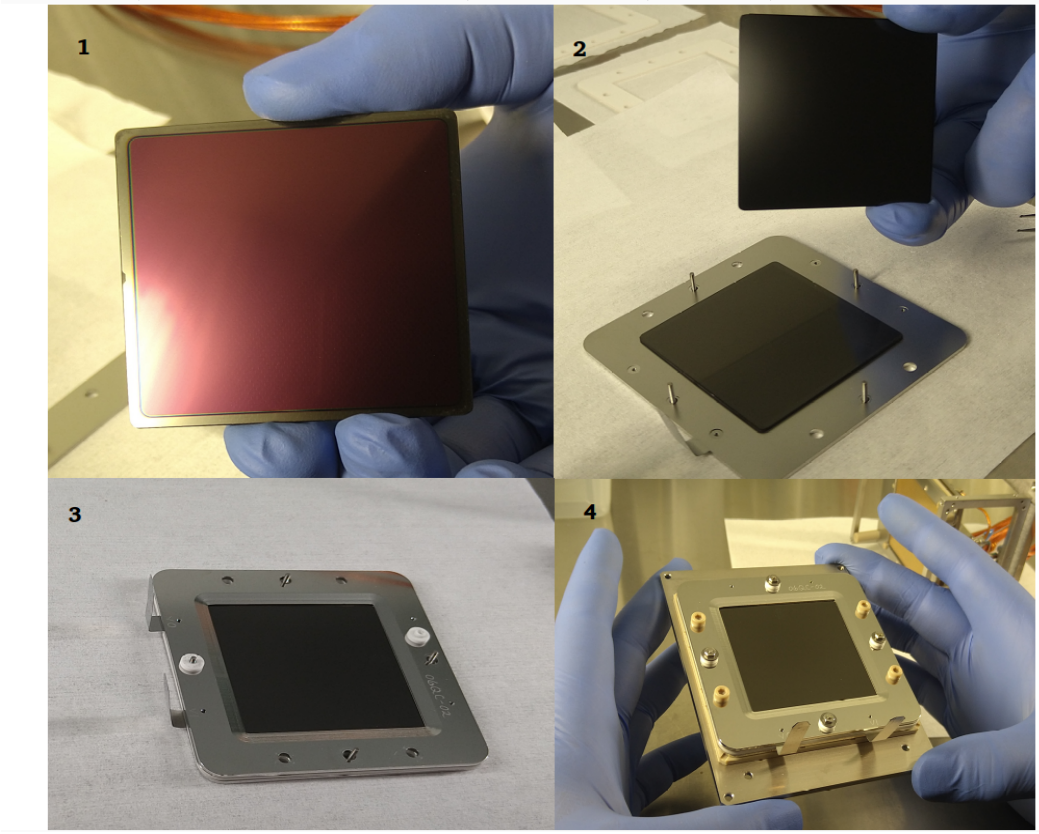

Figure 2.3 – Micro-channel plates (50*50)mm of Chevron Configuration: (1) MgO layered surface (front plate; (2) Installation of the second plate on the back side of the front plate; (3) The assembly includes a base insulator surface and a metallic conducting ring in between the plates; (4) The frame holding the stack together using metallic screws on each side.

Before going into in-depth details, we will go through each component individually, which makes the whole ride detection system.

2.2.1 Key Properties of MCPs

Since their first development in the 1960s, MCP detectors have been used in many applications, such as nuclear physics and space astrophysics. They represent an effective means for detecting particles with energies ranging from UV to X-rays and atoms through MCPs at lower temperatures. Over the past four decades, MCPs have been the subject of several studies that have focused on their lifetime and their detection efficiency against radiation or, depending on parameters such as the applied voltage, the bias angle, the length-to-diameter L/D ratio, the electrode penetration depth, the type of particle or the energy range.

A microchannel plate (MCP) is essentially a fast high gain amplifier for electrons, having many parallel spatial channels, see Fig. 2.4, for use in several applications. This is directly sensitive not only to input electrons but also to other charged particles

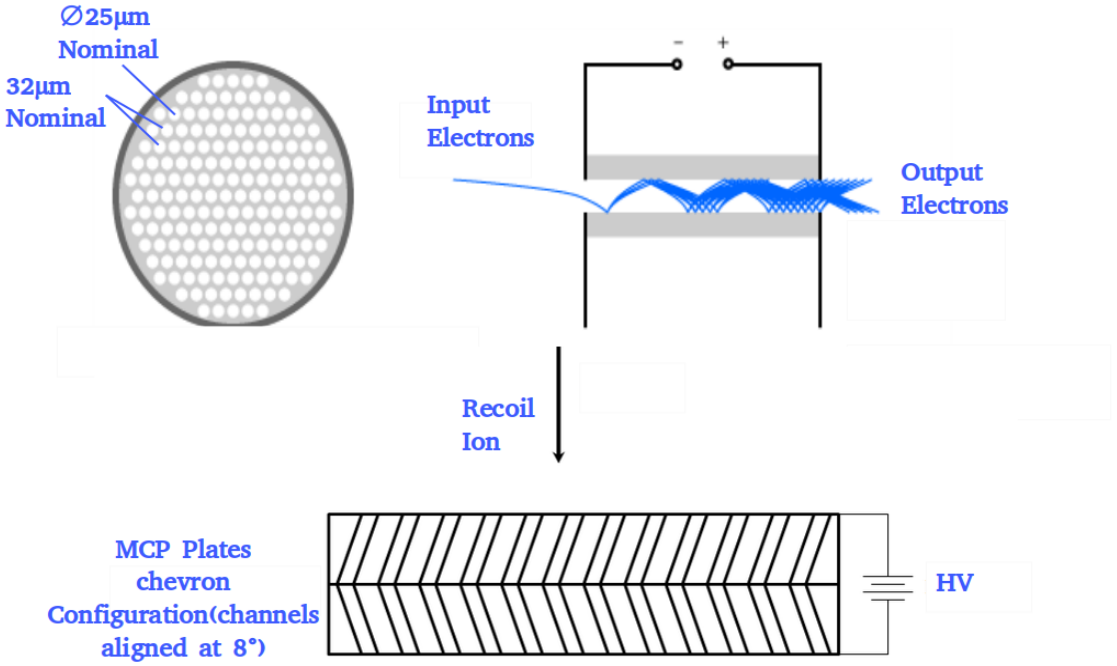

Figure 2.4 – Schematic of a micro-channel plate chevron configuration showing an alignment of channels at a certain angle (8° in this case) as well the electron multiplication dynamics inside their channel walls [3].

(e.g. ions or elementary particles) and to electromagnetic radiation with sufficiently short wavelength (high photon energy), i.e., from the ultraviolet to soft X-rays. The detection efficiency (quantum efficiency) generally depends on the type and energy

of particles.

In a general way, these specially fabricated plates consist of an array of 10^4-10^7 miniature electron multipliers oriented parallel to one another that amplifies electron signals similar to a Secondary Electron Multiplier (SEM). But, unlike SEM, MCP has several million independent channels, and each channel works as an independent electron multiplier, see Fig. 2.4. Typically channel diameters are 10-100 μm and have length-to-diameter ratios between 40 and 100. Channel axes generally are normal or biased at a slight angle to the MCP input surface. The channel matrix is usually fabricated from lead glass and treated in such a way as to optimize the secondary emission characteristics of each channel and to provide the channel walls with semiconducting behavior to allow charge restoration from an external voltage source. The manufacturing process of MCPs goes through a chemical treatment where one generates a thin semiconductor layer on the channel walls. This layer is optimized for high secondary electron emission [93]efficiency and low electrical conductivity. Thus each channel can be considered a continuous dynode structure that acts as its dynode resistor chain.

MCPs can be visulaized as an assembly of millions of miniature Single Electron multipliers. A single incident particle (ion, electron, photon, etc.) enters a channel and emits an electron from the channel wall. Secondary electrons are accelerated by an electric field developed by a voltage applied across both ends of the MCP [96]. The general idea of the trajectory of incident ions and secondary electron emission is illustrated using Fig. 2.4. They travel along their parabolic trajectories until they strike the channel surface, thus producing more secondary electrons. This process is repeated many times along the channel. Consequently, this cascade process eventually yields an electron cloud of several thousand electrons, which appears from the rear side of the plate [93, 96].

Usually, the front and back plates are either circular or rectangular. The diameter of the active area can vary from 20 mm to even more than 100 mm, based on the experimental prerequisites. Since the individual channels confine the electron trajectories, the spatial pattern of electrons at the rear side of the plate preserves the image of particles incident on the front surface. The output signals are typically collected in several ways, including metal, resistive anode (one- or two- dimensional), wedge, or strip anode.

To present a detailed view of this detector configuration, we first go through two critical parameters related to the operation of MCPs.

Gain

Devices with dual-stage MCPs or VMCPs, because of their channel orientation at a certain angle (V-like chevron shape), can achieve a gain of the order of 10^6. In these configurations, the channels of the different plates are generally not aligned, resulting in some loss of spatial resolution. At the interfaces, electrons from one channel can get into more than one channel of the following plate. Sometimes a gap between plates is intentionally left to increase the gain and distribute electrons over a wider

region of space. In the latter case, and depending on the anode used, a barycentric reconstruction can recover a very nice spatial resolution (100μm of the order of the channel size).

Dark Current

One of the important parameters to ponder while operating the MCPs is the dark current. The dark current is the output current – it should not be confused with the strip current (current flowing along the channel wall when a voltage is applied between the two MCP plates) – which occurs without any input signal. Dark current in usual cases is very low, e.g., < 1 pA/cm^2. It should be shallow in a normal operating mode, accounting for a rate of, e.g., a few events per second and cm^2 of an active area. In our case, depending on the dimensions of the MCPs, the dark current is impressively low and accounts for <0.1$\sim$count/s/cm^2. In principle, detectors based on Microchannel Plates come with various designs and serve purposes depending on the type of particles detected, throughput (counts/second), time and position resolution, linearity and sensitivity, signal-to-noise ratio, and other requirements.

2.2.2 Position sensitive Anode

Thanks to the excellent timing properties of MCPs, the latter is often used to measure charged particle's time of flight (TOF) and provide a good timing resolution [97]. If they are operated with proper anodes, they can even be used to measure the position of the incident particles at their surface. In our case, we use a resistive anode printed on a flexible PCB in Kapton. This type of flexible integrated circuit is also being addressed as *PTFI* or *Resistive anode* or *Flex* in the text. This type of anode usually has a very smooth operation. The principles of resistive anodes readout are based on charge division methods. It presents good spatial resolution, as we will see later in the following sections. In this section, the idea of a resistive anode coupled to a micro-channel plate is illustrated.

The resistive anode of the RIDE detectors consists of horizontal strips (pitch 1.3mm) connected to their neighbours by the mean of 10 Ω resistors, see Fig. 2.5. In and between the strips, one can see pads (pitch of 0.9mm) vertically connected on the back side of the Kapton PCB. Each vertical band of pads is connected to their neighbours by the mean of 10 Ω resistors.
In principle, when a particle hits the front side of the MCP, the signal is amplified, depending on the polarization voltage. The total charge is spread on the resistive anode's surface, which illuminates horizontal strips and vertical pads simultaneously, see Fig. 2.6. Unlike delay line anodes, it should be remembered that there is almost no time delay in the charge collection at the anode and the particle being detected on MCP. The charge collected on the MCP (Q_{MCP}) further produces four signals in four directions. The value of these four charges, namely (Q_{left}, Q_{right}, Q_{top}, Q_{bottom}) depends on the total collected charge and on the position of the incident particle hitting the MCP in front, see Fig. 2.7.
The internal connections of the MCPs are also briefly explained in this section to retrieve the signal response from the back of the MCP and the position-sensitive anode,

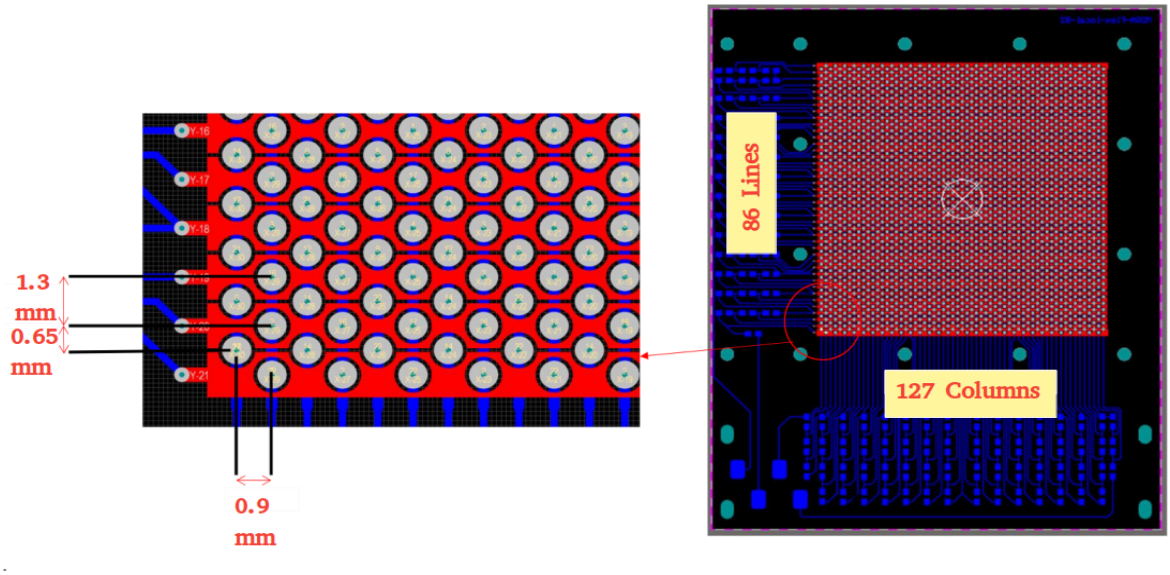

Figure 2.5 – Image of Resistive anode showing vertical pads and horizontal strips and their dimensions.

connected with a reflective anode to mitigate the loss of electrons and force them back towards the anode, which is position sensitive. The connections, which have been utilized to calibrate the resistive anode image in terms of position, are an essential part of integrating the detector configuration into the FASTER data acquisition and processing system. The latter is explained briefly below.

2.2.3 Voltage-divider

To maintain the desired potential on each electrode, the internal connection of the RIDE detector is illustrated using Fig. 2.8. The detector is biased with a negative potential of 4000 Volts which goes through a voltage divider bridge taking care of the subtle potential difference between plates and the two electrodes to maintain the preferential biasing potential between the two plates, not higher than 2000 volts.

Fundamentally, a voltage divider circuit is a simple circuit that turns a large voltage into smaller ones, as shown in Fig. 2.8. Using two resistors in series and with the high input voltage, we created an output voltage that is a fractional input value. For example, in this case, we will say the resistor close to the input voltage is R1, and the resistor most proximate to the ground is R2. We have considered this simple formula 2.1, which helps us acquire the correct voltage division by choosing the valid resistance values.

$$V_{out} = V_{in} \cdot \frac{R_2}{R_1 + R_2} \tag{2.1}$$

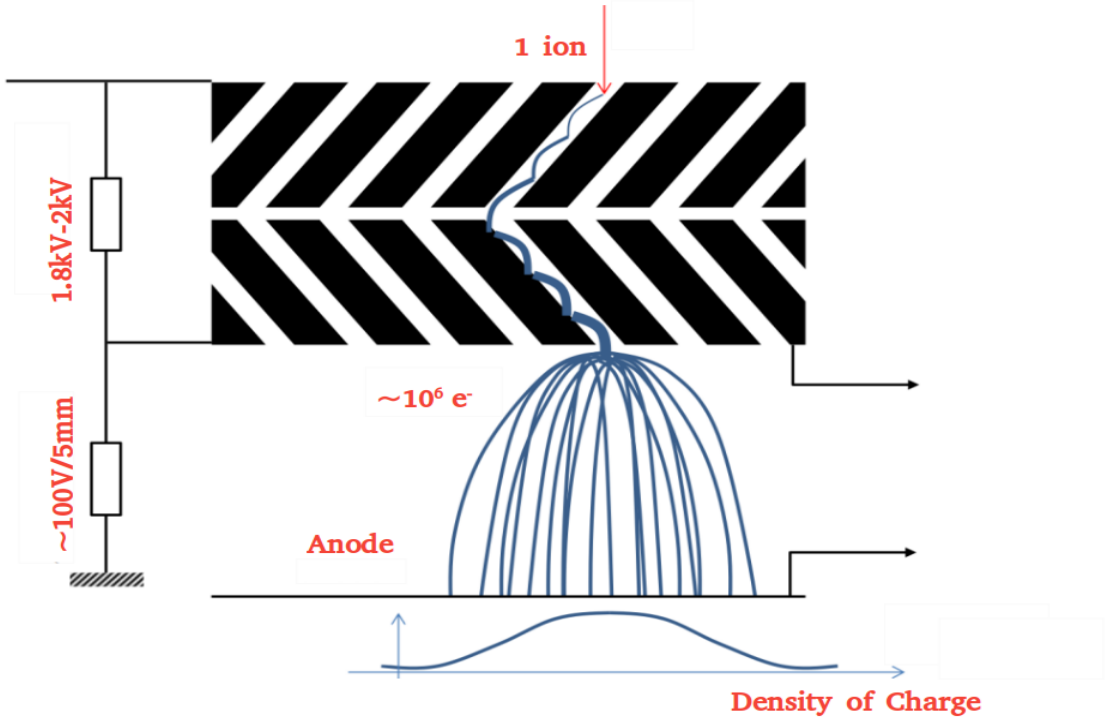

Figure 2.6 – Illustration of electron avalanche principle in Micro-channel plates followed by their spatial distribution on the anode.

The applied voltages on each plate and anode are summarized using Table. 2.2.

2.2.4 Fast amplifiers

The avalanche of electrons leaving the MCPs induces a fast positive signal on the back side of the MCPs and a fast negative signal on the positions-sensitive flex wires in X and Y directions. The reflective anode next to the flex wires is biased with slightly different voltages and is used to reflect the residual electrons back to the flex.

Five signals are read out: one from the MCP back side, four from the ends of the X and Y directions of PSA, see Fig. 2.8 (BNC outputs). The MCP back-side signal is inverted using a homemade inverter and amplified by an Ortec VT120C fast amplifier. This configuration is also explained using a schematic as illustrated in Fig. 2.9. This

Electrode	Voltage(V)
MCP Front	-3900
MCP back	-2100
PSA	-2000
Reflective anode	-2100

Table 2.2 – Applied bias voltages on RIDE detection system.

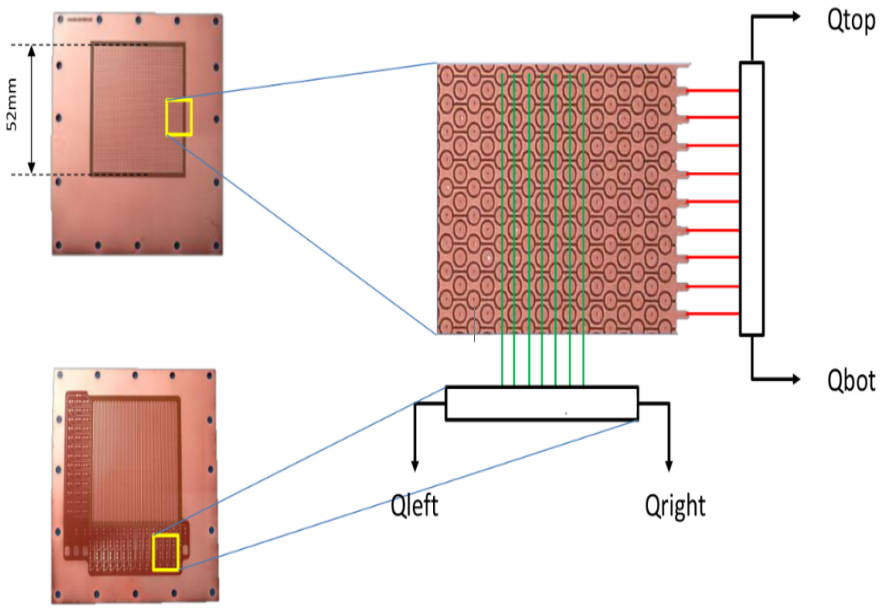

Figure 2.7 – Resistive anode made of Kapton Printed Circuit Board facing the back side of the MCP showing the charge distribution principle in 4 directions.

Ortec VT120C fast amplifier also amplifies the four anode signals. The amplification gain is equivalent to 200 in this case.

2.2.5 FASTER settings

As soon as each detector component is ready with suitable power-delivering devices, the next contributing factor in the characterization process is the Data Acquisition system (DAQ). It plays an essential role. Superficially, we can say it is a process of sampling signals that measure real-world physical conditions and converting the resulting samples into numerical values that a computer can manipulate. Practically, with DAQ, one gathers the detectors' data, called Readout. The DAQ forms and stores these data feeds that we call events and then provides control, configuration, and monitoring facilities for these data events.
The DAQ system used in the MORA framework has also been thoroughly discussed in Chapter 1. Here we will focus on the configuration adapted to characterize the RIDE detectors.

We have utilized the QDC-TDC module of FASTER, which works with the CARAS daughter board. It was the first daughter card developed by the FASTER group in LPC, Caen. A 500 MHz flash charge-to-digital converter (flash QDC) digitizes each of the five MCP amplified signals. Thanks to the excellent functionality of FASTER

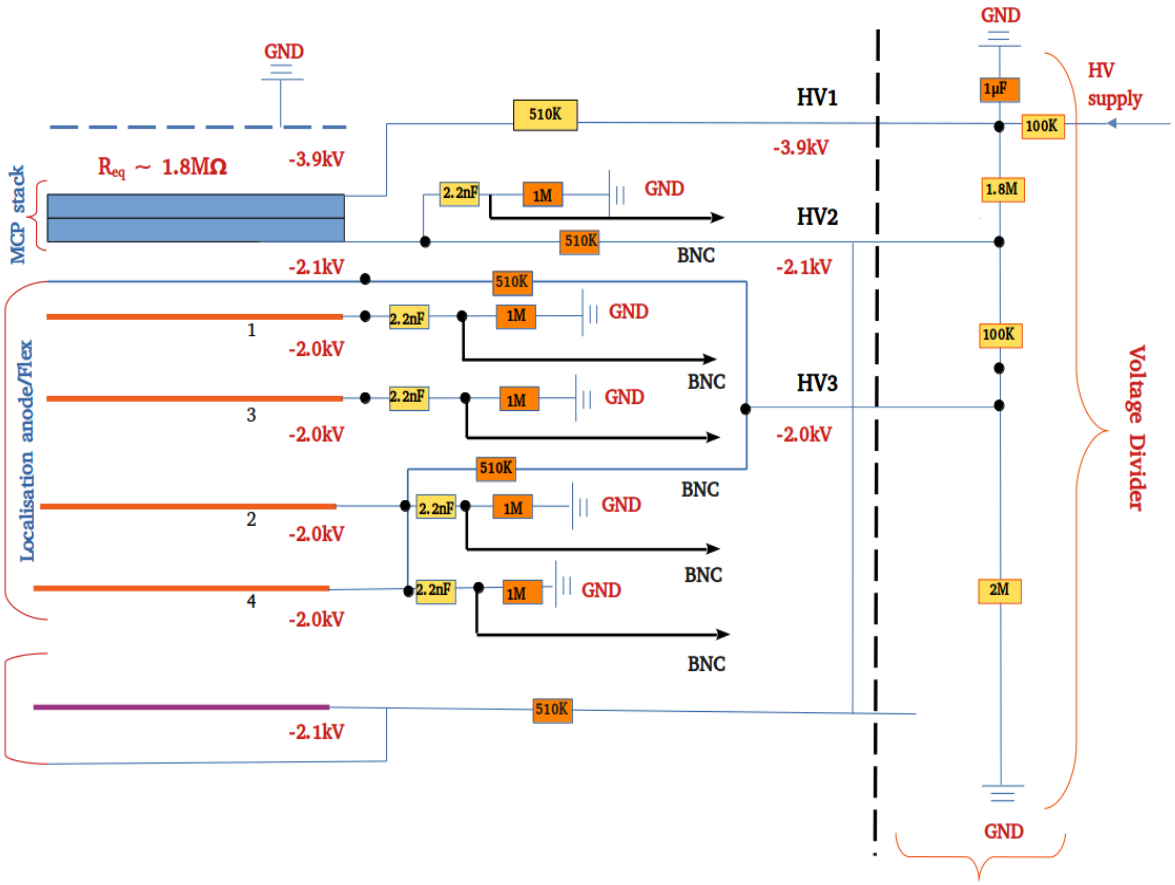

Figure 2.8 – Internal RIDE connections & the voltage divider bridge (right side) installed separately in a box close to the detectors.

DAQ, all QDCs are synchronized, and the pulse filtering, timing, and charge integrating are performed in hardware using modular algorithms. The pulse filtering includes a baseline restoration (BLR) treatment which applies a 160 kHz low-pass filter to the input waveform and subtracts this filtered waveform. The BLR is vetoed when the input waveform is above a certain threshold in mV and during a few ns gates after the input returns to the baseline. The Q_{MCP} signal is positive, with a few hundred mV amplitudes, a rise time of about 2ns, and a fall time of 4 ns. The left, right, top, and bottom localization signals are negative, and their integral depends on the position of the incident particle. One example of the signal produced by these MCP detectors under the bias is shown in Fig. 2.9. We attempted here to highlight some useful parameters using the FASTER pop-up window as illustrated using Fig. 2.10.

1. One of the key features we took advantage of while using it with the RIDE detection system is the switch selection method to change the input impedance. In this case, 50 Ω input impedance possessing an input voltage dynamic range from -1.5 to 1.5V was used.

2. During the initial stage of configuring FASTER, the *Oscilloscope displays* plays

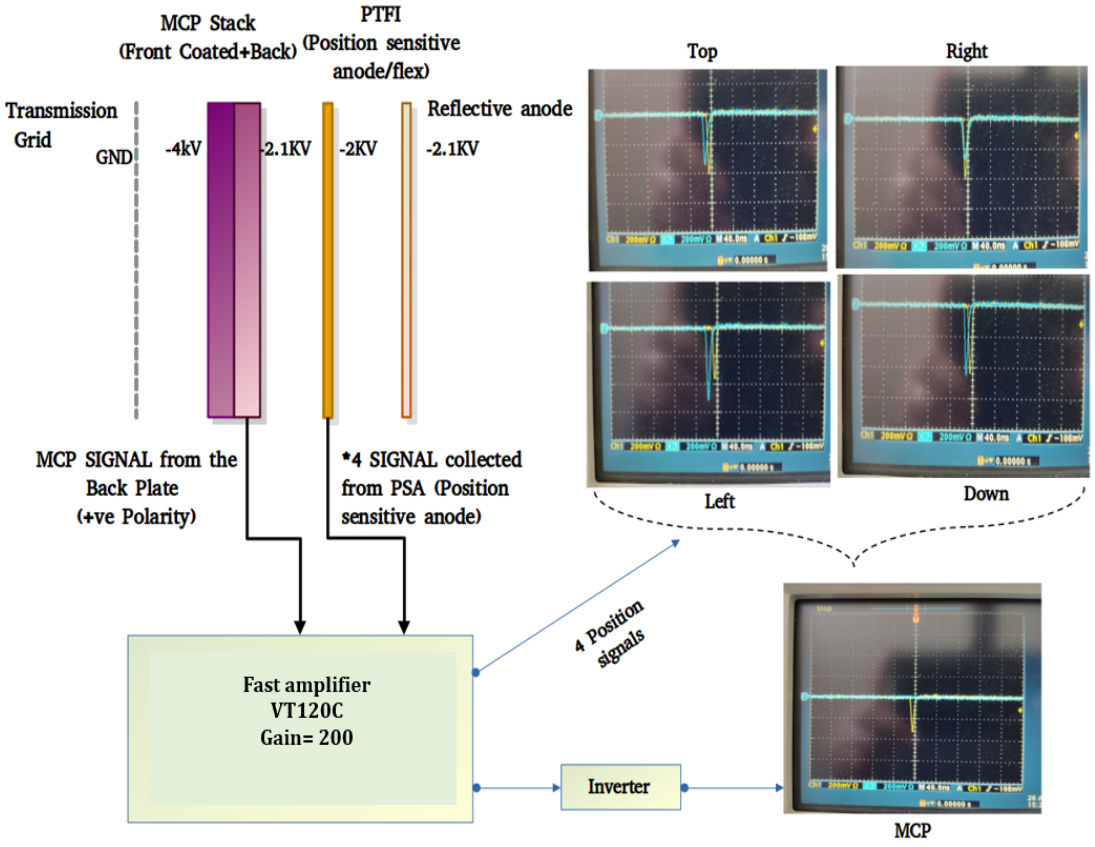

Figure 2.9 – Schematic to illustrate the RIDE detector connections through A fast amplifier and an inverter. The shape of the signals coming from the MCP back plate and PSA is illustrated using the oscilloscope view.

an important role. This tuning helps to identify the shape of the signal and its polarity. Additionally, the user can select 9 full-scale ranges from 6 μs to 1.4 ns on a horizontal scale and up to 2400V on a vertical scale. It is also possible to manipulate the oscilloscope acquisition speed by changing the frequency of counters in this module.

3. The *Low pass filter* module avoids triggering pulse spikes or noise. This module was used occasionally during the testing period under such circumstances.

4. One of the essential tuning parameters in our case is *Baseline Restorer* (BLR). While tuning the BLR threshold, we must inspect the *Input dynamic BLR* with the internal oscilloscope. The threshold should always be chosen just above the noise. If the BLR is wrongly adjusted or set too high, a good event can be considered a baseline and will not be considered.

5. With the help of the Trigger module, one can choose whether to work with internal or external triggers. We used the internal *Constant Fraction Discriminator* option since it is the best option for better precision while doing Time of Flight measurements.

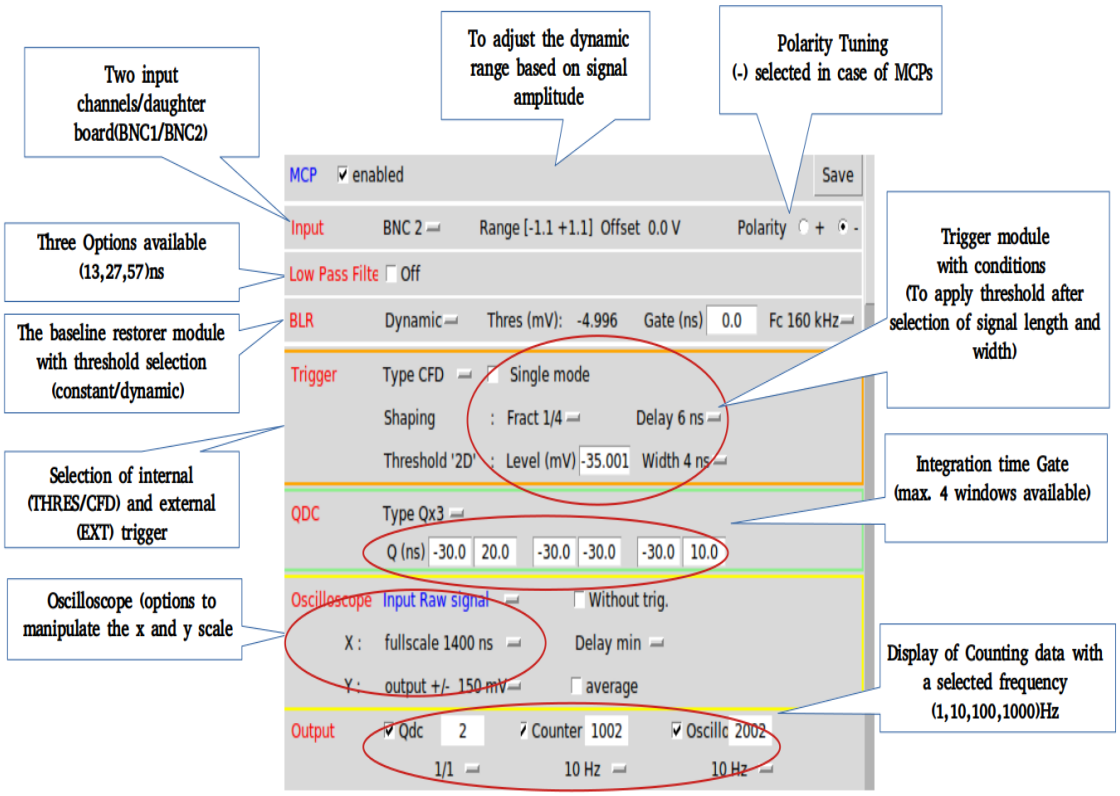

Figure 2.10 – Key parameters while handling the FASTER QDC-TDC-hr module.

2.3 Experimental test setup

On the premises of the GANIL facility, we commenced with this detection system by installing a dedicated testing bench to characterize and study the detectors in their new configuration. The detection system (MCP) is sensitive to pressure variations and suffers from unwanted background for pressures beyond 10^{-5} mbar. Initially, the test bench comprises a vacuum chamber specifically designed to test the detectors. In a cross shape, the chamber (see Fig. 2.11) enabled the usage of a radioactive ion source and facilitated its positioning towards the detection system. Rotary and turbo pumps are positioned in series. The rotary pump helps to acquire the vacuum pressure down to 10^{-3} mbar, and soon after approaching this value, the turbo pump, which operates in a cascade to the rotary one, starts a compression to obtain a secondary vacuum down to 10^{-7} mbar. To control the existing vacuum in the enclosure, vacuum gauges, and their controllers are installed to monitor and measure pressure values. There are two pressure gauges allowing control of the primary vacuum (from 10^{-3} to 10^{-4} mbar) and two other gauges allowing checking the secondary vacuum (from 10^{-4} to 10^{-8} mbar). It takes about 6-8 hours of time to reach the desired value ($<10^{-6}$ mbar). The referred images give a better understanding of the pumping system and the testing environment adapted while handling the RIDE detection system in the

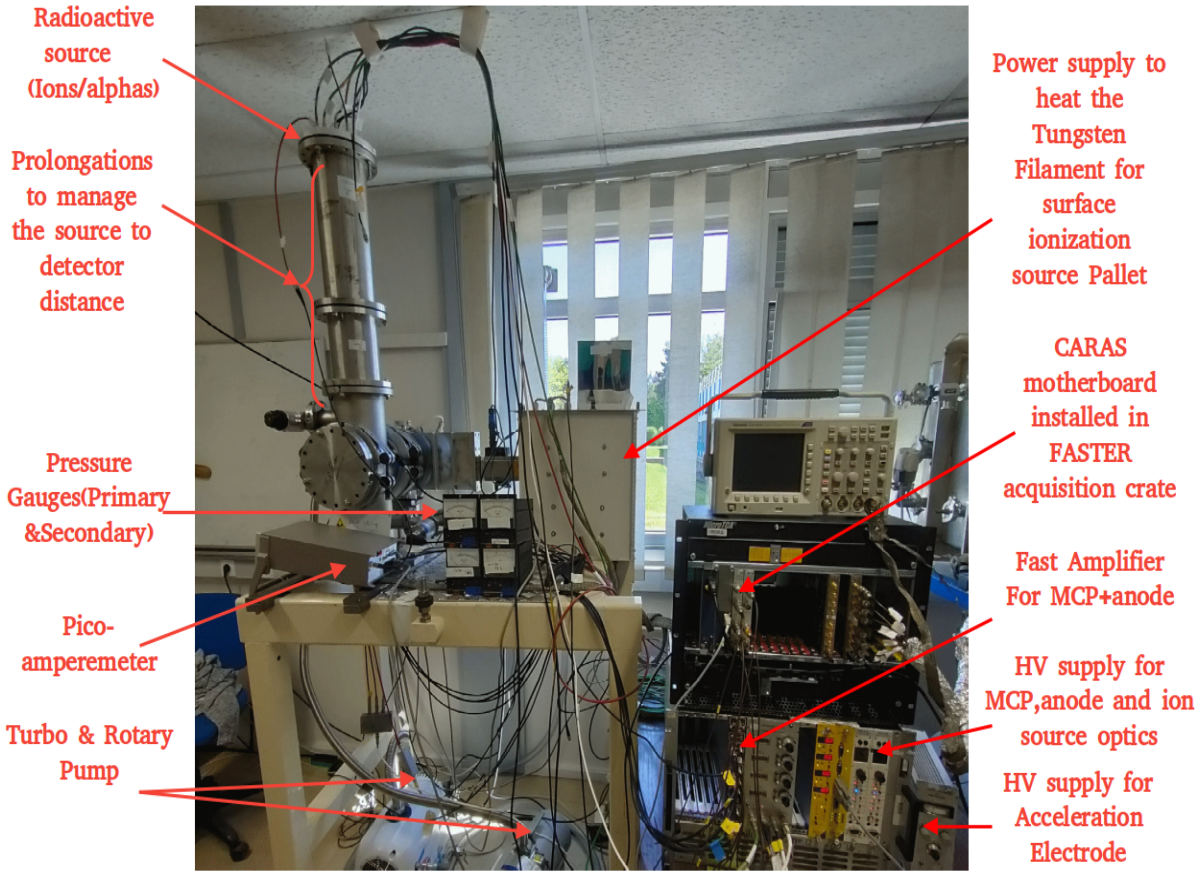

Figure 2.11 – Dedicated test bench consisted of the vacuum system and required electronics for RIDE detector characterization and testings with offline ion source or a radioactive alpha source.

preliminary phase. A few important points and steps while operating such a detection system to be noted are listed below:

- A poor vacuum environment will likely shorten MCP life or change MCP operating characteristics. Hence a pressure of 10^{-6} mbar or better is always preferred.
- Higher pressure can also result in high background noise due to ion feedback. When satisfactory vacuum conditions are achieved, biasing voltages can be applied to the detectors.
- It is always recommended that biasing be done slowly and carefully, especially after every chamber venting. Measuring the current of power supplies used for biasing also helps to monitor MCP behaviour.
- The voltage drop across the meter should be taken into consideration when measuring the applied voltage at the MCP stack, which presents a large impedance (several tens of MΩ). The bias voltage should be applied to the MCP in 100-200 volts steps. In the setup, we used, as already said, the front side of MCPs at a

voltage of -4kV, and thanks to the voltage divider, we can maintain a difference of potential of around 1800-2000V between the two sides of the MCPs. In this case, the impedance in parallel to the MCP stack should be compared to one of the meters to correct for the actual biasing voltage.

- If the biasing current is being monitored, no erratic fluctuations should appear. In case they do appear, any damage or contamination should be suspected, and the voltage should be immediately turned off.
- In these circumstances, the assembly should then be inspected before proceeding. Higher potentials than being advised by the producer may result in irreversible damage.

2.4 Test-1: Preliminary Test for Detection Efficiency

2.4.1 Goal

Before studying the in-depth details of the whole detector configuration, we started by doing a small test with bare MCP plates to ensure the quality of MCP prototypes received from Photonis. We started by using a radioactive alpha source, optionally adding a source of exposure of UV laser light, to look for the detection efficiency and any possible sensitivity of the detectors in the presence of UV lasers.

2.4.2 Test and Analysis

In this process, we only took advantage of the stack of MCP (front+back) plates and started biasing the front plate with a negative potential of 2300 volts. A small voltage divider circuit was used to maintain a potential difference of precisely 1770V, with a measured current value of 0.234 mA between the two plates. It is to be noted that during this testing, the vacuum conditions were not as favourable as they should be. This particular small test is represented using Fig. 2.12.

2.4.3 Conclusion

During this preliminary test, we acquired an efficiency of 40(30)% with alpha particles, with no significant sensitivity to the laser. The considerable uncertainty in the measured value is due to high background noise. Although we managed to get some idea of the detector efficiency, it still depended on the detection threshold choice. Charge spectra with or without alphas were indeed found to be very similar.

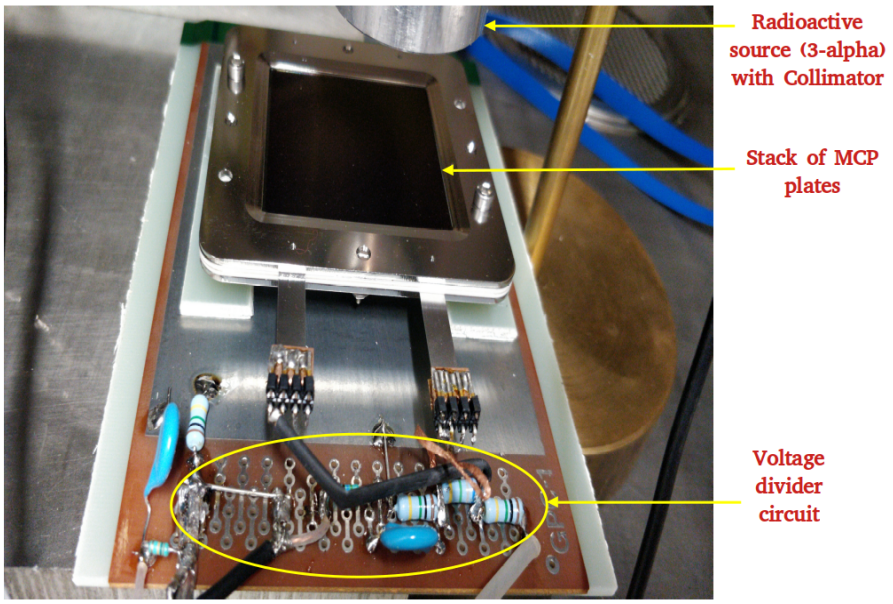

Figure 2.12 – Preliminary detection efficiency tests with bare MCPs configured in chevron using 3-alpha (Am, Pu, Cm), 3kBq radioactive source.

2.5 Test-2: Detector Calibration and Image Reconstruction

2.5.1 Goal

The main goal of this test is to facilitate the purpose of using a position sensitive flex. We first initiated this by constructing the detector's raw image, then its position calibration, and further applying higher order corrections functions for image reconstruction. It is needed to calibrate the MCP position response since it enables a thorough study and reduces systematic uncertainties in a high-precision beta decay experiment like *MORA*. Therefore, it acts as a crucial step.

2.5.2 Calibration mask

In order to reproduce the Detector image, we started with an in situ calibration mask. A stainless steel mask of 1.5 mm thickness and of outer dimensions corresponding here to the dimension of MCPs (50mm$\times$50mm) was used. The mask exhibits a uniform distribution of holes of 1mm in diameter at 5mm pitch distributed throughout its surface, along with a cross shape opening of dimension (10$\times$10)mm of 1mm thickness, which corresponds to the center of the MCP detector (see Fig. 2.13). To obtain an accurate information about the positioning of events on the detector in space (Left, Right, Down, and Up as defined with respect to the ion cloud) the detector will be exposed. We also have L-shaped openings of the same 1mm thickness having the dimension of (5$\times$5)mm engraved on each corner of the calibration mask.

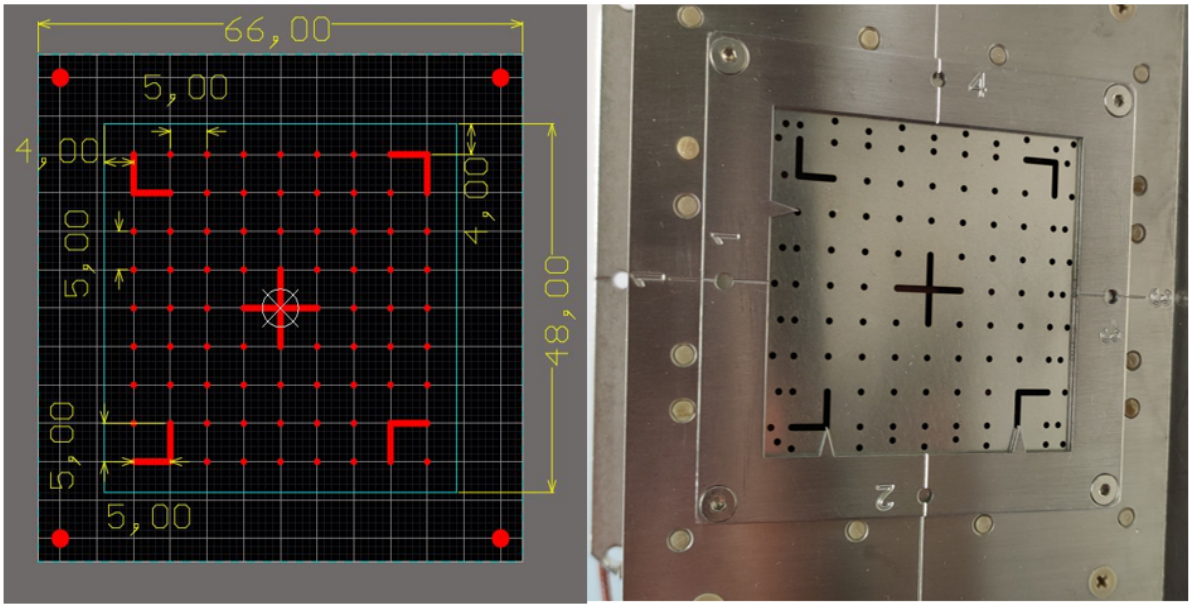

Figure 2.13 – First design of calibration mask to be put in front of the MCP plates and inside the frame as shown in the right.

2.5.3 Image reconstruction

The dynamics of signals on localization channels result from the convolution of the input particle dynamics and localization dynamics. In order to minimize localization uncertainty, we must minimize the noise. Low noise pre-amplifiers and perfect EMC(electromagnetic compatbility) are important in these situations.

In order to analyze the raw image obtained after putting the calibration mask on the top of the MCP surface, the position where the incoming particle hits the MCP detector is determined by taking the value of four charges collected on each end of the position-sensitive anode, namely the charge collected on left, right, top and bottom position. These charges are used to determine the MCP position readout. The x and y estimators can be formulated as follows:

$$\tilde{x} = \frac{Q_{right} - Q_{left}}{Q_{right} + Q_{left}} \tag{2.2}$$

$$\tilde{y} = \frac{Q_{top} - Q_{bottom}}{Q_{top} + Q_{bottom}} \tag{2.3}$$

where Q_{left}, Q_{right}, Q_{top}, and Q_{bottom} correspond to the distributed charges collected on each side of the flex, basically in four directions.
We call in the following Q_{MCP} the total charge collected on the MCP. The $\tilde{x}$ and $\tilde{y}$ estimators usually range from values comprised between -1 and 1 in magnitude and are unitless. They yield an image as illustrated in Fig. 2.14. A part of the range is obviously not covered by the anode ($0.6 < \tilde{x} < -0.6, 0.6 < \tilde{y} < -0.6$): the charge division is done as such that by construction, the smaller charge is never smaller than

one-quarter of the larger. Such boundary condition can be expressed for instance for Q_{left} such as 0.25 $Q_{right} < Q_{left} < 4\ Q_{right}$. The latter condition ensures a minimum charge wherever the event is detected: Q> 0.1 Q_{MCP} for any of the directions right, left, top, or bottom, assuming that Q_{MCP} is distributed evenly in x and y.

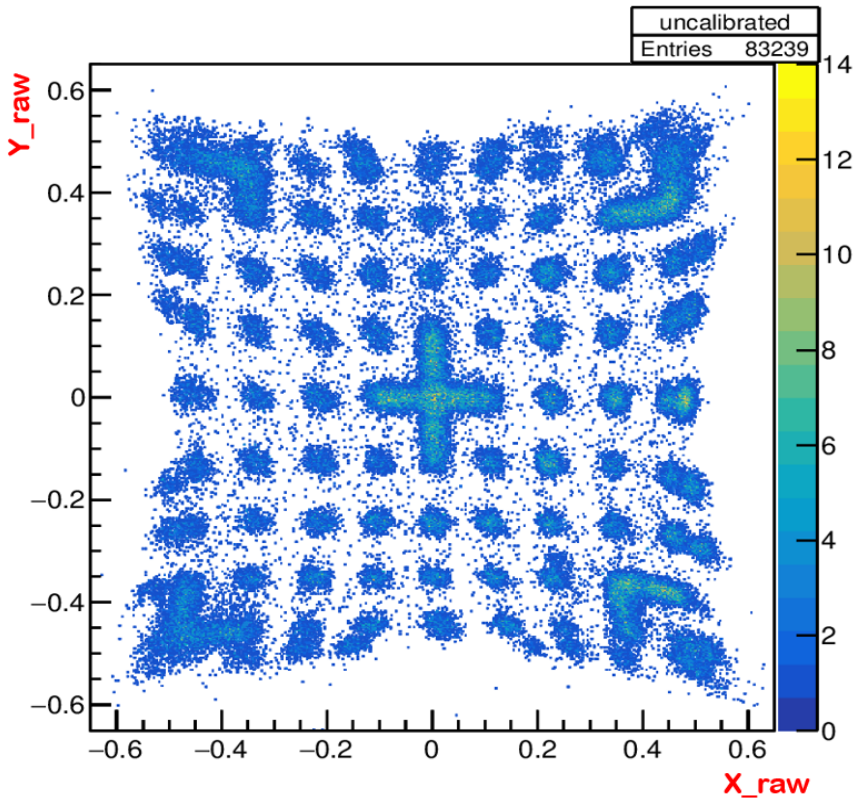

Figure 2.14 – Detector raw image constructed using four localization charges collected from the position-sensitive anode. The x and y-axis are dimensionless position estimators ranging from -1 to 1 in magnitude.

2.5.4 Test Preparation & Troubleshooting

As we already mentioned before, we use a resistive anode with 5 readouts for localization purposes. This kind of device is a priori user-friendly and simple to develop. On the other hand, it suffered some basic defects that complicated its commissioning. We encountered several problems concerning the use of the anode, which was specifically designed for our detection system.

At the beginning of the characterization process, we struggled to achieve an image of the detector corresponding to the specific arrangement of openings in the calibration mask, see Fig. 2.13. Rather than a regular arrangement of holes, as in the mask, we acquired some deformed arrangement caused by an unwanted coupling of localization channels with each other. As it was evident that we are restricted to letting the

charge be distributed over the whole surface of *PTFI*, this eventually made us suspect some defective connections between strips and pads. In the end, this happened to be a problem in the manufacturing of the flex PCB.

Eventually, the problem arising from the anode was discovered. Under technical supervision, we observed that the pads connecting the vertical lines in PTFI were broken at places, leading to the accumulation of charges only at one point. As a result, the PCB also suffered from sparking issues inside the frame holding the detector setup together during the timeline of testing.

One example of the result of the manufacturing issue of PTFI is represented using an image of the detector as illustrated in Fig. 2.16. We can see in this figure how the broken pads (broken pads visible in Fig. 2.15) in the anode can lead to such issues. The case was solved by replacing the PCB using another manufacturing company which led us to continue with the calibration of the detector described after that.

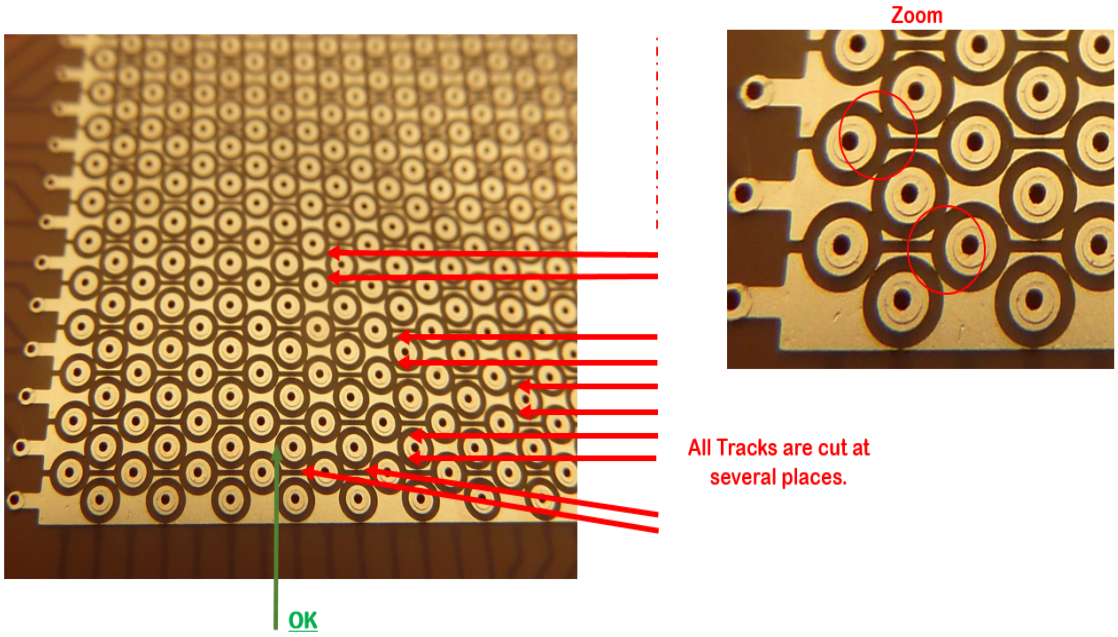

Figure 2.15 – Problem encountered in the position sensitive flex of RIDE detector for MORA: broken vertical pads leading to non-uniform charge distribution on the surface of position-sensitive anode

2.5.5 Image Calibration

The basic idea for calibration here is to determine the correct positions of the central cross and corners L's and several other points distributed along the mask surface from the $\tilde{x}$and $\tilde{y}$ estimators. To achieve this, we have used a correction function that is being constructed to determine the positions of the points as close as possible to

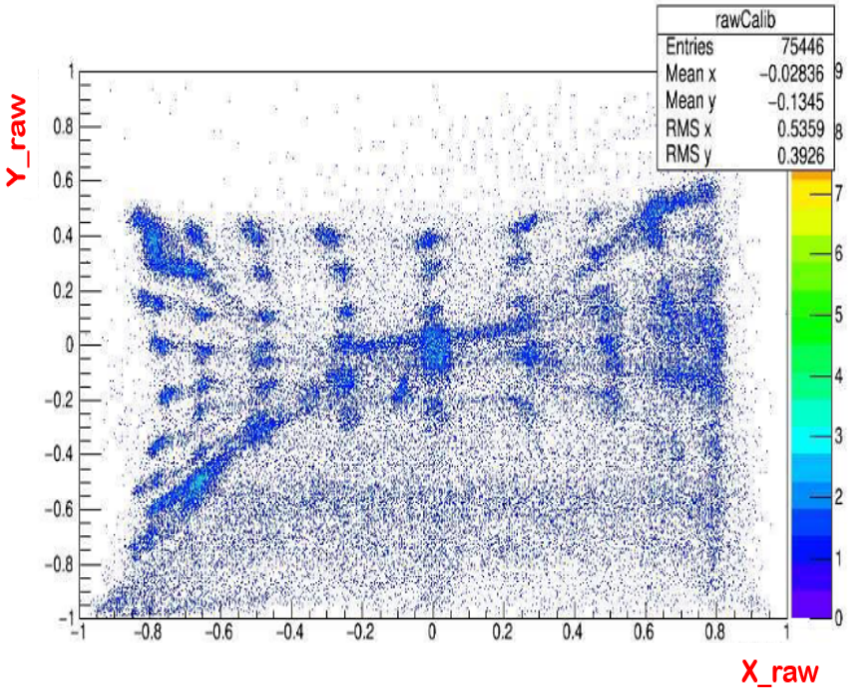

Figure 2.16 – Representation of detector image, very deformed due to broken pads further leading to accumulation and non-uniform distribution of charge on PTFI surface.

their nominal physical positions. These functions are then used to correct the MCP position response.

The Q_{MCP} should be equivalent to the summation of charges collected on the position-sensitive flex. Hence this will be considered the first step of the position measurement calibration, which allows us to equalize the gain of localization channels, see Fig. 2.17. There is no reason this gain should always be the same as there can be gain variation in different operating parameters (gain variation of fast amplifiers, the sensitivity of CARAS channels etc.)
Moving further, progressively, we will discuss the polynomial corrections applied to the obtained raw image of the detector.

2.5.6 Zero-order correction

To proceed further with the image reconstruction, we start this process by aligning the obtained raw image of the detector at the center, which corresponds to the nominal physical value of the mask position on the detector. The raw image obtained has values ranging from -1 to +1 in two dimensions. This process, in principle, does a translational displacement of the image to center the raw image at the origin, corresponding to the center in the physical mask. The data is retrieved in the .fast format binary file from the FASTER data acquisition system, which is further converted into

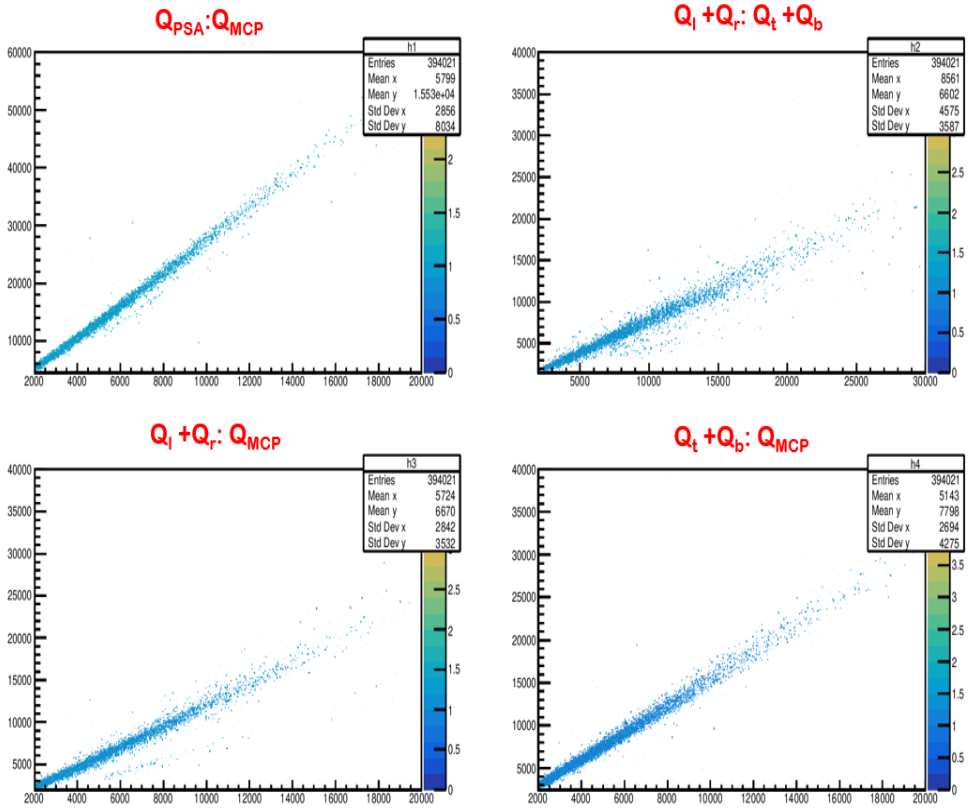

Figure 2.17 – Linear distribution of charge in between the total charge collected on MCP and four localization channels.

a root file to have convenient access to analyzing it.

We use the root analysis program to treat the charge collected on the MCP and the localization channels to construct the raw image. We equalize the charges collected on the four position channels by projecting the raw image on the x and y plane, see Fig. 2.18, to really fit the image center to the origin. By multiplying the x and y estimators with scaling coefficients, the resultant peak corresponds to the widest opening, a big cross in the center of the calibration mask.

The image construction formula was modified using the scaling factors for the basic stretching and shifting, as illustrated using eq. (2.4) and (2.5). These scaling factors are again chosen such that the middle cross region is centered at the origin of the coordinate system. This step is crucial for our next step, which is the first-order correction and, in our case, the calibration in position.

$$\tilde{x} = \frac{a \cdot Q_{right} - b \cdot Q_{left}}{a \cdot Q_{right} + b \cdot Q_{left}} \tag{2.4}$$

$$\tilde{y} = \frac{c \cdot Q_{top} - 1 \cdot Q_{bottom}}{c \cdot Q_{top} + 1 \cdot Q_{bottom}} \tag{2.5}$$

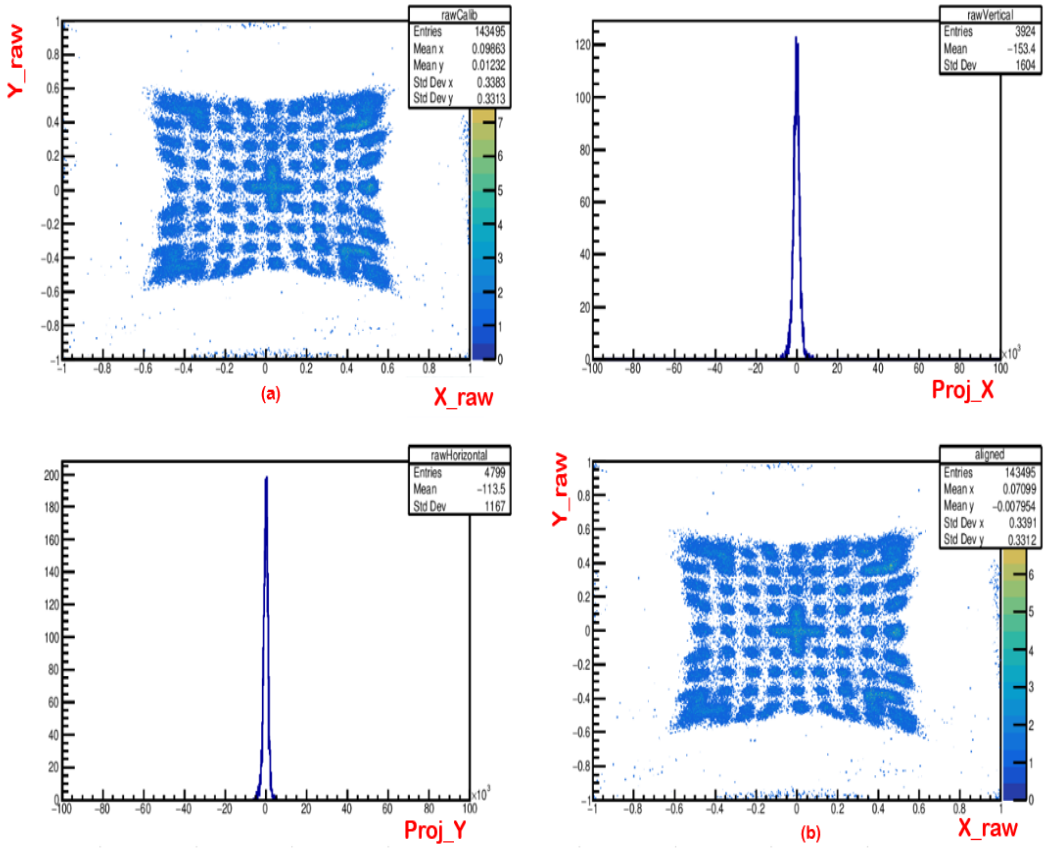

Figure 2.18 – (a) Detector raw-image; (b) Alignment of the raw image by projecting in X and Y plane, where the central position of the cross in the calibration mask corresponds to the center of detector image.

2.5.7 First-order correction/calibration

Succeeding the zeroth order correction, which requires position calibration, which means calibrating the x and y estimator in position, here we have used mm based on the dimension of our detector, which is equivalent to 50 mm.

This process allows us to calibrate the image in position. To do so, we first use a first-order polynomial as illustrated using eq. (2.6) & (2.7) to transform the high accuracy position of the calibration points on the hole side to their physical positions as closely as possible. Using the first-order polynomial function makes the holes in the reconstructed image correspond to the position of visible holes in terms of their exact position on the mask in mm.

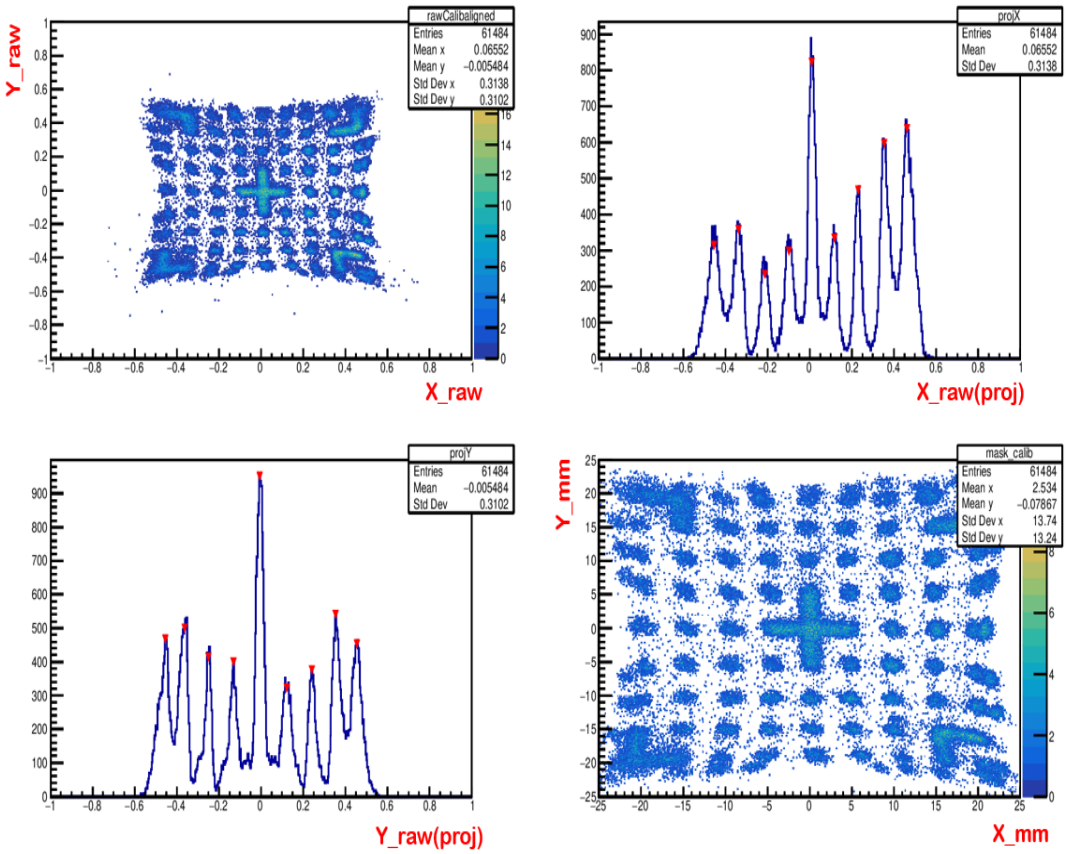

Figure 2.19 – First order correction/calibration of detector raw image, x and y axis projection of central part and calibrated image with axes corresponding to the real physical dimension of the calibration mask/detector.

Using the *peak finding algorithm* in our root analysis, see Fig. 2.19, it is possible to establish the correlation of estimated x and y position for each hole opening to their actual physical position on the calibration mask within an acceptable range. We use a C language script that utilizes the root data file containing all the data point information related to the detector image. In simple words, we only projected the center part of the image on the x and y planes to get the peaks corresponding to each hole distributed alongside the central Cross opening. With the help of this script, we proceed by finding the position of peaks corresponding to the central cross and the small holes via the *TSpectrum* class and inject the latter as initial values of parameters to make a global fit. The same script is used as well to fit the peak areas. One can see the obtained result of this procedure with the help of a linear calibration curve in Fig. 2.20 for horizontal and vertical projection of detector images.

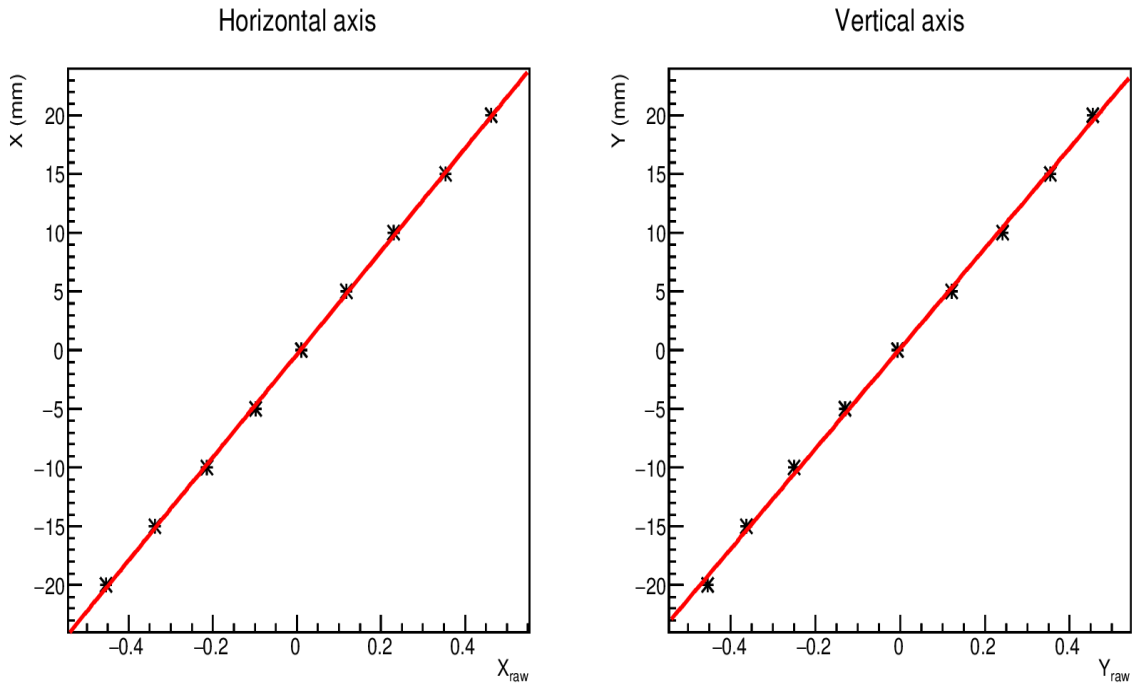

Figure 2.20 – Linear calibration curve obtained for x and y projection of detector image center region using a straight line fit.

$$\tilde{X}(mm) = a \cdot \tilde{x} + b \tag{2.6}$$

$$\tilde{Y}(mm) = c \cdot \tilde{y} + d \tag{2.7}$$

Taking this calibration as a reference, one can move further and apply higher order polynomial to correct the visible distortion in the image. As illustrated in Fig. 2.19, we can see the distortion in the aligned calibrated image of the MCP detector, which will now lead us to correct the positions and reconstruct the image.

2.5.8 Second-order correction

We will go for the second order correction, which requires second order correction polynomial as shown in eq. (2.9). In the equation, X_c and Y_c are the corrected positions of a calibrated point, $(\tilde{X}, \tilde{Y})$ are the non-corrected positions obtained from eq. (2.6) & (2.7), and p_i and q_i, with i ranging from i=0 to 5, are parameters determined by a fit using all the calibration points on this hole region uniformly distributed through the mask surface and setting (X_c, Y_c) to their physical positions. The fitted values of these parameters for all complete hole regions are saved separately in a file for the need to

apply a higher-order correction function. The obtained accuracy and improvement after applying higher order correction of second order is illustrated using Fig. 2.20.

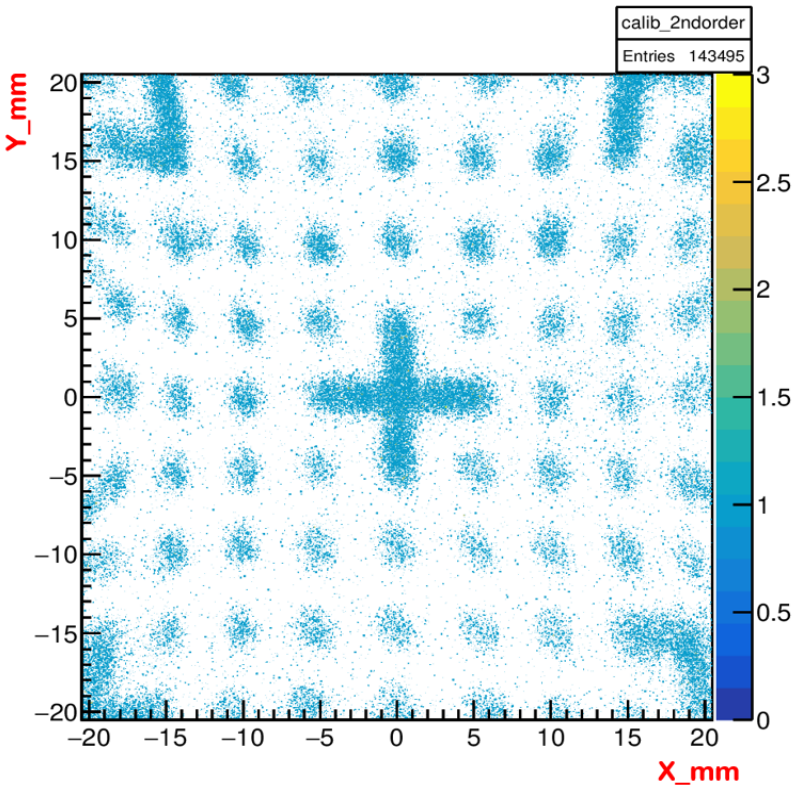

Figure 2.21 – Detector image reconstructed after applying the second order correction polynomial as shown using eq. (2.8) & (2.9)

$$X_c = p_0 + p_1\tilde{X} + p_2\tilde{Y} + p_3\tilde{X}^2 + p_4\tilde{Y}^2 + p_5\tilde{X}\tilde{Y} \tag{2.8}$$

$$Y_c = q_0 + q_1\tilde{X} + q_2\tilde{Y} + q_3\tilde{X}^2 + q_4\tilde{Y}^2 + q_5\tilde{X}\tilde{Y} \tag{2.9}$$

2.5.9 Third-order Correction

The regions near the outer edges, which are not yet nicely visible and do not exhibit complete holes, are mostly affected by the stray electric field on the edges and are ruled out from the analysis. We have discussed it in detail in a later section. This only reduces the usable area of the MCP by less than 20% as calculated by excluding the edges and avoids using a complex correction algorithm for regions with distorted shapes. In this case, the corrected position of a calibrated point was determined using third-order correction polynomials on the values of (X_c, Y_c) where the p_i and q_i coefficients range from i=0 to 9, see eq. (2.10) and (2.11).

$$X_d = p_0 + p_1X_c + p_2Y_c + p_3X_c^2 + p_4Y_c^2 + p_5X_cY_c + p_6X_c^3 + p_7Y_c^3 + p_8X_cY_c^2 + p_9X_c^2Y_c \tag{2.10}$$

$$Y_d = q_0 + q_1 X_c + q_2 Y_c + q_3 X_c^2 + q_4 Y_c^2 + q_5 X_c Y_c + q_6 X_c^3 + q_7 Y_c^3 + q_8 X_c Y_c^2 + q_9 Y_c X_c^2 \tag{2.11}$$

The optimum parameters are easily obtained by fitting a surface in a 3-D plot, as shown in Fig. 2.22. To do so, we first created a 3-dimensional histogram and filled it with measured values of x and y for each point taken into the calibration corresponding to their real values in the x and y direction separately in the mask. Furthermore, we fit this obtained histogram using the third-order correction function as illustrated using Fig. 2.11. The level of correction achieved is fairly acceptable, as

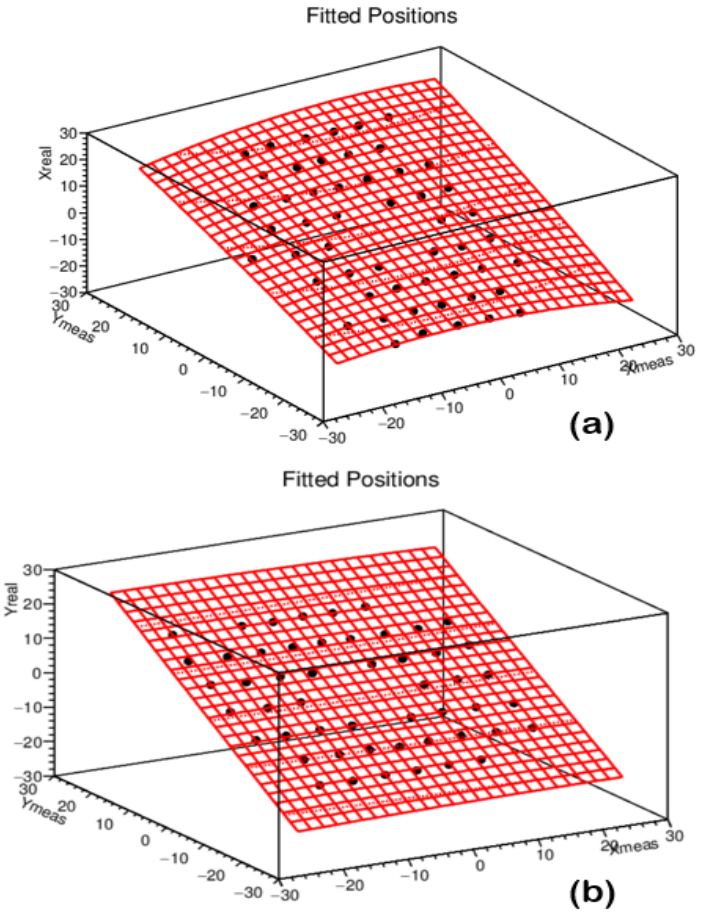

Figure 2.22 – 3-D histogram projected for (a) calibration in x, (b) calibration in y.

shown in Fig. 2.23, to formulate the detector resolution in position in the following step.

2.5.10 Electrical leakage fields

In the following, the choice of stopping at third-order correction in position reconstruction will be justified. Let's assume once the electrons leave the MCP back plate, they will experience an attractive force coming from the position-sensitive anode biased with less negative potential than the plate. Ideally, we assume that the

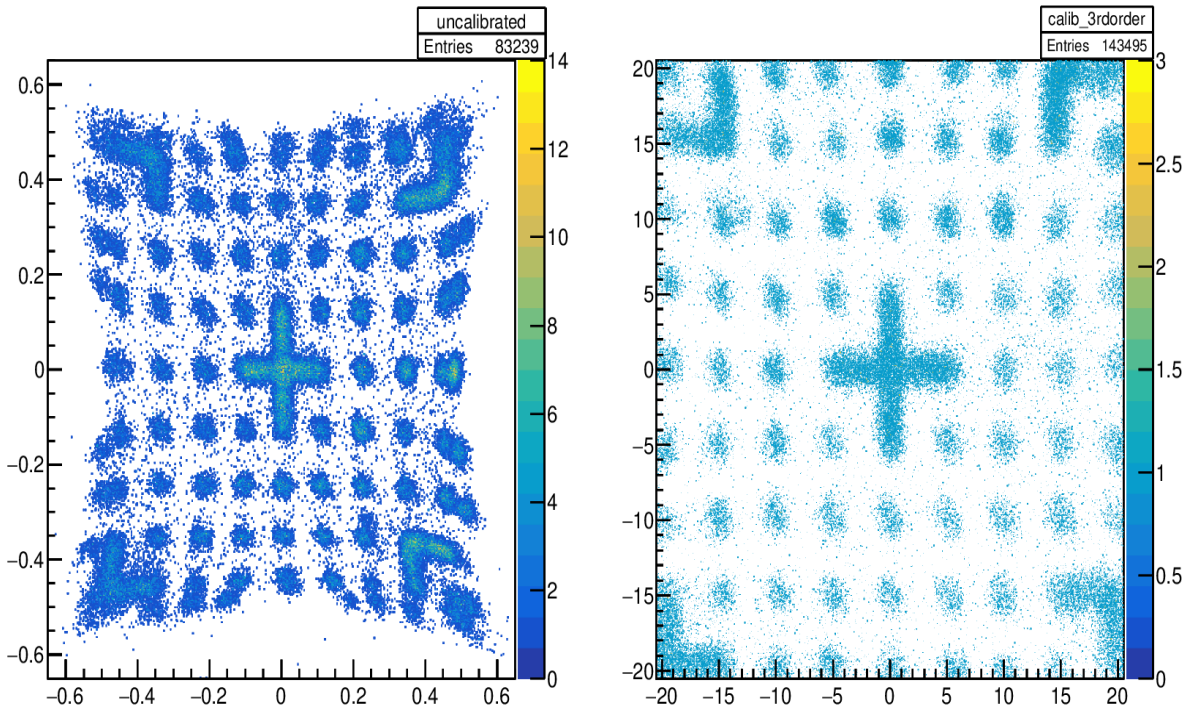

Figure 2.23 – Comparison of higher order polynomial corrections applied on calibrated detector image. The left histogram shows the raw detector image constructed using four localization charges, and the one on the right shows a much better outcome after applying the third-order polynomial correction.

electric field in between the MCP plates and the anode has only one component which is perpendicular to the plates $\vec{E} = \vec{E}_{\perp} = (0, 0, E_z)$. Thus the trajectories of the electrons will follow a straight line perpendicular to the biased plates. However, some secondary sources can create a small electric field with some parallel components $\vec{E}_{\parallel} = (E_x, E_y, 0)$. In that situation, the trajectories of the electrons will deviate slightly from the usual trajectory since there will be an extra force acting on them $\vec{F}_{\parallel} = (F_x, F_y, 0)$.

$$\frac{d\vec{p}_{\parallel}}{dt} = \vec{F}_{\parallel} \tag{2.12}$$

Since the distance between the two MCP plates is small, the time of flight of the electrons will be small as well, and in that sense, we can smoothly say that the force they will experience will not change much during their travel, and we can assume that $\vec{F}$ does depend neither on time nor on z. In this sense then, we can solve Eq. (2.12) easily:

$$\Delta\vec{p}_{\parallel} = \vec{F}_{\parallel}\Delta t \implies \Delta\vec{v}_{\parallel} = \frac{\Delta t}{m_e}\vec{F}_{\parallel} \tag{2.13}$$

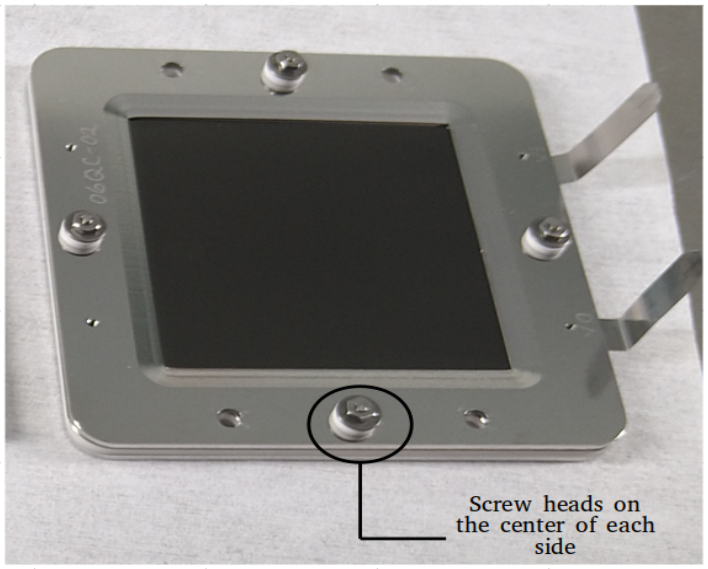

Figure 2.24 – MCP backplane showing four visible screws maintaining the stack together in the RIDE assembly

If we consider now that the velocity of the electrons initially has no parallel component, we find that the change in position from the ideal case is approximately

$$\Delta x \sim \frac{\Delta t^2}{2m_e} F_x \tag{2.14}$$

$$\Delta y \sim \frac{\Delta t^2}{2m_e} F_y \tag{2.15}$$

Recollecting here, $F_x = q_e E_x$. This electric field will come from some charge distribution in some tiny conductors in between the plates or in the vicinity of the plates that will get polarized due to the applied tensions, for example, bolts, holders, screws, etc. Since the electrons will travel far away from these elements, we can consider them as if they were some effective point-like charges Q_j located at the edges. Under these circumstances, we can reformulate the electric field, for instance, in the x direction as:

$$E_x = \sum_j \frac{Q_j}{4\pi\varepsilon |\vec{R} - \vec{r}_j|^3} (x - x_j) \tag{2.16}$$

Here $\vec{r}_j = (x_j, y_j)$ is the location of the effective charge Q_j, and $\vec{R} = (x, y)$ is the location of the electron (here we can neglect the z components since the distance between plates is minimal). To locate the position of these effective point-like charges, we have performed a simulation of the electric field inside the plates as it is depicted

in Fig. 2.25.

We can clearly see that these charges would be mainly located at the screws on the edges, at the positions (d,0), ($-d$,0), (0,d), (0,$-d$), see Fig. 2.24, where d is the distance between the bolts and the center of the plate if we assume that they have the same charge Q. Under these circumstances, the electric field can be formulated as follows:

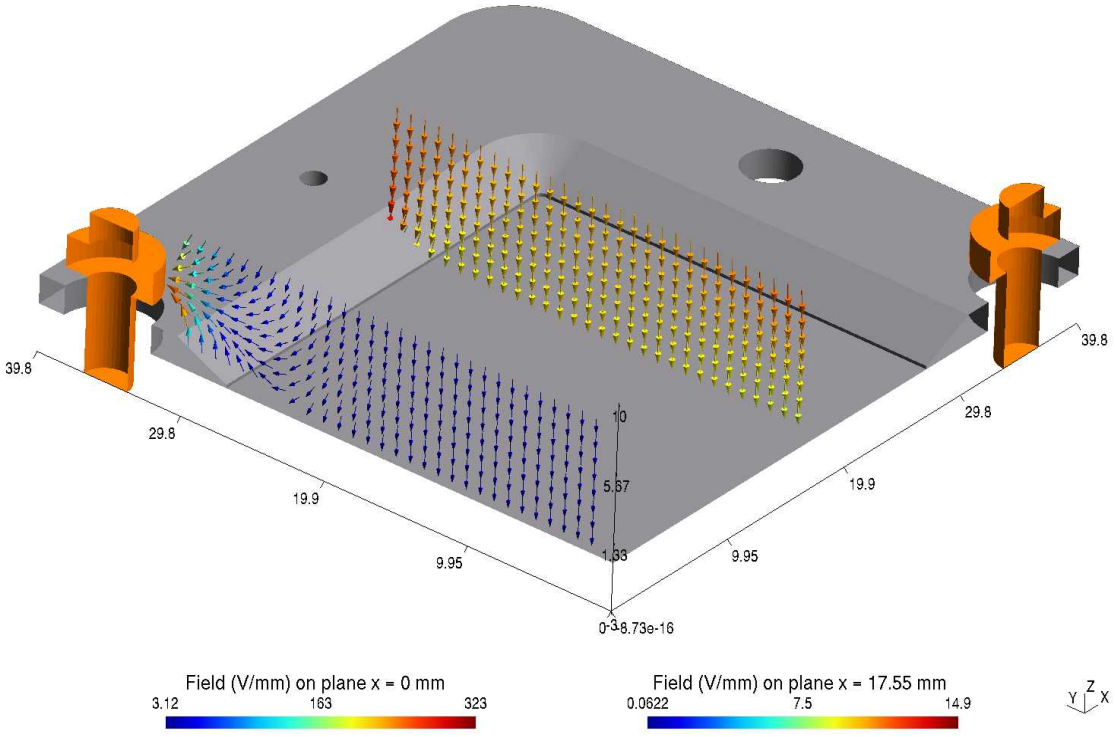

Figure 2.25 – OuroborosBEM simulation illustrating the E field behaviour towards and away from the center screws, the screws are at the same potential as the MCP front plate; the force exerted on electrons points away from the edge and towards the center of MCP plates due to negative charge of secondary electrons

$$E_x(x,y) = \frac{Q \times (x-d)}{((x-d)^2+y^2)^{3/2}} + \frac{Q \times x}{(x^2+(y-d)^2)^{3/2}} + \frac{Q \times (x+d)}{((x+d)^2+y^2)^{3/2}} + \frac{Q \times x}{(x^2+(y+d)^2)^{3/2}} \tag{2.17}$$

By doing the Taylor expansion up to third-order terms, we get:

$$E_x(x,y) \approx \frac{-2Qx}{d^3} - \frac{11Qx^3 - 24Qy^2x}{d^5} + ... \tag{2.18}$$

We see linear and cubic components only because of the symmetry of sources creating the transverse component.
Now, if we consider different charges on each bolt (Q_R,Q_L,Q_T, and Q_B), E_x would be

(2.19):

$$E_x(x,y) = \frac{Q_R \times (x-d)}{((x-d)^2+y^2)^{3/2}} + \frac{Q_T \times x}{(x^2+(y-d)^2)^{3/2}} + \frac{Q_L \times (x+d)}{((x+d)^2+y^2)^{3/2}} + \frac{Q_B \times x}{(x^2+(y+d)^2)^{3/2}} \tag{2.19}$$

Taylor expanding (2.19), we get

$$\begin{aligned} E_x(x,y) \approx & -\frac{Q_R - Q_L}{d^2} + \frac{(Q_T + Q_B - 2(Q_R + Q_L))x}{d^3} \\ & - \frac{6(Q_R - Q_L)x^2 + 6(Q_B - Q_T)xy + 3(Q_L - Q_R)y^2}{2d^4} \\ & - \frac{(3(Q_T + Q_B) + 8(Q_L + Q_R))x^3 - 12(Q_R + Q_B + Q_T + Q_L)y^2 x}{2d^5} \end{aligned} \tag{2.20}$$

We can see now some quadratic terms, but they are only meaningful if the differences (Q_R - Q_L) and (Q_T - Q_B) are prominent. So, in this case, we would have important contributions from linear and cubic terms but mild contributions from the quadratic terms.

And hence, the symmetry of the electric field will suppress the even terms of the Taylor expansion. This could explain why the third-order correction produces remarkably better results than the second-order one. One should additionally note that the four screws naturally give rise to an octupolar potential (four *positive* and four *negative* poles relative to each other). An octupolar potential yields a 3^{rd} order force component. Such a component is therefore expected to be dominant in the image reconstruction of the RIDE detectors. With only odd orders contributing and the suppressed expansion at higher orders (5^{th} and higher), stopping at the expansion at 3^{rd} order is quite justified.

2.5.11 Position resolution

The FWHM spatial resolution is the sum of terms related to the geometry of the particle interactions and terms related to the readout element/signal processing chain.

Since each channel of the MCP acts likewise as an independent electron multiplier, the channel diameter and center-to-center spacing determine the MCP resolution. In our case, when the output from the MCP is observed using the position-sensitive anode, the spatial resolution also relies on the MCP electrode depth penetrating the channels, the space between the MCP and the mesh, and the accelerating voltage for the incident ions. The spatial resolution of an MCP used in the MORA framework in a chevron-stacked configuration is less than that of a single MCP because it spreads into many channels as it enters the later-stage MCP. It is mainly dictated by the PTFI anode, usually of the order of 1mm, due to the thickness of pads and imperfect barycentric reconstruction, and the increased gain makes greater the electrostatic

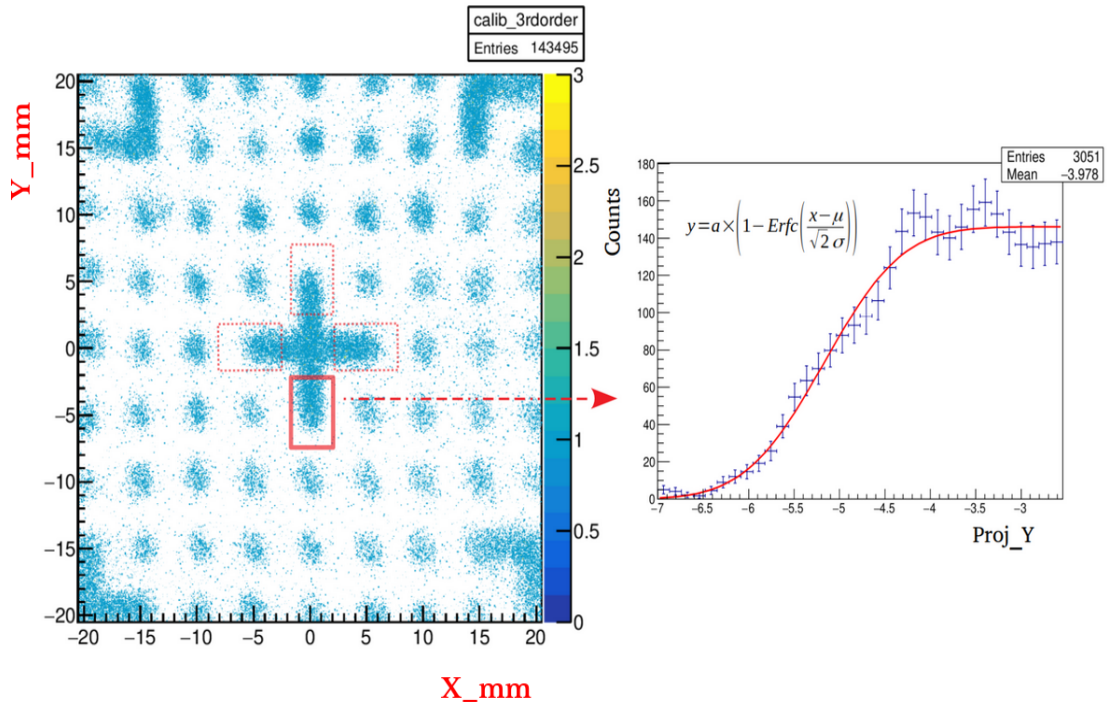

Figure 2.26 – Graphical cut of a 4.55mm a portion of the cross on each side, in the right inset, the fitted projection spectrum in the y plane with an error function.

repulsion in the space when the electrons are released from the MCP.

To determine the resolution, we considered the big cross in the center of the calibration mask exhibiting a thickness of 5mm. We take a graphical cut of a 4.55mm portion of the cross on each side, as illustrated using Fig. 2.26, and project them in the x and y plane. In ideal cases, the projection spectrum should be a step function once these portions are projected on both planes. Since the MCPs have a finite resolution, the step function evolves into an error function, which can be defined as:

$$Erfc(x) = 1 - Erf(x) \tag{2.21}$$

$$Erfc(x) = \frac{2}{\sqrt{\pi}} \int_x^{\infty} e^{-t^2} dt. \tag{2.22}$$

Thus, we fitted these projections with a function F(x) as defined using eq. 2.23

$$F(x) = a \times \left(1 - Erfc\left(\frac{x - \mu_1}{\sqrt{2}\sigma_1}\right)\right) \tag{2.23}$$

where:
a is the normalization factor
μ is the positions of the falling/rising edge, and
σ corresponds to the Gaussian smearing width of the edge in x/y plane

which accounts for the Position resolution. The results of the fit yield a resolution of 0.8 $\pm$ 0.4 mm in x and 0.9 $\pm$ 0.4 mm in y. Following this, we also achieved a position accuracy of better than 80μm in x and y for the holes fully reconstructed after applying the third-order correction.

2.5.12 Conclusion

In this test, we constructed the detector's raw image using the four localization charges collected from the anode using an x and y position estimator approximation. We could further use this information to correct the image and reconstruct it to achieve the best possible precision in determining the particle detection position with high resolution.

We have utilized correction polynomials up to the third order and got a good agreement with the physical position of the holes in the calibration masque and in the corrected real data. This test has been further continued to determine position resolution with high accuracy. It is found a resolution of 0.8 $\pm$ 0.4 mm in x and 0.9 $\pm$ 0.4 mm in y with position accuracy of better than 80μm in the center part of the detector image.

It is proposed the usage of two different in-situ calibration masks. The new design of the mask, as already mentioned in the last sections exhibiting all the required changes, has been done and can be seen in Fig. 2.27.

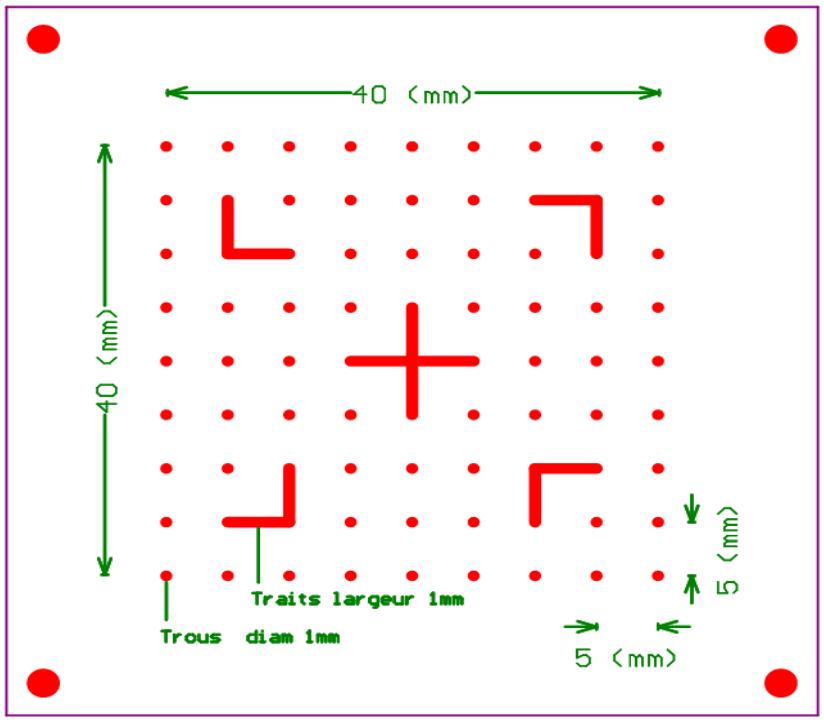

Figure 2.27 – Improved/new version of in -situ calibration mask specially designed to avoid prominent disturbances and distortions on the edges of the raw detector image, the new design exhibits the shift of L openings 5mm from each side towards the center

- One dedicated to applying the image reconstruction procedure consists of uniform hole distribution throughout the mask and inferring precisely the resolution of the image obtained after applying the reconstruction algorithm.
- Another mask specially designed for the correct position determination of the trapped ion cloud consists only of corner L-shaped openings and a central cross. One needs to be careful while designing these masks as we have seen the disturbances and distortions in the detector image more prominent on the edges, and that's why it is advised for the next design to shift the corner L openings 5mm from each side towards the center.

2.6 Test-3: Absolute Efficiency Measurements

2.6.1 Goal

For many experiments, the absolute detection efficiency ϵ of an MCP is an important parameter. It describes the probability that an impacting particle (photon, electron, or ion) triggers a signal on the detector. In the case of coincident multiple particle detection systems, high efficiency is essential, as the efficiency for detecting n particles scales with ϵ^n.

The efficiency parameter of an MCP depends on various factors, such as the particles' mass and kinetic energy to be detected. The standard approach to do so is by considering the measured ion currents in a Faraday cup and the MCP count rate. The MCP detector's efficiency can be deduced by measuring the intrinsic ratio of two contributions. To clarify the functionalities of the Faraday cup, we remind here of a few features. They are current collectors generally simple to construct and are fast and accurate. These collectors are connected directly to current measuring devices, and current measurements as low as a few 10^{-15}A are possible with modern ammeters.

The measurement accuracy is usually affected by a series of secondary processes created by particles impacting a cup, such as the emission of secondary electrons and secondary ions or reflection of charged particles, collection of electrons and ions produced near the cup (for example, produced by ionization of the residual gas or produced at the aperture structure), current leakage to the ground, and the penetration of particles through the cup structure. Escaping of secondary electrons is minimized by a suppressor grid biased to about -100 V, placed directly in front of the collector plates. Faraday cup was well suited for our case, being in the requirement for absolute current measurements because they are not affected by any unknown gain/charge amplification factor. The collection efficiency is 100%. The suppressor grid and geometry of the cup allow for safe neglect of parasitic contributions of secondary sources of charges flying from or to the cup.

2.6.2 Description of the ion gun

We started with a homemade offline ion gun for the efficiency measurement (see Fig. 2.28). It consists of an accelerator electrode close to the pellet allowing a large po-

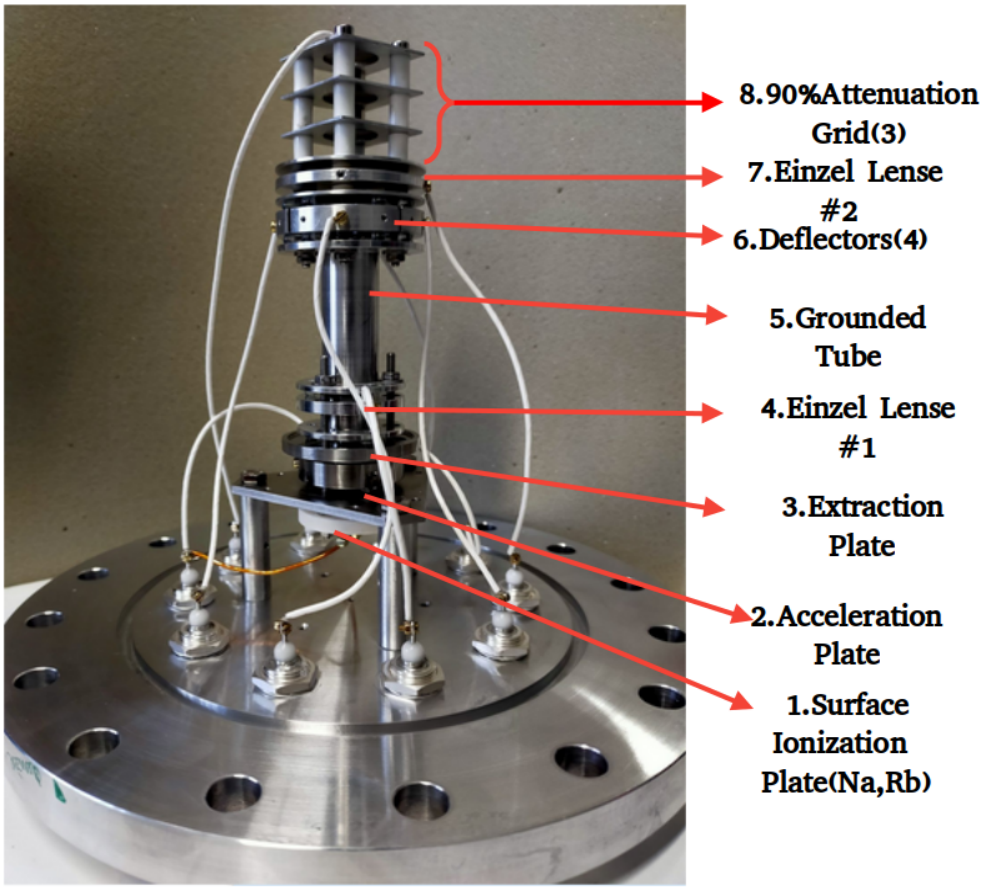

Figure 2.28 – Homemade offline Ion Guide developed at LPC, Caen utilizing surface ionization Na and Rb pellets for offline efficiency measurements

tential difference (1.5 kV) to be applied to these electrodes with respect to the ground tube and of optics responsible for manipulating the trajectory and direction of the ion beam. The following steps were taken into account to accelerate the ions:

- The electrode is connected to a filament passing through the pellet, (1) in Fig. 2.28, at a high voltage of about 1500V. The acceleration electrode (2) is followed by an extraction electrode (3) with a potential of 1400V to extract the ions produced and accelerated after the pellet. The principle of the surface ionization system is explained in a later section.
- The Einzel lens (4), which is in principle composed of three electrodes, operates through a delicate balance between the kinetic energy of the ions and the potential difference between the central and external electrodes to focus / de-focus the beam. The imposed voltage is manipulated between 800 V and 900 V.
- A tube (5) is connected to the ground where the ions transit and helps to focus the beam.

- Deflectors (6) allow the beam to be oriented in the desired direction. In reality, this adjustment can be very delicate, which makes the required adjustment very difficult. Out of 4 deflectors, we have utilized two to adjust the direction of the ion beam falling onto the detectors.
- Sufficient voltages had to be applied to the deflectors to get a focused parallel beam.
- In a second Einzel lens (7), the applied voltage is between 800 V and 900V to further focus the ion beam.
- A succession of three attenuation grids (8) with a mesh parameter of only 10 % transmission. These grids, therefore, allow 1/1000 of the ions to pass through. The attenuation is an important parameter to restrict the counting rates from being too high on the MCP detector (at most, a few 10kHz). The potentials applied to the ion gun optics are obtained by a small simulation using the SIMION toolkit.

2.6.3 Surface Ionization principle

In a solid material, for example, a metal such as Tungsten (W), electrons are present with different energy states. Note that Tungsten is a refractory metal extremely resistant to heat and wear. Additionally, Pauli's principle requires each electron to have a different wave function involving a different energy level or spin. As a result, electrons occupy higher and higher energy levels within the material. In the case of the ion source, a filament with resistance passes through the Sodium or Rubidium pellet. By applying a voltage, it starts to heat (Joule effect). As the temperature of the material (Tungsten) increases, it changes the distribution of electrons on the energy levels; a more significant fraction does migrate to higher energy levels. Sometimes, they can store enough energy to escape the material. This energy should be compared to the material's work function: the work function is, by definition, the required energy for an electron to escape a material.

We have utilized an offline alkali ion source, a pellet, to produce ions accelerated at different energies. When a layer of atoms (here Na) covers the material's surface (Tungsten), their external electrons can populate the higher energy levels of the material. Suppose the atoms are desorbed from the surface (by heating). In that case, a fraction will be evaporated as ions, depending on their potential of first ionization and the material's work function.

The Saha-Langmuir equation is usually employed to calculate the ratio of the number of atoms desorbed in the form of ions (n_i) and neutrals (n_0) according to the work function of the base material (ϕ_s) and of the first ionization potential of the desorbed atom (ϕ_i):

$$\frac{n_i}{n_0 + n_i} = (1 + \frac{g_0}{g_i} \times e^{\frac{(\phi_s - \phi_i)}{kT}}) \tag{2.24}$$

where: T is the temperature (K), (go/gi) the ratio of the statistical weights of neutrals to ions, and k the Boltzmann's constant.

In our case, the pellet is made of ^{23}Na atoms to be ionized, which are contained in a matrix of aluminium oxide to withstand high temperatures. Imposing a voltage at the terminals of the filament connected to a resistance heats the source very significantly, excites the Na atom, and allows the production of ions. The ionization potential of Na atoms as any alkali ion is small, ϕ_i=4.2 eV. At the same time, the work function is higher for Al_2O_3, of the order of 4.7eV, which gives a good ionization probability, even at rather low temperatures according to the Saha-Langmuir equation 2.24. The pellet manufacturer (Heatwave labs) indicates temperatures around 1200°C for evaporating the alkali elements.

2.6.4 SIMION Simulations

Here is the introduction of the Monte Carlo package, SIMION[98], used to study the ion beam behaviour through an offline surface ionization source. SIMION generally provides extensive supporting functionality in geometry definition, user programming, data recording, and visualization and presents an affordable and versatile platform. SIMION's methods are reasonably direct via finite difference methods (optimized over-relaxation and multi-mesh methods) and Runge-Kutta for solving the required partial differential equations (PDEs), particularly the Laplace Equation and ordinary differential equations (ODEs), respectively.

A workbench strategy allows us to have multiple meshes, or possibly different mesh sizes and symmetry, used in the same simulation. Geometries can be defined via multiple methods, like files from a 2D/3D CAD model, using certain libraries and different available versions of geometry files.
In this case, we used a dedicated geometry text file with an extension of *.GEM* to define electrode geometries using constructive solid geometry primitives. These operations help us to define shapes using unions and intersections of other basic shapes. *SIMION* converts this *.GEM* files to a *potential array* (PA) file. The potential array is a mesh of points in space, and its purpose is to store electrode geometries and the potential at each point in that geometry.

With the help of a *LUA* code, which is the main programming language embedded inside the *SIMION* software, we can define the random ion generation, which follows the Maxwell distribution, and also define the positions, mass, charge, direction, velocity, and time of birth of these ions. The simulation result is shown in Fig. 2.29. This figure shows that using suitable geometry and applying a correct set of voltages on the different lenses, it is possible to make the ion beam spray the whole surface of the MCP detector.

2.6.5 Test Preparation

Before commencing this critical measurement of the absolute detection efficiency of the RIDE detector, we obtained the detector image using the same calibration mask in the presence of ions generated from a surface ionization Na pellet.
To achieve a full image of the detector or, in other words, the total exposure of the active area of the detector to the ions coming through, we had to do some modifications

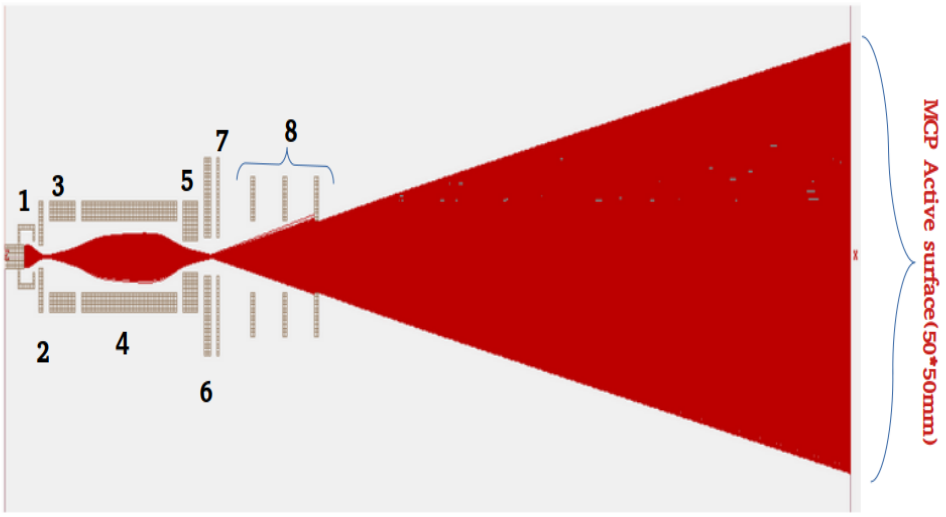

Figure 2.29 – Offline ion guide simulation using the SIMION toolkit, [1] Surface ionization pallet, [2] Acceleration Electrode, [3] Extraction Electrode, [4] Einzel lens-1, [5] Grounded Tube, [6] 4-Deflectors, [7] Einzel lens-2, [8] 3×Attenuation Grid.

to the setup compared to what was simulated in SIMION, including the ion optics (offline ion guide), electronics (few changes in voltage divider) and also the source-detector positions.
The procedure to obtain the detector's raw image in the presence of ions went through the following advancements/modifications:

- We chose to increase the diameter of the openings, which were covered by the three attenuation grids, by about 10 mm, by increasing them to 16 mm; to obtain a much wider illumination and more uniformly toward the detector. The results were still not convincing due to the presence of conductive glue used to attach these meshes, which was allegedly the reason for obstructing a part of the mesh.

- We continued these modifications to attach the attenuation grids with the screws directly and to avoid the use of glue, allowing a more uniform illumination of the detector. We obtained an image with an improved resolution, but the beam seemed very focused/centered.

- The problem seems to come from the fact that the beam is too converged before arriving on to the detector, a fact that is not predicted by the SIMION simulation. A solution that may allow a bit more divergence to the beam to illuminate the detector is to remove the lenses converging the beam too much and instead replace them with attenuation grids.

- The result obtained was a more illuminated image, not uniformly but more precise, with a resolution of the mask points. Then, we used another ion source configuration to focus the beam a little less by replacing the lenses with the attenuation mesh. We initiated by measuring the current using a Faraday cup, see Fig. 2.30.

2.6.6 Test Methodology

As soon as we were convinced the beam was well focused on the MCP detector, we resumed our tests to measure the efficiencies.
The idea of performing the efficiency tests starts in the following manner. Before reaching the MCP front plate, the ions are accelerated with the energy of 1.5 keV (acceleration electrode potential), which means the ions leave the pellet at this particular energy. The idea behind this is as we increase the negative voltage in front of the MCP

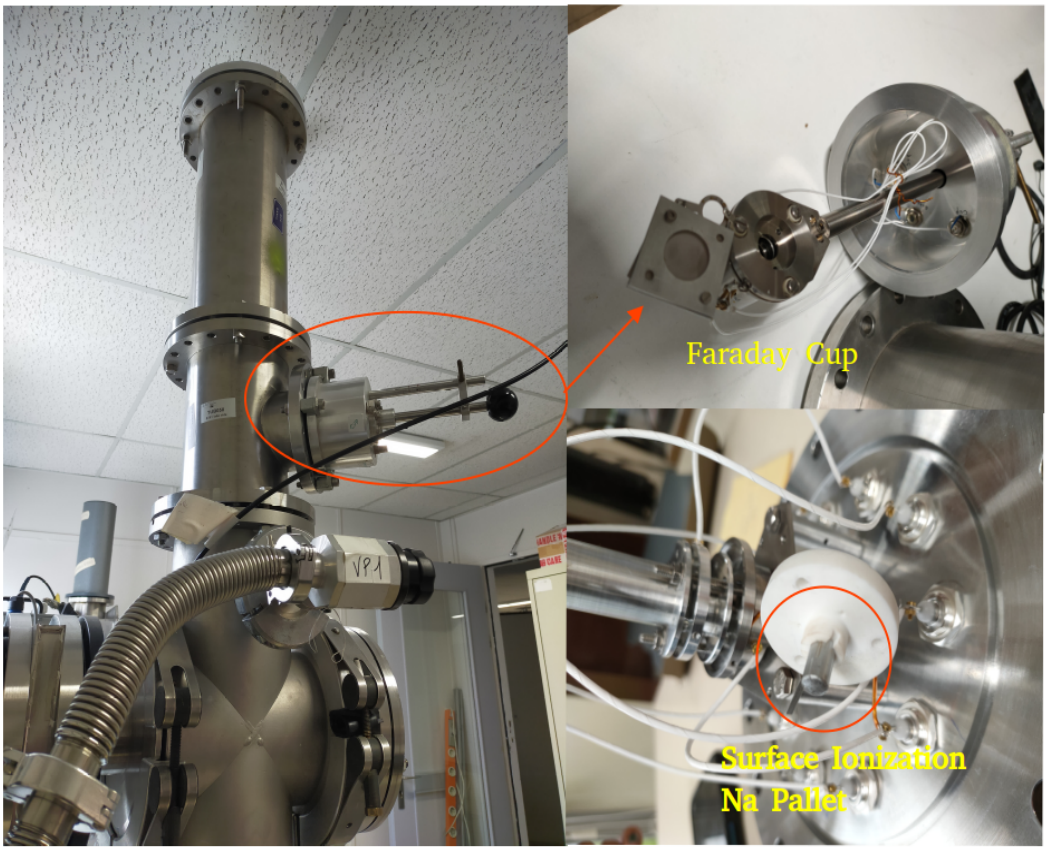

Figure 2.30 – Test bench components showing the vacuum chamber modified from the first version shown in Fig. 2.11 for new installation of Faraday cup to measure ion currents and Surface ionization Na pallet in offline ion guide.

detector, we measure ions with greater velocities since a greater potential difference accelerates them. We can test the efficiency of the MCP detector as a function of the

incident energy. To perform this efficiency test concerning the energy of ions reaching the detectors, we modified the voltage divider circuit used in our previous tests, see Fig. 2.8.

In principle, this modification includes two input voltages before the divider bridge to vary the energy of ions when they hit the front MCP plate while maintaining a safe potential difference between the MCP front and back plate. The new version of the modified voltage divider is illustrated using Fig. 2.31. Although this modification

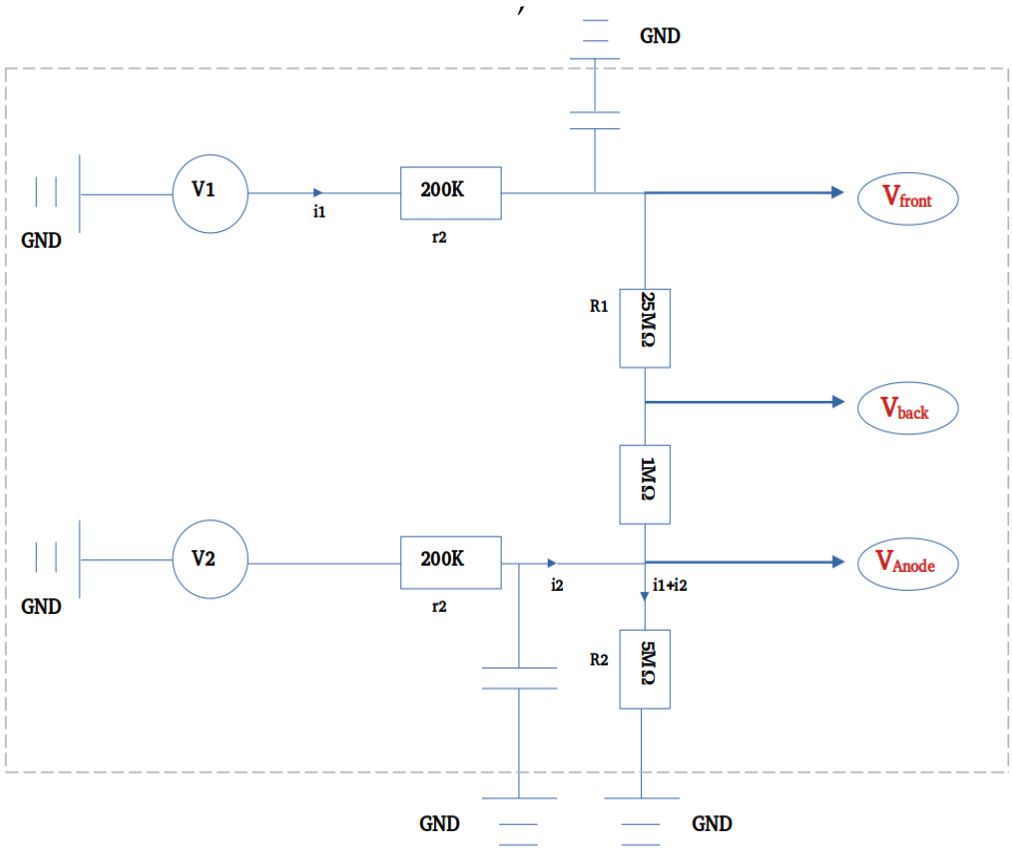

Figure 2.31 – Modified version of the voltage divider to perform efficiency measurement test with varying ion energy.

in the voltage divider circuit was done in several steps, we first disemboweled the already existing version of the voltage divider. We tried to achieve V_{front}-$V_{back} \in$ [1700,2000]V with two input voltages, addressed as V1 & V2, and we implemented the new circuitry. To avoid any intricacy, the modification with the anode was not included in the beginning. The confirmation of the proper functioning of the modified voltage divider was done in steps.

We did a small trial by putting lower potentials and biasing V1 and V2 with 0 and 20 volts and vice-versa to see what we measure on the other side after the divider on V_{front} and V_{back}. This stage helps to calculate the correction coefficients. A short

illustration of how we proceeded is presented hereafter. We know,

$$V_{front} = \alpha V1 + \beta V2 \tag{2.25}$$
$$V_{back} = \alpha' V1 + \beta' V2 \tag{2.26}$$

It is possible to determine the values of the coefficients α, βexperimentally, α', β' by applying small voltages on $V1$ and $V2$. The determinant of this system of linear equations corresponds to the following:

$$\delta = \alpha\beta' - \beta\alpha' \tag{2.27}$$

So,

$$V1 = AV_{front} + BV_{back} \tag{2.28}$$
$$V2 = CV_{front} + DV_{back} \tag{2.29}$$

the correct values of V1 and V2 voltages are calculated with

$$\text{A} = \frac{\alpha}{\delta}, \text{B} = \frac{\beta}{\delta}, \text{C} = \frac{\alpha'}{\delta} \quad \text{D} = \frac{\beta'}{\delta}.$$

After this voltage calibration, we utilized a homemade Faraday cup to estimate the number of ions exposed to the detector. We carefully moved ahead to the following parameter of beam chopping, a technique that periodically interrupts the continuous ion flux. We utilized a Behlkey switch ($\pm 3kV$) attached to a deflector power supply to produce pulses of 2 μs (t) every 10ms of the cycle (T).

The first step after the modification was to verify the efficiencies as a function of MCP biasing voltage. This particular test is essential to mitigate any severe risk to the detector because of excessive counts. We observed higher counts as soon as the biasing voltage was increased and reached its nominal value. The retained voltage here was kept close to 1750 to 1850 Volts. To accumulate the real number of ion counts on MCP, we used the convenience of having TOF spectra according to the beam-chopping signal, see Fig.2.32 We compared this number with the measured current on the Faraday cup to determine the absolute detection efficiency. The efficiency was calculated using the formula:

$$\epsilon_{abs} = (MCP_{ions} - MCP_{background})/FC_{avg} \times e/d \times \mu_{att}/T \tag{2.30}$$

where:
ϵ_{abs} = Detector absolute efficiency
MCP$_{ions}$ = corresponds to the no. of counts when the MCPs are exposed to ions
MCP$_{background}$ = Observed background on detectors in the absence of ions (counts estimate taken from the neighbouring channels of TOF-spectra where we do not see the ion peaks)
FC$_{avg}$= Average measured current on the Faraday cup before and after the measurement
e = electric charge
d= duty cycle corresponds to the ratio of chopping window (t)and chopping cycle (T)

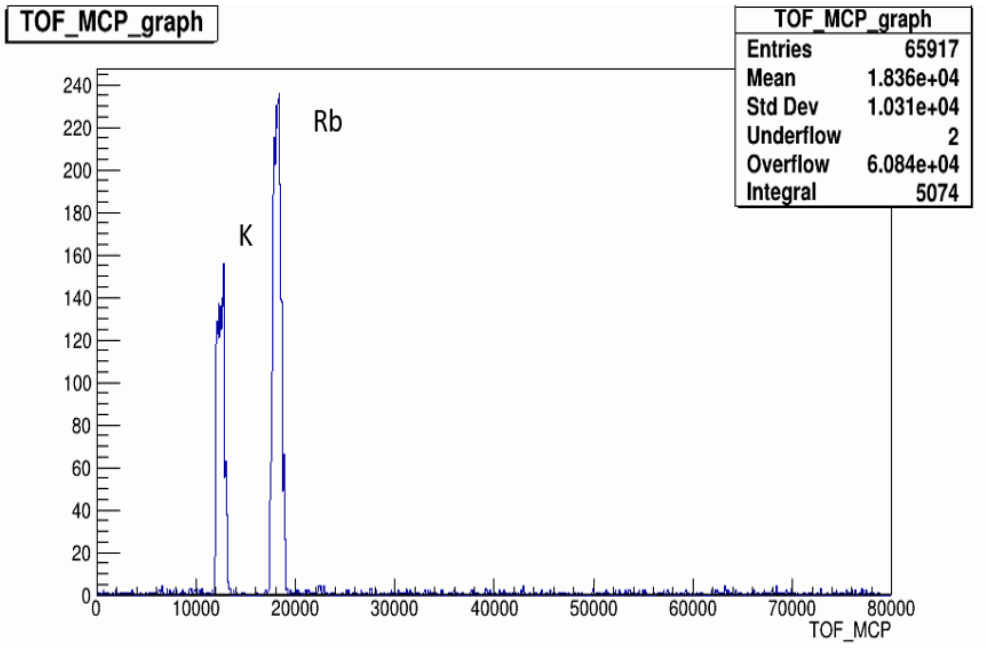

Figure 2.32 – TOF spectra showing peaks of K, Rb from surface ionization Na pallet

μ_{att} = Attenuation factor (10%) of the mesh in front of MCP.
T = Acquisition time

As mentioned earlier, the efficiency was computed by considering each contributing parameter in the equation. To include the uncertainty factor σ on the measured efficiency, the error bars are computed taking into account the average value (FC$_{avg.}$)and difference in measured current on the Faraday Cup (**FC**$_{diff}$). and the absolute value of efficiency (ϵ_{abs}).

$$\sigma = abs(FC_{diff.}/2)/\epsilon_{abs} \times FC_{avg.} \tag{2.31}$$

2.6.7 Test Results

The result obtained in this test is shown in Fig. 2.33, .where we can see the detection efficiency reaching the maxima at 45 % and experiencing the saturation with ions of energy 3.5-4keV.

2.6.8 Conclusion

With the benefit of this thorough test, we managed to have a fully-fledged test bench to examine the detection efficiency in the case of the RIDE detection system.

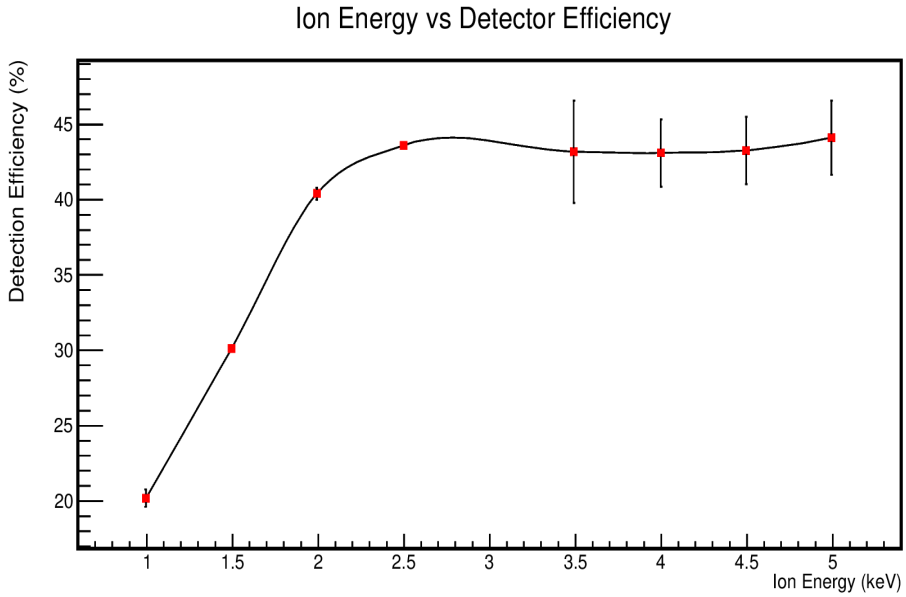

Figure 2.33 – Detector Efficiency scan concerning the energy of the ions. The efficiency attains a maximum value (plateau) at 45%, similar behavior has been observed earlier with delay line anodes [4]

Using an offline ion guide for an efficient transit of ions, we applied switching techniques to the continuous beam flux to reduce the rate of ions on the MCP. With a rate at or above 10^5 pps, we start reducing the life of MCPs. We are in a regime where the electron amplification is no longer optimal, as the MCP does not recover the voltage properly between two pulses. This technique assisted us in determining the detection efficiency concerning the energy of ions.

The efficiency is reaching the maximum efficiency plateau at 45 %, which is quite textbook. Indeed, this maximum efficiency value is mainly due to dead zones in the detector for ion detection, the microchannel mesh. We also have witnessed saturation at a point ranging from 3.5 to 5 keV, mimicking the behaviour of such a detection system as observed in past experiments using delay line anodes [4].

2.7 Closing comments & foreseeable Improvements

To give a quick rundown of all the difficulties we have faced during this procedure, we would like to mention some of the problems we encountered during efficiency test measurements.

1. During these tests, apart from one set of MCPs provided by the manufacturer *Photonis* as a prototype, we observed a very high background, a noise rate as high as 1000 counts/sec, well above the thresholds, at 1700Volts of biasing potential in between the two plates, and even below.

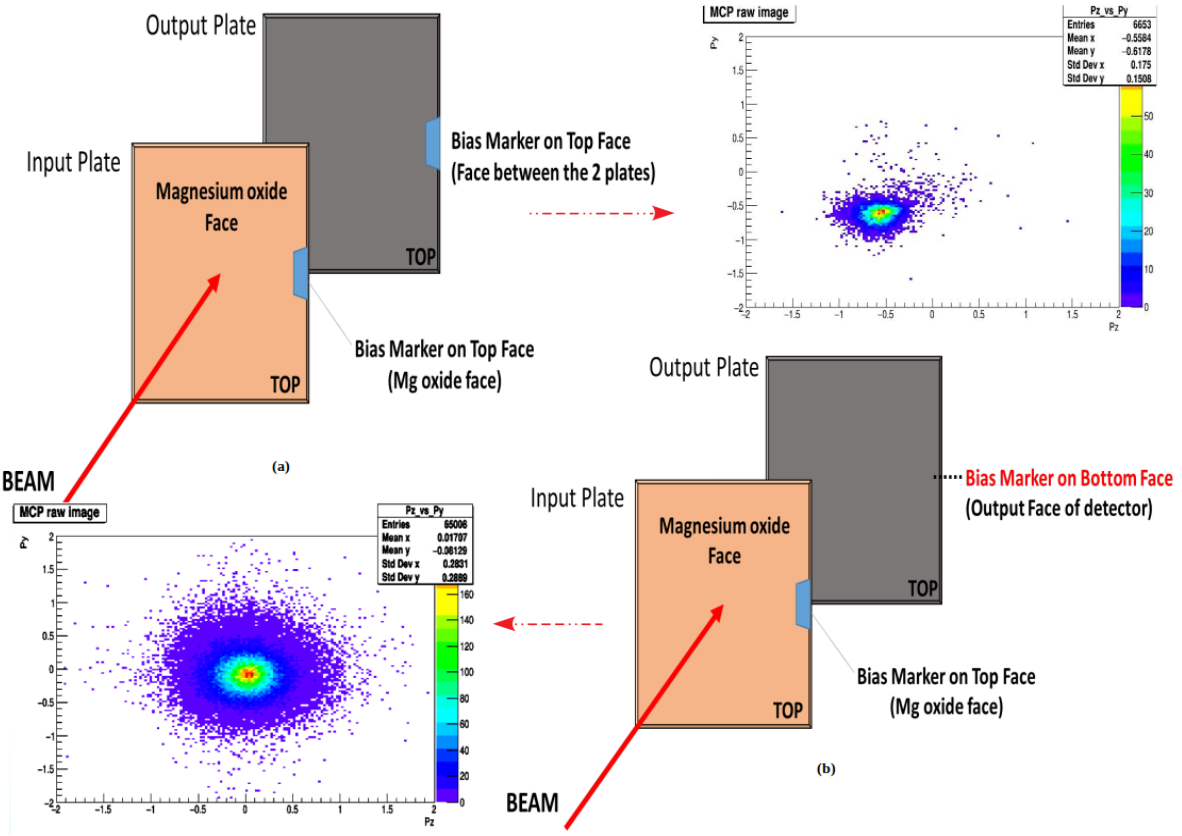

Figure 2.34 – (a) MCP stack(front+back plates), aligned channels giving rise to the high background as visible on edge in the absence of the biasing potential (b) Modifications (flipping of the back plate) to achieve 8° alignment in between the channels to fulfill the chevron configuration requirement, centered beam during the efficiency measurement with 1700V bias potential.

2. Only 1 set of MCPs out of the 3 worked with our detector configuration. In all sorts of manipulations, we took much care concerning their storage in better vacuum conditions. We only manipulated them for assembly under a fume hood and in a clean environment within a few hours.

3. At one moment, we suspected that the origin of the problem might be due to the assembly with the conductive screws going through the MCP sets. The high background was consistently observed in the corners of the MCP, visible during the construction of the detector's raw image. As it was pretty evident that there is a focusing effect of the front voltage applied to the screws, also from working MCPs, this sounded like a plausible explanation.

4. A few steps were taken after considering the possibility, as mentioned earlier, to mitigate this issue, which includes their operation under vacuum close to (P$\sim<$ 2.e^{-6}mbar) and with slow biasing, starting with 1300Volts. We added a Kapton insulation on the top of the screws, unable to exchange them with plastic screws (unavailable commercially). We also tested the bare MCPs without the position-sensitive anode. All these measures were proven ineffective.

5. A series of tests with faulty detectors and consistent results each time made us eventually suspect that channels were not in a chevron configuration but aligned. This idea wasn't thought of as the stacks of MCP were directly delivered to us by Photonis, already assembled in their frame. To verify, we flipped the second MCP (input becomes the output), which decrypted the background issues in all the faulty MCP sets.

This error was unfortunately detected only later, when at JYFL, during the many tests we did, as we only disassembled the MCP stacks once or twice, reproducing the erroneous configuration that we observed in the MCP sets provided by the manufacturer. The above-discussed issue showcasing the aligned channels (before) and chevron configuration (after) is illustrated using Fig. 2.34.

Annular SI Detectors

3.1 Motivation

As thoroughly discussed in Chapter 1, this sort of innovative combination of high trapping efficiency, coming from the transparent Paul Trap, and laser polarization techniques, from optical pumping, are being utilized for the first time with correlation measurements in nuclear β decay. To reach the sensitivities close to 10^{-5} in the measurement of the D parameter, we focus on maintaining the polarization degree above 70 %.

In this experiment, we are likely able to reach a polarization degree (P) close to 99% because of the confined ion cloud's prolonged exposure to the laser light. To proceed, we are employing annular segmented silicon detectors in and along the axis

of the MORATrap, see Fig. 3.1. One is installed in a circularly polarised laser propa-

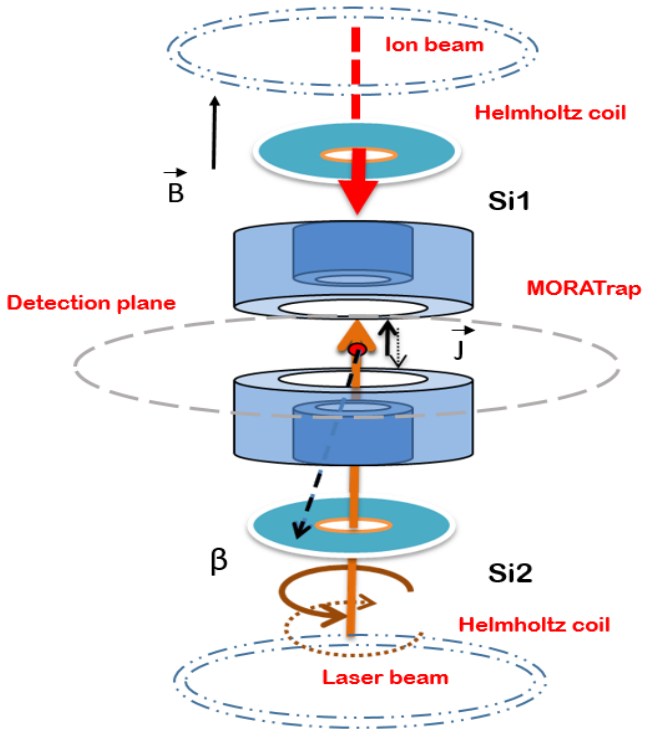

Figure 3.1 – Polarization setup of MORA showing the trap axis and the silicon detectors (Si 1 and Si 2). The superimposition of the laser beam with the ion cloud allows for acquiring the polarization of nuclei of interest. Helmholtz coils are employed around the circumference of the detection chamber to maintain a preferential axis for the magnetic field. The two annular Si detectors upstream and downstream of the trap axis monitor the asymmetry to determine the polarization degree (P).

gation direction, and the other in the opposite direction. We can access the degree of polarization by measuring the beta asymmetry parameter observed between the two detectors taking into account the equation

$$\frac{N_{\beta^+}^{\uparrow} - N_{\beta^+}^{\downarrow}}{N_{\beta^+}^{\uparrow} + N_{\beta^+}^{\downarrow}} \propto A_\beta \cdot P \tag{3.1}$$

where $N_{\beta^+}^{\uparrow}$ and $N_{\beta^+}^{\downarrow}$ depicts the numbers of positrons detected parallel and anti-parallel to the polarization direction, respectively, and P corresponds to the polarization degree. According to the standard model, the value A_β can be inferred from Ft- values for some of the mirror isotopes as done in [99]. From more recent data, it can be recalculated to be A_β = -0.5628 $\pm$ 0.0007 for ^{23}Mg.

The utilized coincidences with recoils measured in the azimuthal plane of the MORATrap, thanks to the recoil ion detectors used in the detection setup, which are also serving for the D correlation measurement, will a priori be preferred to single β events, as coincidences allow to reject a very high background [100]. The coincidence recorded with the recoil ions will constrain the neutrino momentum of the detected events because of the momentum conservation law.

In the case of β's conditioned by the coincident detection of a recoil ion, the asymmetry is reformulated as a linear combination of the β and neutrino asymmetry coefficients. It is calculated with the given equation

$$\frac{N^{\uparrow}_{\beta^+\,coinc} - N^{\downarrow}_{\beta^+\,coinc}}{N^{\uparrow}_{\beta^+\,coinc} + N^{\downarrow}_{\beta^+\,coinc}} = (\alpha \cdot A_\beta + \beta B_\nu) \cdot P \tag{3.2}$$

In this case, $N^{\uparrow}_{\beta^+\,coinc}$ and $N^{\downarrow}_{\beta^+\,coinc}$ are the numbers of coincidences between positrons detected parallel and anti-parallel to the direction of polarization in annular silicon detectors and recoil ions detected in the azimuthal plane of the trap, and α and β are coefficients relying on the solid angle for detection and on the decay parameters. A Monte Carlo simulation can precisely determine these coefficients. B_ν can be inferred with 0.24 % precision from recent ft measurement as done in [99], we calculate: B_ν = -0.7507 $\pm$ 0.0018. With this method, the precision to determine the polarization degree will be better than 2%.

To address the systematic uncertainties arising during the measurement of the polarization degree from non-uniform detection efficiencies, we will invert the polarization direction, which will significantly reduce the systematic uncertainties. Equation 3.2 shows that in the first approximation, the relative accuracy on P will scale as the square root of the number of coincidences recorded in the different β and recoil ion detectors

$$\frac{\sigma_P}{P} \simeq \frac{\sqrt{N^{\uparrow}_{\beta^+\,coinc} + N^{\downarrow}_{\beta^+\,coinc}}}{N^{\uparrow}_{\beta^+\,coinc} - N^{\downarrow}_{\beta^+\,coinc}} \tag{3.3}$$

3.2 General overview of the detector

Before attaining the first proof of laser polarization at the IGISOL-4 facility, we commenced with an initial characterization process at GANIL by testing three identical silicon detectors, and the best two were chosen to be installed on the trap axis for P measurement.

The dedicated silicon detectors were developed by *Micron Tech.* and have been characterized and tested in a dedicated test bench at the GANIL facility and later in the facility of Jyväskylä. The active surface of the employed silicon wafer consists of two annular rings of radius from 7.25 to 19.75 cm and thickness of 1mm, mounted on a hexagonal PCB surface of dimension 52×70 mm, as shown in Fig. 3.2. The actual configuration of these detectors also includes an aluminum protection sheet

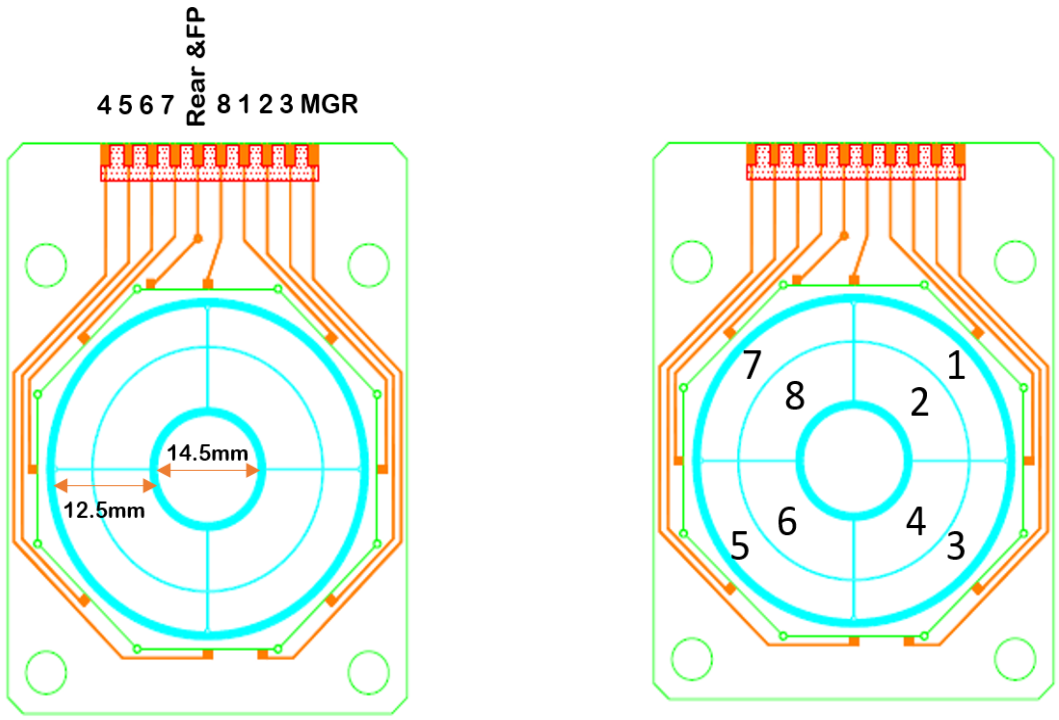

Figure 3.2 – Annular SI detectors technical specifications and dimensions specifying the active region having two rings subdivided into eight sectors and the electrical connections

of 100 μm thickness precisely used to shield the detector's active surface from the bombardment of lasers during the conduct of the main experiment, where the lasers are mainly required to polarize the ^{23}Mg ions. We can see the true detector geometry without the layer of aluminum protection cover in Fig. 3.3.

The purpose of this chapter is to centralize specifically on the characterization of individual sectors of the Si detectors for the fulfillment of measuring light charged particles. The testing setup components include a vacuum system, preamplifiers, and the mandated electronics for the Si detectors. This characterization is done to ease the optimization of energy resolution for future measurements and to investigate further polarization degree measurements.

In addition to the experimental work, in the course of the characterization process, several inquiries were made to purchase the best suitable preamplifiers for such a detection system, taking into account background-related issues, which are also discussed in the later sections.

3.3 Detector Working Principle

Since the 1960s, semiconductor materials have been in use in many fields. They became even more prevalent in nuclear physics when nuclear physicists uncovered that the semiconductor detectors were better than the well-known gas chamber at that

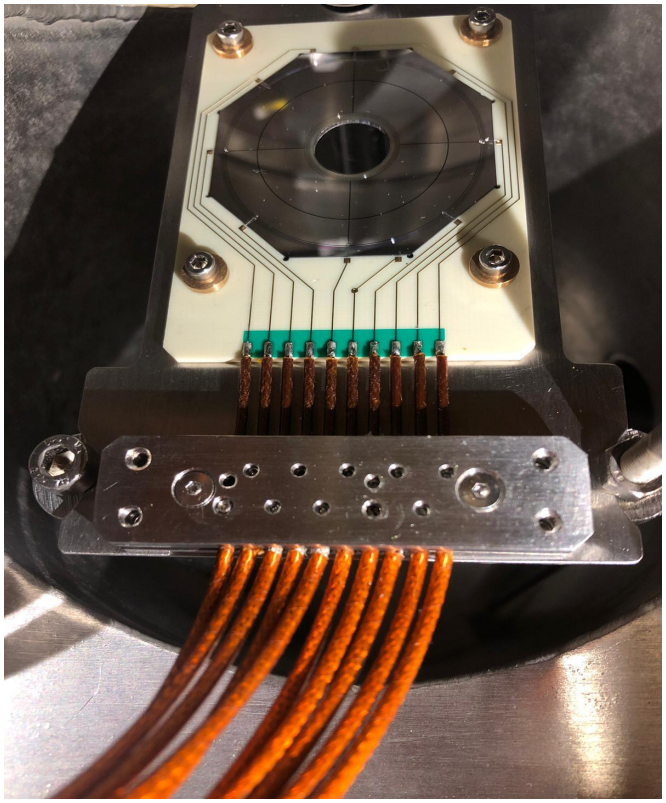

Figure 3.3 – Annular silicon detectors of MORA. Two annular rings are subdivided into eight sectors. In this pictorial representation, the active wafer was without the aluminum protection foil, while it was used during its characterization in the presence of alpha particles.

time. The most crucial difference is that the higher energy resolution in semiconductor detectors is ten times better than in the gas chamber.

This detector is most commonly used when the best energy resolution is intended. As we know, each type of radiation detector produces its intrinsic output product after interaction with radiation. In semiconductors, the fundamental information carriers are electron-hole pairs, which are produced along the path taken by the charged particle (primary or secondary) through the detector. By collecting electron-hole pairs, the detection signal is formed. Silicon and germanium detectors are the most commonly used. Germanium detectors have a finer energy resolution and are generally used for γ-ray spectroscopy, whereas silicon detectors are preferred for charged particle detection.

In principle, Si detectors are an excellent choice for electron detection and have been used since the 1960s. Their backscatter factor on the detector surface is lower than for Ge as this phenomenon depends on the material's atomic number Z. As the atomic number of silicon (Z= 14) is lower than that of germanium (Z= 32), the electrons tend to scatter much less on the surface of a silicon detector. Such detectors have also been improved to perform coincidence measurements. With the high efficiency of this simple detection technique, it can be used to study the decay energy spectrum and measure spectral shapes. The response from a Si detector to a charged particle is

straightforward. For mono-energetic ions, only full-energy peaks are observed. The energy resolution of such detectors is affected by many factors. The signal obtained can fluctuate due to various noise origins, limiting energy resolution. Some of these factors are inevitable, while others can be minimized based on the design of the detector setup and an appropriate experimental environment.

A more fundamental limiting factor is the statistical variance of electron-hole pairs created. The Fano factor is the statistical variance of electron-hole pairs created divided by the expected value of electron-hole pairs per incoming particle. The formula for calculating the Fano factor, which also can be found in [101], is illustrated here

$$F = \frac{\sigma^2}{E/\epsilon} \tag{3.4}$$

where σ is the statistical variance, F is the Fano factor, E is the energy of incoming particles, ϵ is the ionization energy, i.e., the energy needed to produce one electron-hole pair, and E/ϵ is the total number of produced electron-hole pairs. The ionization energy is approximately ϵ =3.62 eV at a room-temperature for the silicon detector. The detection efficiency of silicon detectors is nearly ideal when it comes to detecting alpha particles and other light ions, in the sense that all of the particles hitting the detector generate a pulse [101]. If one ignores the background sources, the resolution of the silicon detector is only limited by the Fano factor, the energy of the incoming particle, and the ionization energy. One can know the fractional energy resolution

$$R_{lim} = 2.35\frac{\sigma}{E/\epsilon} = 2.35\sqrt{\frac{F\epsilon}{E}} \tag{3.5}$$

The energy resolution is usually given as the full width at half maximum FWHM, as represented here

$$FWHM|_{lim} = 2.35\sqrt{F\ E\ \epsilon} \tag{3.6}$$

which corresponds to the width of the energy peak, in a Gaussian distribution, at half of its amplitude. Typically, for a silicon detector, the value of the Fano factor [102,103] is in the order of 0.1. For that reason, one can attain a high energy resolution of a few keVs for the most common alpha particle energies in the MeV range. However, this theoretical limit can not be accessible because of other contributing parameters like electronics and low-frequency noise, which indeed limits and degrades the energy resolution and is inevitable. In practice, the best resolution, which can be achieved with silicon detectors at room temperature, to detect alpha particles, could reach around ten keV [101].

3.4 Components of the SI detector

3.4.1 Test-bench and setup

Electrons being the lightest particles, are scattered very easily in any medium. Their scattering results in a partial energy deposition and significantly misinterprets the measured energy spectrum. The detectors were operated under a vacuum to minimize the interaction of electrons within the detection chamber. All the vacuum components, the pump, the valves, and the flanges have been chosen accordingly.

The test bench to characterize our annular silicon detectors comprises a vacuum

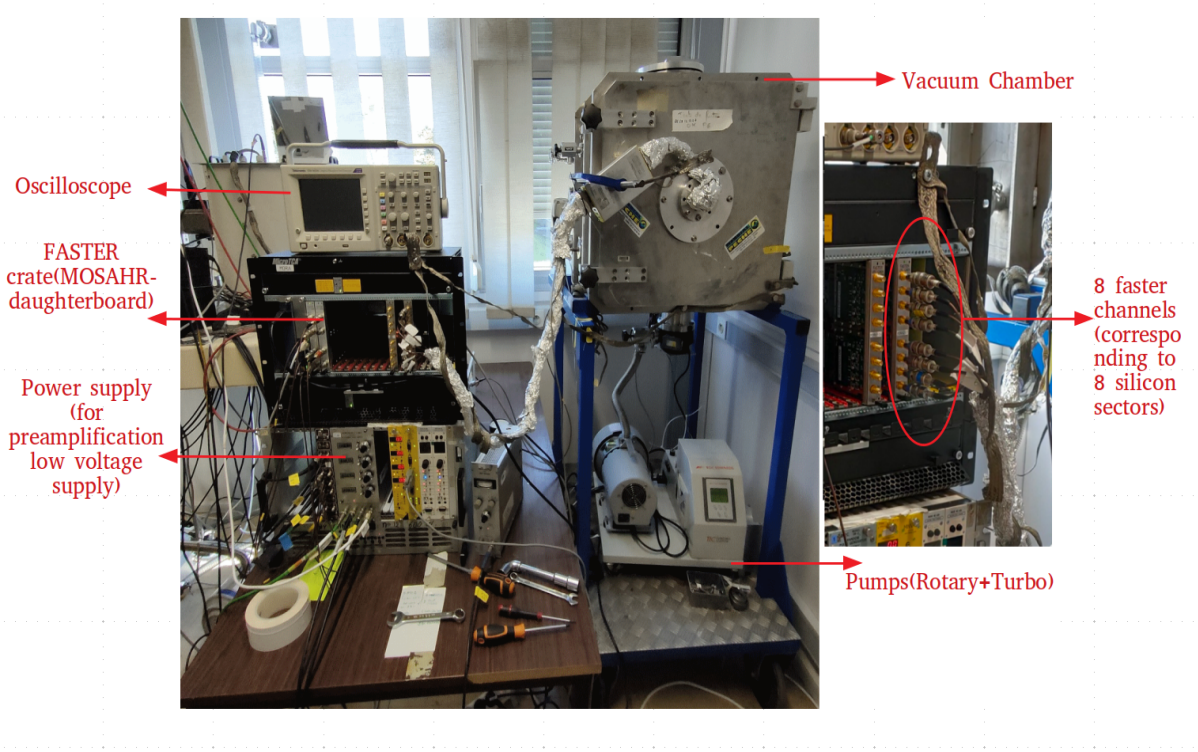

Figure 3.4 – Test bench dedicated for the characterization of silicon detectors, also showing the FASTER crate with installed MOSAHR motherboards utilizing ADC modules for this specific testing.

chamber. We used the vacuum gauge Edwards WRG-S-NW25 to read the pressure inside the chamber with the EDWARDS TIC pumping station. These pump features are integrated into the TIC turbo and instrument controller, which delivers complete control of the pump functionalities via a simple interface. The speed of the molecular turbo pump ranges from 47 to 400 $l.s^{-1}$. The gauge is connected to the pump via an Ethernet cable. The primary pump evacuates air from the chamber up to 10^{-2} mbar, and the turbo pump starts immediately. This system allowed us to reach up to 10^{-5} mbar at room temperature within 2-3 hours for our chamber. Special care was taken in the selection of the vacuum chamber arrangement to avoid significant damage to

the active surface of silicon as well as the cables going to preamplifiers, see Fig. 3.4.

3.4.2 Electronics and Preamplification

The high voltage supply used in this testing setup is an ISEG NHR module, a multi-channel high voltage power supply in 1/12 NIM standard cassette format. They provide up to 4 channels, each with an independent voltage, current control, and electronically reversible polarity. It can supply 4 mA up to voltages of 2 kV, 3 mA up to 4 kV, and 2 mA up to 6 kV. In our case, we operated the detectors at 80 V negative supply.

A preamplifier usually is the first stage of an acquisition system, as the signal amplitude from the detector output is low and typically requires amplification. Generally, the preamplifier should be placed as close as possible to the detector to reduce the capacitance loading onto the detector and capture electronic noise in the line. The preamplifier's two main functions are to adapt the high impedance of the detector to preserve the signal throughout the cables and maximize the signal-to-noise ratio.

A charge-sensitive homemade preamplifier card, manufactured at the GANIL facility (see Fig. 3.5) was utilized first in this work as a convenient alternative since this card possesses 16 outlets functionality which gives us full access to use this for our multi-channel (8-sectors) silicon detectors. In this process, we experienced multiple problems in the testing procedure at the beginning of the characterization. The reasons were the following:

- Initially, we had to use air blowers to cool down the preamplifiers, usually starting with very low voltages. We often observed the signal strength to be very low because of not attaining high gain with homemade preamplifier card.
- Some of the preamplifier chips were damaged over time, which initiated the problem of high leakage current up to 2 μA and the non-visibility of some of the sector's signals.
- We compromised a lot with the preamplifier gain using this card module as we mandated the gain higher up to 200 mV/MeV, and we could only reach up to the gain value of 50 mV/MeV.
- Several problems of excessive background/noise arose from the lousy insulation of cables used for preamplifier-detector connections.

However, there has been a change in the test setup since we observed the persistent noise issue. We witnessed in the beginning phase a periodic noise of 500 Hz appearing consistently, which ultimately required some major modifications in the test setup:

- We got rid of the extra grounding cables from the test bench to avoid looping issues, as well as the turbo controller, which was believed to be the primary source of the appeared noise.

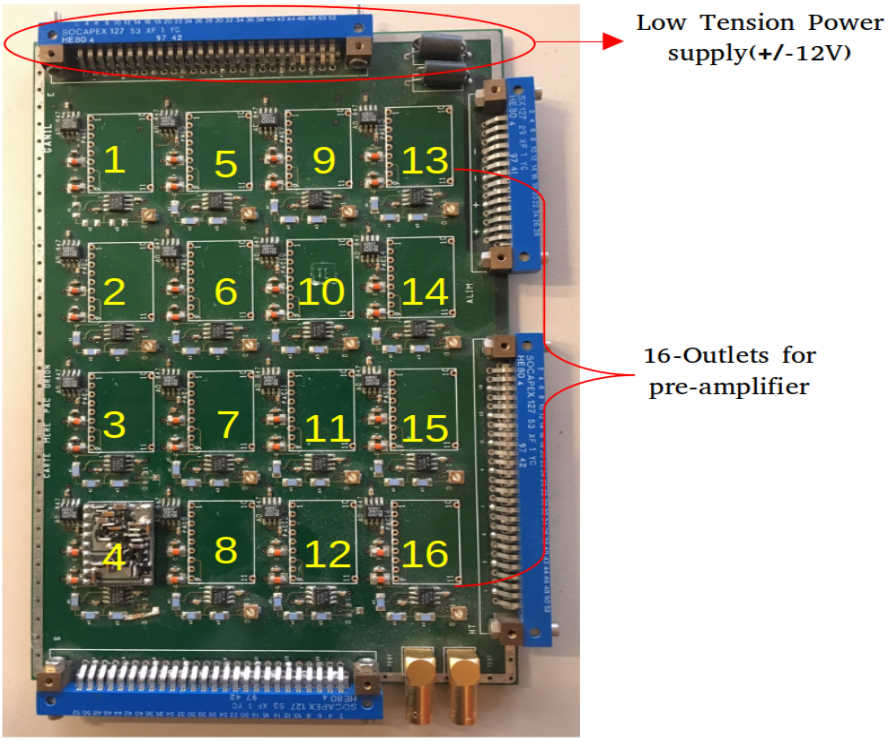

Figure 3.5 – Homemade PAC (Preamplifier card) with 16 outlet functionality dedicated for multichannel silicon detectors.

- To a specific point, we could eliminate the noise issue with a new controller and its placement settings.
- We even replaced the turbo pump with a new one.
- We attempted to put extra rubber rings for better vacuum on the testing vacuum chamber's top, front, and bottom flange.
- The ring holding the preamplifiers was very sensitive, and we could occasionally see the amplitude/ noise strength change.

Eventually, with many noise issues being tackled and after a long gymnastic period for selecting the best preamplification system for our detectors, we looked to use the commercial option, the one provided by *Mesytech* [104]. Finally, We used the Mesytech MPR-16-L preamplifiers, which provide a state-of-the-art multi-channel charge integrating preamplification, very well suited for silicon or gas detectors, see Fig. 3.6. This module provides a switch to amplify the output signal by a factor of 5 which further helps to give a large output signal even at low-charge depositions and thus offers excellent noise immunity. Standard types are available, which are 100 MeV, 500 MeV, and 2.5 GeV. Here mentioned are some of the useful features one should get while employing this technology preamplifiers:

- A compact module furnished with 16-channel functionality and the PCB is suitable for vacuum use

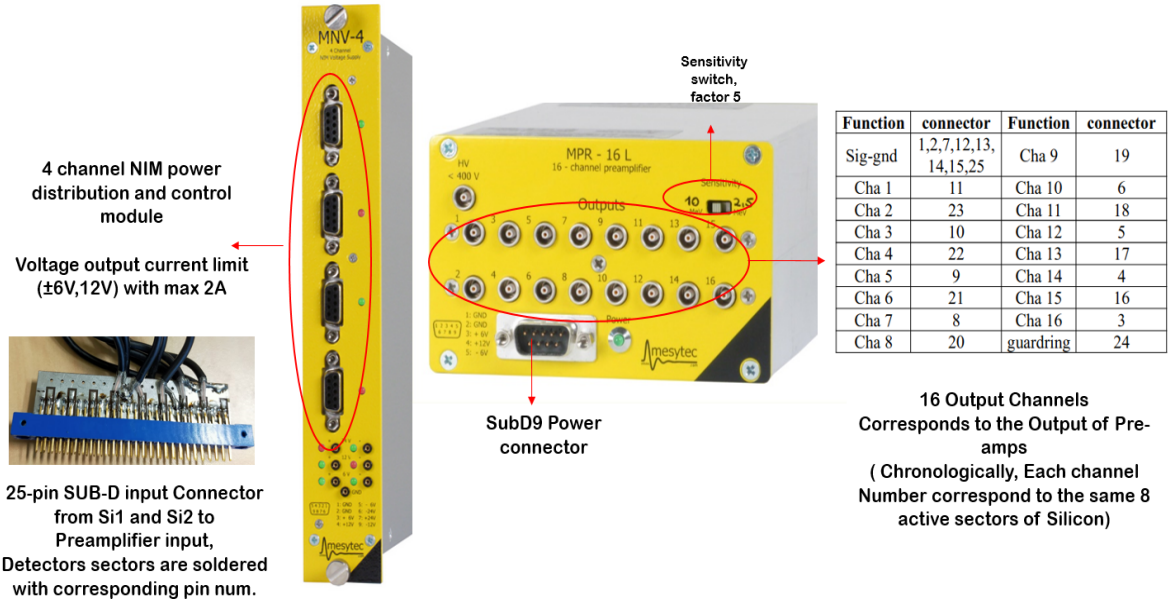

Function	connector	Function	connector
Sig-gnd	1,2,7,12,13, 14,15,25	Cha 9	19
Cha 1	11	Cha 10	6
Cha 2	23	Cha 11	18
Cha 3	10	Cha 12	5
Cha 4	22	Cha 13	17
Cha 5	9	Cha 14	4
Cha 6	21	Cha 15	16
Cha 7	8	Cha 16	3
Cha 8	20	guardring	24

Figure 3.6 – We have opted for the 16-channel preamplifiers with 4-channel low energy NIM power supply and subD9 power connectors suitable for 8-channel detectors used in this work. Lately, we have modified the preamplifier input connections to have more convenience.

- A very low power dissipation (4V type)
- Sensitivity switch, providing a factor of 5 difference
- Input protection with ESD (electrostatic discharge)
- Lemo output can drive terminated BNC lines
- Input outlet for the use of pulser
- Biasing voltage up to $\pm$ 400V.

3.4.3 Faster Acquisition (DAQ)

Moving further, we utilize the FASTER module for the silicon detectors called CRRC4-Spectro MnM (Measurement Numerical Module), which is initially a spectroscopy module and can handle charge preamplifiers with a time constant ranging from 8 μs to 600 μs. The dynamic input range depends on the daughter card installed in the module. In our case, we are taking advantage of the MOSAHR daughter card where the dynamic range can be either $\pm$1V, $\pm$2V, $\pm$5V, or $\pm$10V with accessibility to

4 input channels.

Some important tuning parameters to be taken care of while using the ADC module of the MOSAHR daughterboard are illustrated using Fig. 3.7. These are:

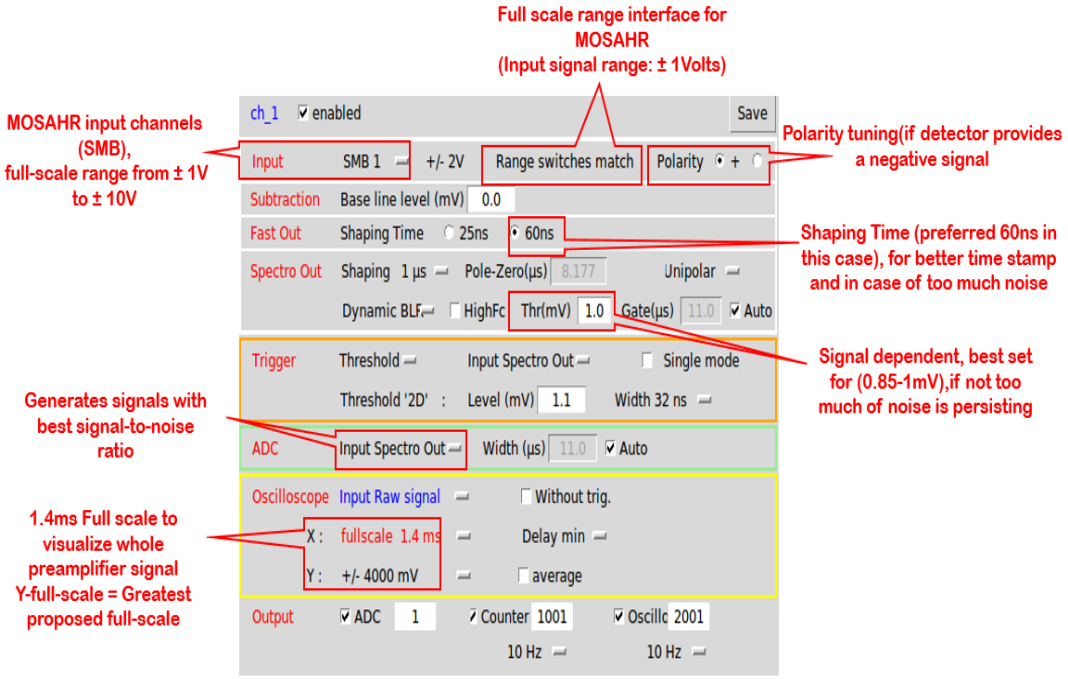

Figure 3.7 – FASTER pop-up window while utilizing the ADC module for MOSAHR daughterboard.

- The *Full-scale range* for the MOSAHR daughterboard we considered while configuring the FASTER is $\pm$1V, corresponding to the input impedance of 3 kΩ.
- *Polarity* was tuned for negative in our case as we obtained a negative signal from the detector as illustrated using Fig. 3.8.
- The shaping module for this daughterboard provides three functionalities one can choose based on the requirement. We have used *Spectro out* module, which filters the signal from the charge preamplifier and improves the signal, resulting in the best signal-to-noise ratio, provided the other parameters are correctly set.
- The threshold selection is signal dependent. It is set during the characterization between 0.85 mV and 1 mV if excessive noise wasn't persisting. The essential feature of this module is a *CR-RC4* filter, and it defines several related *shaping times*, representing the standard deviation of the resulting filtered signal. The

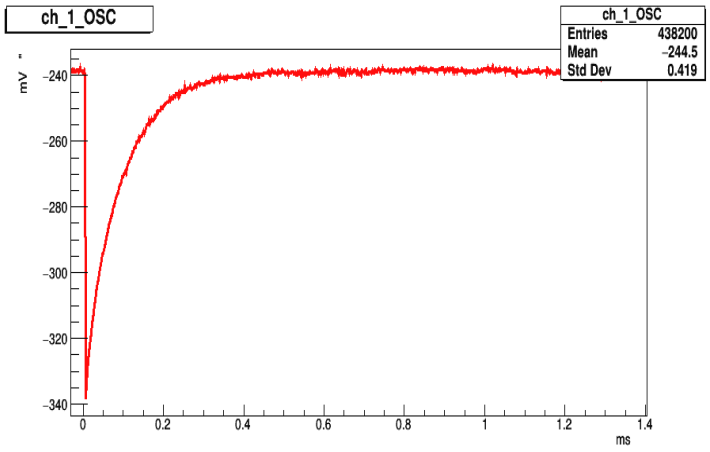

Figure 3.8 – Negative Silicon detector signal coming from sector 1 captured from the RHB visualization tool of the FASTER data acquisition system.

best shaping time depends on the detector and the charge preamplifier, which maximizes the signal-to-noise ratio and provides the best spectra resolution.

- As we discussed in the last section about the preamplification used, we tested our detectors with the shaping time of *1 μs*. However, we also tested the detector response with 500 ns, 2 μs, and 4 μs shaping time for a more reasonable comparison.

3.5 Detector Characterization and Methodology

Before discussing in detail the characterization of silicon detectors with different offline radioactive sources (3-α & ^{207}Bi), we will also briefly discuss the adapted methodology for energy calibration and determining the detection thresholds for each sector of the detectors.

3.5.1 Energy Calibration

When electrons or charged particles interact in the detector, the deposited energy is characterized by the electrical signal and recorded in the acquisition channel. To obtain the energy spectrum, the detectors must be calibrated. Generally, this is done by using well-known energy references and establishing a relationship between the number of channels and the energy. The calibration curve is obtained by a polynomial relationship, as given in (3.7)

$$E(\text{keV}) = E_0 + G_1\, C + G_2\, C^2 ... \tag{3.7}$$

where C is the channel number, E_0 is the energy at channel 0 and the set of G_i are the calibration coefficients. The objective of the energy calibration is to obtain a spectrum displayed in absolute energy so that it can be studied. The calibration of the detector

allows us to characterize it, know its resolution at a given energy, and judge whether or not the detector is suitable to be used in the final experimental apparatus. This is a common operation for silicon detectors. We first started the detector calibration with an alpha source, comprised of ^{241}Am, ^{239}Pu, and ^{244}Cm isotopes.
The calibration with alpha particles is intriguing because it takes place at relatively high energy, very far from the noise at low energy, so it is easier to follow the energy peaks for calibration. Hence, it is easy to identify the peaks and calibrate them rightly.

One can see the applied calibration with three alpha peaks and the obtained linear fit in Fig. 3.9. For the calibration of the Si detectors, we also used a radioactive source

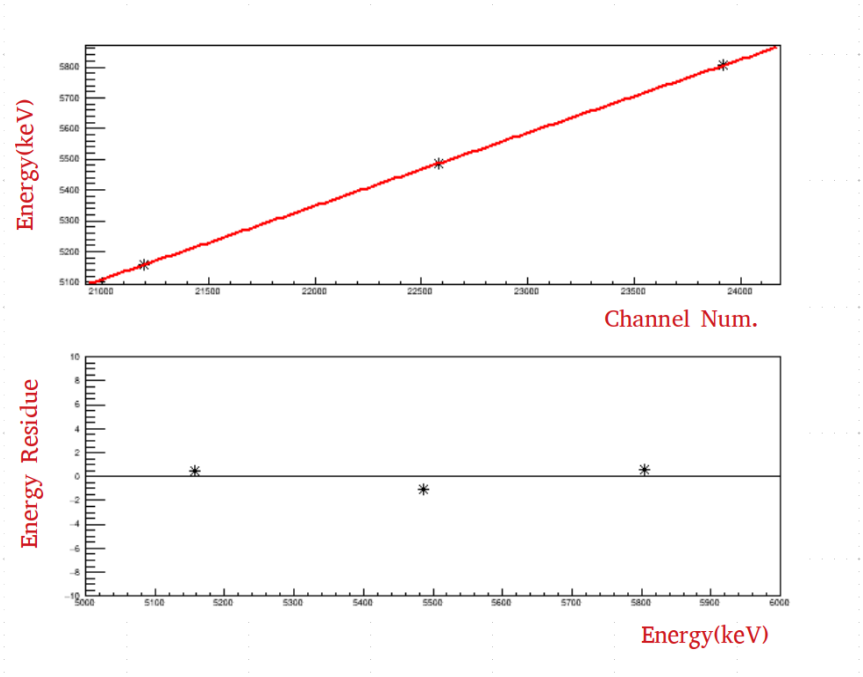

Figure 3.9 – (top) Preliminary energy calibration curve of alpha energies as a function of channel number, performed with 3-α radioactive source composed with ^{239}Pu, ^{241}Am, ^{244}Cm. (Bottom) The residual energy computed with the difference between real and measured energy after applying the calibration.

of ^{207}Bi. The conversion electron peaks emitted by the decay of ^{207}Bi allowed us to calibrate the detector.

3.5.2 Energy Resolution

The performance of a detector is characterized in particular by its energy resolution. The number of electron-hole pairs created during the interaction of an electron in the detector is not constant, and as the charges drift to the electrodes, they may recombine or produce new pairs. As a result, the peak induced by a mono-energetic electron beam does not correspond to a Dirac function in the energy spectrum. Still, it has a certain width, usually close to a Gaussian distribution. Besides, the noise of the electronic chain contributes to this peak width. The energy resolution, or Full Width

at Half Maximum (FWHM), is generally approximated by the following relationship

$$W_T^2 = W_P^2 + W_C^2 + W_E^2 \tag{3.8}$$

1. The first term, W_P^2, is the fluctuation of the number of charges created in the detector and is given by

$$W_P^2 = (2\sqrt{2\ln 2})^2 F\,\epsilon E \tag{3.9}$$

2. The term W_C^2 corresponds to the charge collection statistics and varies as the square of the incident electron's energy. The effects of an incomplete charge collection are linearly dependent on energy. As the energy increases, the number of charge carriers in the detector increases. Thus, the charge collection may be incomplete. This effect also increases with the dimensions of the detector crystal.

3. The electronic noise W_E^2 is highly dependent on the detector capacitance and the electronic components of the acquisition system. Its contribution to the FWHM is energy-independent.

3.5.3 Tests with 3-alpha source

To check the energy resolution of the system, an alpha source was temporarily placed inside the testing chamber (under vacuum), mechanically supported by the collimator wheel. The available alpha source used to test the setup consisted of a mixed-radioactive source containing three isotopes: plutonium (^{239}Pu), americium (^{241}Am), and curium (^{244}Cm), producing three prominent alpha peaks, respectively at energies of 5.156 MeV with an intensity of 70.77 %, 5.486 MeV with 84.8 % and 5.805 MeV with an intensity of 76.9 %, as we can see in Table 3.10. The acquired

	Energy(keV)	Intensities(%)
239Pu	5105.5	11.94
	5144.3	17.11
	5156.6	70.77
241Am	5388.0	1.66
	5442.8	13.1
	5485.6	84.8
244Pm	5762.6	23.1
	5805.8	76.9

Figure 3.10 – Tabulated three alpha energies and their intensities used for silicon detector characterization.

spectrum for reference with one silicon sector is illustrated in Fig. 3.11. Also, we can see with a closer look that some peaks are not fully resolved from each other. To show the detector response's consistency, we plotted each sector of the detector after applying the energy calibration as shown in Fig. 3.12.

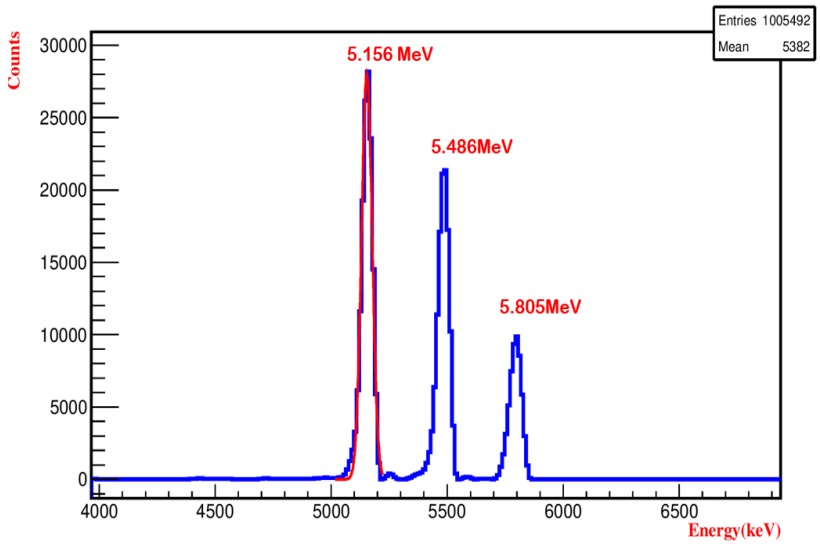

Figure 3.11 – Calibrated spectra obtained with 3-alpha source, the individual peaks coming from Am, Pu, and Cm were used for the fitting.

The resolution obtained for the three prominent peaks at 5.157, 5.486, and 5.805 MeV is 34, 32, and 30 keV FWHM, respectively. The larger spread in the alpha peaks and the low-intensity signal is mainly because we performed these tests utilizing the homemade PAC and the higher electronic noise contribution measured in the system. In addition, the quality of the alpha source and its relative position to the detector may also influence the final resolution, as related to the energy losses of the alpha particles in the source itself and angular effects in the detector entrance window.

3.5.4 Tests with ^{207}Bi

The second measurement was performed using an electron source. The ^{207}Bi was used as an electron-emitting source in this measurement to test the detector response to beta particles. Note that this configuration has an aluminum cover protection shield before the detectors. The experiment uses the Al cover to prevent reflections from the laser system to trigger the Si detectors. Its effect on the path of electrons needed to be evaluated. Therefore the cover was included during the tests with such a radioactive source. The ^{207}Bi nuclei decay to excited states of ^{207}Pb primarily via electron capture and a small β^+ branch, emitting beta particles of E_{max}= 806 keV, $E_{average}$= 383 keV, and the excited states of ^{207}Pb decay via internal conversion, emitting conversion electrons of $\sim$1 MeV. In addition, the ^{207}Bi decay was accompanied by the emission of gamma rays of 570 keV (98 %), 1064 keV (74.6 %), and 1770 keV (6.87 %).

One can use a database (ESTAR DATABASE [105]) that gathers the stopping powers to determine the value of the energy loss in aluminum. Considering an energy of

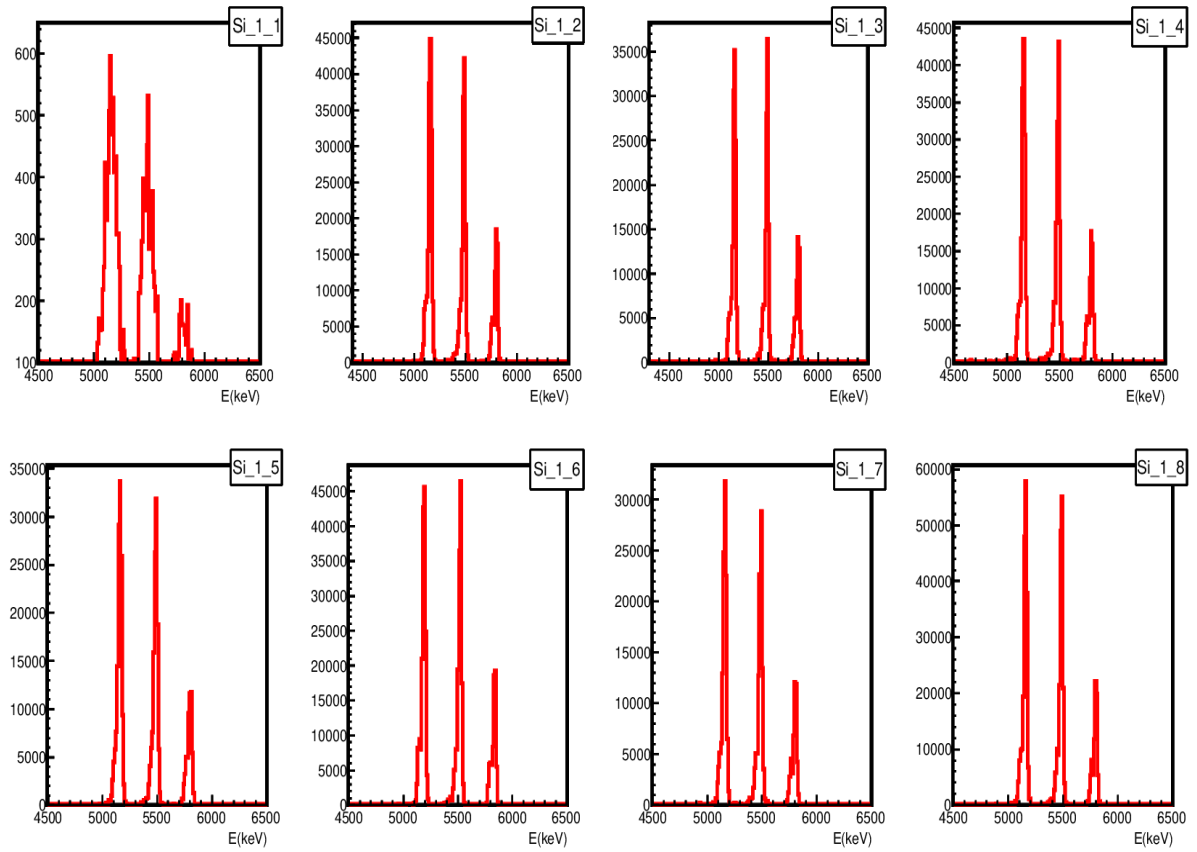

Figure 3.12 – Calibration spectrum showing all the 8 silicon sectors with 3-α reference source with mixed radionuclides (^{239}Pu, ^{241}Am, ^{244}Cm). The calibration is done without the aluminum protection cover.

about 1 MeV (which corresponds to the closest peak of 975 keV), one can recuperate an attenuation of 1.486 MeV.cm^2.g^{-1}. Knowing the density of 2.7 g cm^{-3}, the stopping power of aluminum at 1MeV, and the thickness of the plate, it is possible to determine the attenuation, which in our case is computed as 40 keV. This value corresponds to the simulation done with silicon detectors with the plate for protection. The peaks fitted in the energy range 400 keV - 1100 keV are shown in Fig. 3.13 and 3.14.

The fitted peaks are used for energy calibration. The detector response was found to be linear in our case, see Fig. 3.15. We obtained the disagreement parameter(1-R^2) equivalent to 0.1% The second peak seems to originate from coincidence events in which conversion electrons at 481.6 keV and Auger electrons deposit their energy, see Fig. 3.16. The same structure is observed for the 553 keV and 975 keV peaks. The energy resolutions and thresholds obtained in this measurement are tabulated using Table 3.1.

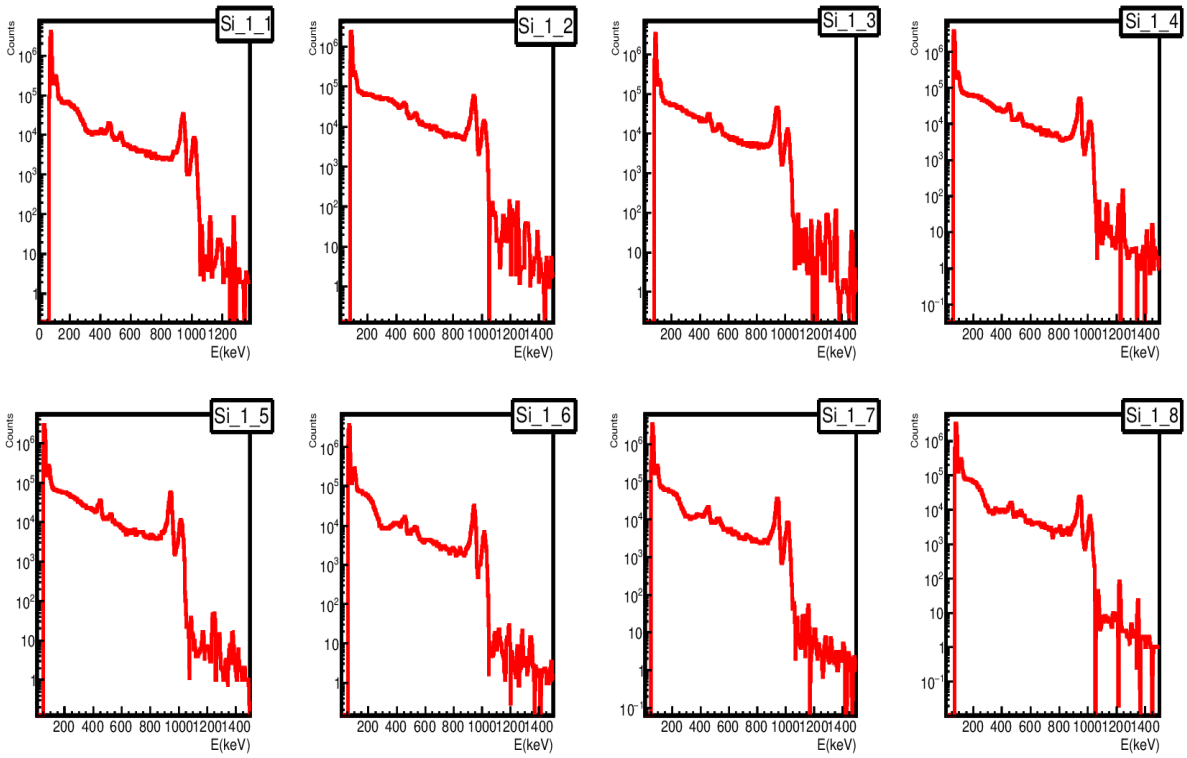

Figure 3.13 – Preliminary energy calibrated spectra obtained with the ^{207}Bi source on Si-1 silicon detector (close to the ion beam injection line). The calibration takes into account the attenuation in the aluminium layer.

Channel No.	Sector No.	Si1		Si2	
		Threshold(keV)	FWHM	Threshold(keV)	FWHM
Ch-1	**sec-8**	75	**26.0**	50	**29.5**
Ch-2	**sec-1**	80	**33.3**	80	**33.0**
Ch-3	**sec-2**	90	**33.0**	70	**35.0**
Ch-4	**sec-3**	70	**27.5**	65	**19.32**
Ch-5	**sec-4**	65	**26.2**	80	**28.2**
Ch-6	**sec-5**	70	**24.2**	90	**29.4**
Ch-7	**sec-6**	70	**25.3**	85	**26.5**
Ch-8	**sec-7**	80	**29.0**	65	**28.2**

Table 3.1 – Energy resolutions and thresholds of Si1 (det-1) mounted in the actual configuration close to the beam injection line and Si2 (det-2) installed close to the laser entrance setup of MORA, obtained with ^{207}Bi electron source. The calibration considers the attenuation of 40 keV due to the aluminum protection cover.

3.6 Monte Carlo Simulations

We conducted simulations for the annular silicon detectors to reproduce the experimental results obtained while testing them in the presence of different radioactive sources (alphas, electrons). The specific software for this task is the so-called PENELOPE code.

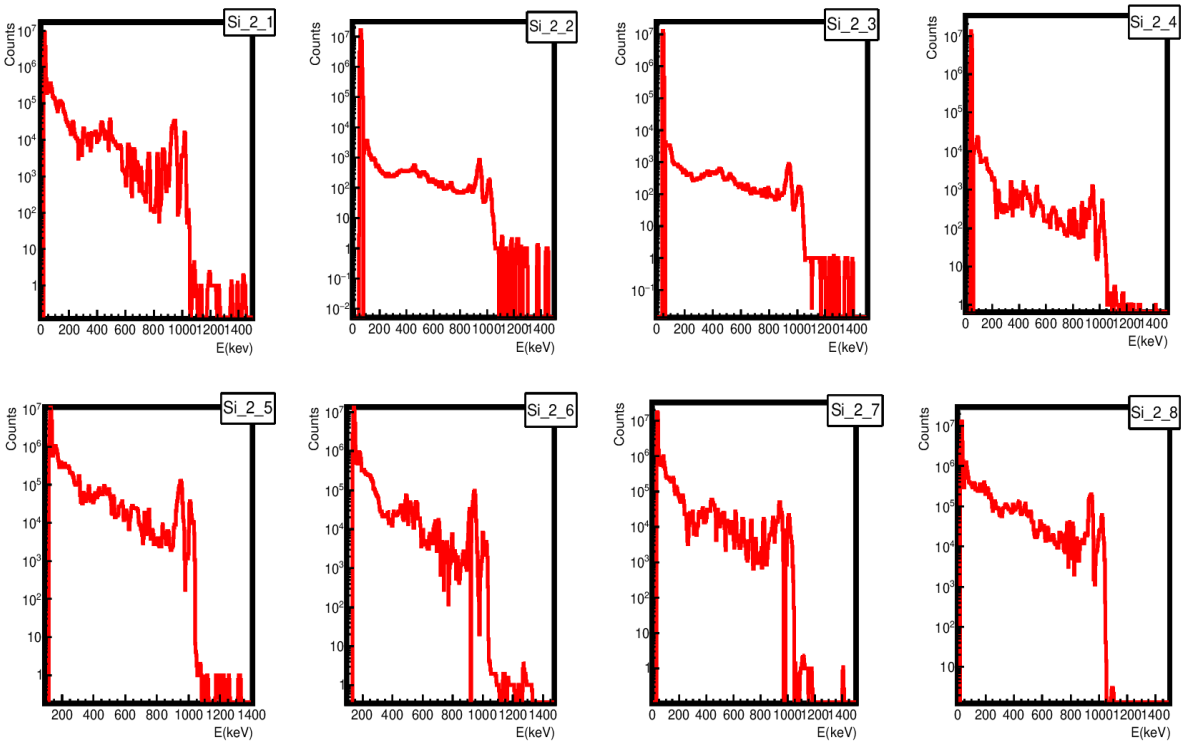

Figure 3.14 – Preliminary energy calibrated spectra obtained with the ^{207}Bi source on Si-2 silicon detector (close to the laser entrance setup). The calibration takes into account the attenuation in the aluminium layer.

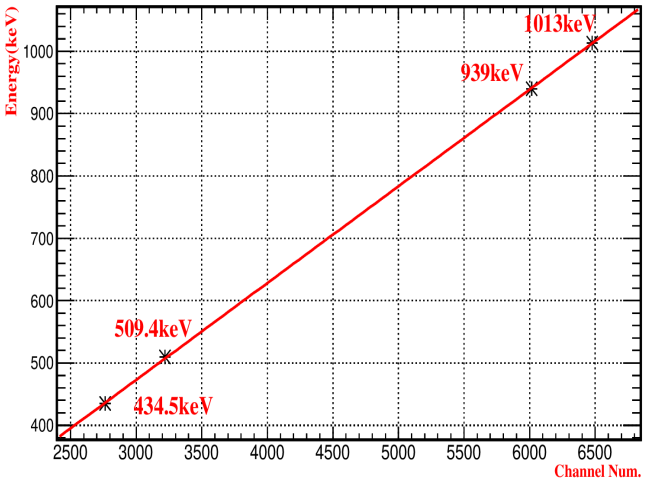

Figure 3.15 – Energy calibration curve of electron energy as a function of channel number, performed with the conversion electron lines from ^{207}Bi decay

PENELOPE is a Monte Carlo code initially designed to handle the transport of electrons and positrons in the matter for an energy range from a few hundred eV to 1 GeV [106]. The term stands for *PENetration and Energy LOss of Positrons and Electrons*. It was developed by the University of Barcelona and distributed by the OECD's Nuclear Energy Agency (NEA). As the PENELOPE code utilizes a mixture of different

		Energy keV			Electrons per 100 disint.
e_{AL}	(Pb)	5,2	-	15,7	54,8 (7)
e_{AK}	(Pb)				2,9 (4)
	KLL	56,028	-	61,669	}
	KLX	68,181	-	74,969	}
	KXY	80,3	-	88,0	}
$ec_{1,0\ T}$	(Pb)	481,694	-	569,680	2,112 (29)
$ec_{1,0\ K}$	(Pb)	481,694		(2)	1,548 (22)
$ec_{1,0\ L}$	(Pb)	553,838	-	556,664	0,429 (7)
$ec_{1,0\ M}$	(Pb)	565,848	-	567,215	0,1057 (16)
$ec_{3,1\ T}$	(Pb)	975,655	-	1063,640	9,53 (18)
$ec_{3,1\ K}$	(Pb)	975,655		(3)	7,11 (17)
$ec_{3,1\ L}$	(Pb)	1047,798	-	1050,624	1,84 (5)
$ec_{3,1\ M}$	(Pb)	1059,808	-	1061,175	0,441 (25)
$ec_{3,1\ N}$	(Pb)	1062,765	-	1063,523	0,1193 (30)
$\beta^+_{0,1}$	max:	805,8		(21)	0,012 (2)
$\beta^+_{0,1}$	avg:	383,4		(9)	

Figure 3.16 – The conversion electron energies from the decay of ^{207}Bi used for the energy calibration.The source of expected energies is decay data evaluations [5, 6].

methods, it provides tangible results and is considered the reference code for transporting electrons and positrons in the matter. This software is programmed in the FORTRAN77 language. This code does not allow object-oriented programming and is divided into several subroutines allocated to geometry, physics modelling, etc. Typically, the geometry of PENELOPE can authorize very complex constructions.

To proceed with the simulations, the two main files required are geometry with an extension .geo and an input file with an extension .in.

The geometry file contains the geometry of the implemented detectors and the setup. We use another dedicated program for the list of materials already recorded in PENELOPE, including all the physical data on each material and physical properties like mean excitation energy, density, interaction cross-sections, atomic relaxation data, etc. The input file acts as an essential file where we include all the parameters like the name of the geometry file, spatial coordinates, volumes, detector information as an active body with energy range and several bins, and type of particles (electron, photon, or positron), initial energy or a spectrum with energy and total probability for a mono-energetic source, output files names, the material used and the corresponding parameters (absorption energies, cutoff parameters, etc.) and the run-time for the simulation [106].

The generated output file, after the simulation, gives us the energy deposited in the detectors and its corresponding probability density in 1/(eV*particle). The simulation was first performed to compare the effect of aluminium protection cover in

the path of electrons, see Fig. 3.17 and then further convoluted with the experimental energy resolution of the detection system, see Fig. 3.18. We normalized the spec-

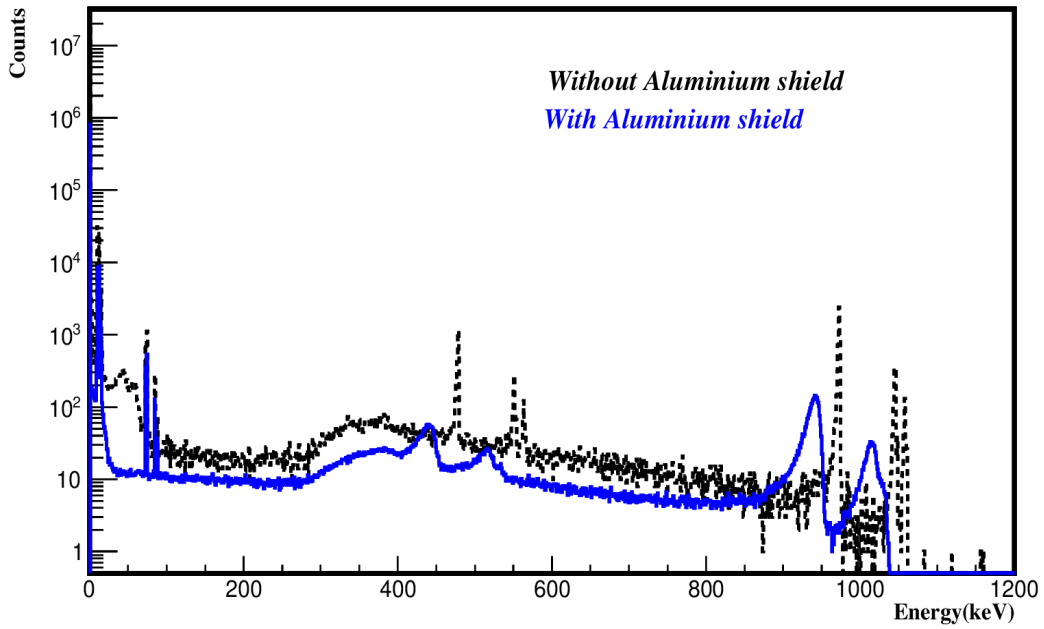

Figure 3.17 – Comparison of detector simulations with ^{207}Bi source. (Blue) With an aluminum cover of thickness 100 μm on the active surface. (Black) Without an aluminum cover, attenuation of 40 keV is observed in this case.

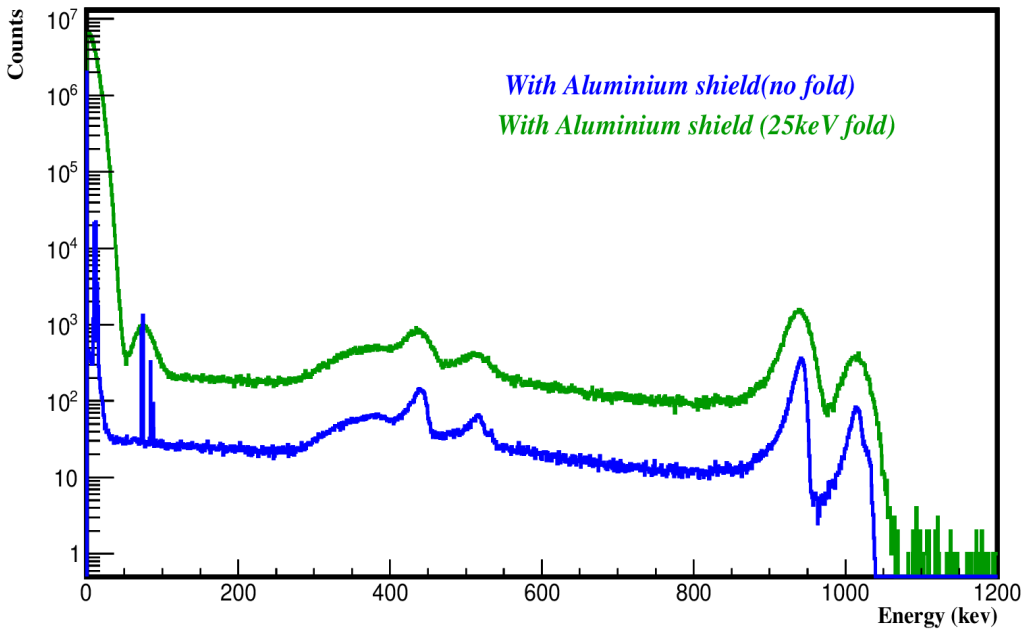

Figure 3.18 – Detector simulations with ^{207}Bi source in the presence of aluminium protection cover. (Blue) no fold. (Green) with 25 keV FWHM folding including the attenuation from aluminium cover.

trum of ^{207}Bi and compared it using 10^6 events in the simulation to verify the observed structure. We obtained a good agreement between the experimental and the simulated spectra, as illustrated using Fig. 3.19, which, in our case, validates the char-

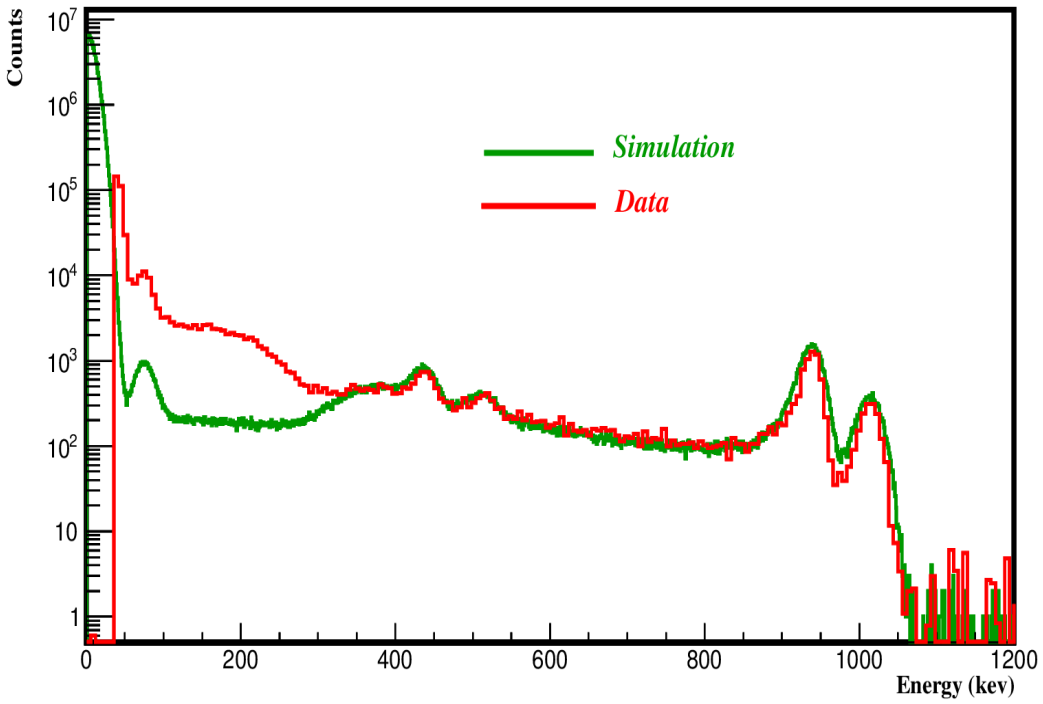

Figure 3.19 – Comparison of simulation (Green) with 25 keV FWHM fold and including the attenuation from aluminum cover and measurement (red) for ^{207}Bi decay.

acterization of the detection system. The observed differences at low energy in this comparison can arise from an external electronic noise at low energy and also due to the significant backscattering in the vacuum chamber.

3.7 Summary and Conclusion

With the characterization of silicon detectors, we managed to choose the best electronics and preamplifiers for our system. We successfully tested our detectors, although we dedicated a significant amount of time to mitigating the noise issues during the characterization process. We introduced a lot of modifications in the setup and electronics, which also included some necessary changes in the design of the connector connecting the preamplifiers and each detector sector. We opted for a more noise-suppressing environment by installing the ground cables around the connectors and more sensitive zones, keeping the preamplifier box in the absolute vicinity of the detectors, etc. We tested each of the detectors individually in the presence of alphas and electrons with and without the Al cover, covering the active surface of the detector. We observed an attenuation of $\sim$40 keV in the latter case. The detectors were tested successfully and simulated with the PENELOPE code in both cases. We achieved a detector resolution of 25-30 keV in the presence of electrons and 30-34 keV

in the presence of alphas, though we compromised with detector resolution in the latter preliminary testing because of not having the best option for preamplification.

This work is now being continued during the first experiments at Jyväskylä, as we are calibrating the silicon detectors again in the *MORA* chamber using an offline radioactive finger possessing two sources, mainly ^{241}Am for alphas and ^{90}Sr as an electron source. In addition, the idea of designing a new radioactive finger possessing ^{207}Bi source has been discussed within the group to ease the future calibration measurement in the case of Silicon detectors.

Progresses with MORA at IGISOL

4.1 Overview of the IGISOL-4 Facility

The *IGISOL*-4 accelerator facility of Jyväskylä - Finland [107] produces low-energy radioactive-ion beams specifically for performing nuclear spectroscopy by utilizing an ion-guide-based ISOL-type mass separator [108] The ion-guide technique functions on the survival of recoil ions in noble gas through a nuclear reaction in a thin target. Therefore, this mechanism can be applied to all elements, especially refractory ones. This technique is not limited to fission, as neutron-deficient beams can be produced through fusion evaporation and transfer reactions with light and heavy ions. Recently, many innovative techniques have been developed in the facility of *IGISOL* to improve the efficiency of heavy-ion fusion evaporation products. Although the ion guide source is universal, there are several other methods, like hot cavity laser ion sources, which can provide better efficiency and can be proved essential in the production of very exotic isotopes of some elements, for example, silver.

At the IGISOL facility, the radioactive beams are extracted from the ion guide source into a radio-frequency sextupole ion guide (SPIG) for low-energy transport into high-vacuum-condition regions. The ions are hereafter accelerated to 30 keV, mass separated using a self-focusing 55° dipole magnet, and then further delivered to an electrostatic beam switchyard for identification and experiments. Concerning *MORA*, the *IGISOL*–4 facility, is currently the only laboratory around the world that can provide mass-separated ^{23}Mg beams with the newly commissioned Multi-Reflection Time-of-Flight Mass Spectrometer (MR-ToF-MS). Prior to the MR-ToF-MS, the RFQ cooler buncher cools the ions and converts the continuous radioactive ion beam into narrow ion bunches of ^{23}Mg for efficient trapping. *IGISOL*-4 is also equipped with a suitable laser setup for in-trap orientation, which proves to be essential in our case. See Fig. 4.1.

4.2 Beam manipulation

As the beam is driven to the MORA beam line with around 30 keV of kinetic energy, which is way more energetic for being correctly trapped, a correct manipulation of the beam is needed, which has been taken care of in the injection line of MORA.

We initiated testing the line of *MORA* for the first time at *IGISOL* using three stable sources: a surface ionization source using a sodium pellet, a laser ablation source, and a spark source to perfect the commissioning. Already performed SIMION simulations for the injection line of *MORA* were also utilized in this process. Ultimately, we managed to get a good response during the tests performed with the spark source using Na, which proved to be the best among the three tests. We started by applying and

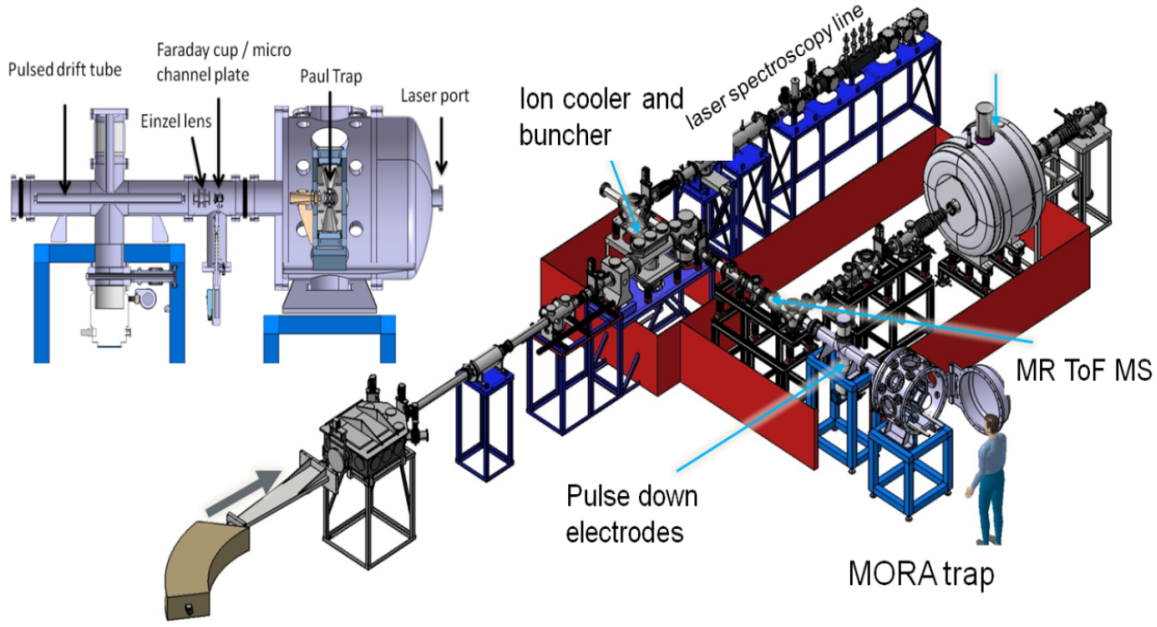

Figure 4.1 – Location of the MORA setup at JYFL in the IGISOL-4 experimental hall. (left) we see the injection line with Pulsed drift tubes (PDTs), Einzel lens, and other beam diagnostics used to inject the radioactive ions into the trap. (right) we see the IGISOL line starting from the mass separator, RFQ cooler buncher followed by the line of MORA

adjusting the voltages/timings configuration for the injection line and trapping parameters found during the first-ever commissioning performed at LPC Caen, where ions were successfully trapped.

4.2.1 The injection line of MORA

The beamline of *MORA* has been designed and fabricated by the technical expert's team from LPC Caen, holding a precision of 10 μm. The injection line of *MORA* incorporates two Pulsed Drift Tubes, namely PDT1 and PDT2 having a length of 40 cm and 18 cm, respectively, see Fig. 4.2 and 4.3. These two PDTs are made of three electrodes, where the two ground electrodes frame the main one. Apart from that, two sets of steerers, comprising four electrodes, are placed just after the PDT1 and before the PDT2. We utilize an Einzel lens, also placed between the two sets of steerers, to ensure the beam is correctly focused.

We also can incorporate some possible diagnostics in the injection line placed before the second steerer by using a compressed air system. Three sets of attenuators are being used in the configuration with an attenuation factor of about 90% enabling control of the ion flux to MCPs. It is optionally equipped with a phosphorus screen attached to it. MCPs are naturally used because of their excellent properties in detecting ions of the given range (see Chapter 2). Placed behind the MCP, the phosphorous

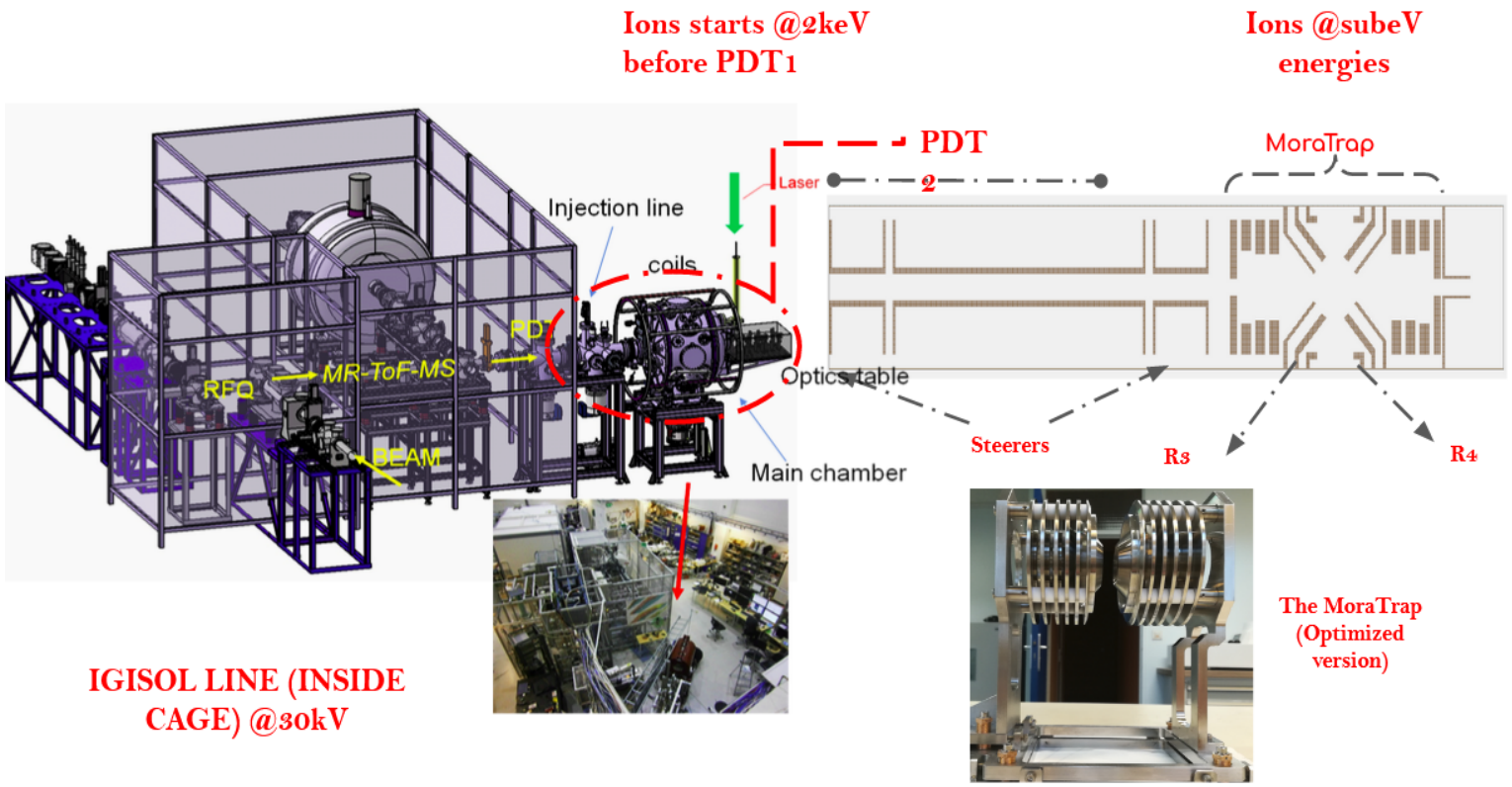

Figure 4.2 – Beam manipulation in the IGISOL line and the injection line of MORA using two Pulsed Drift Tubes (PDTs) for slowing down the energy of ion bunches to a few eV range for efficient trapping and laser polarization.

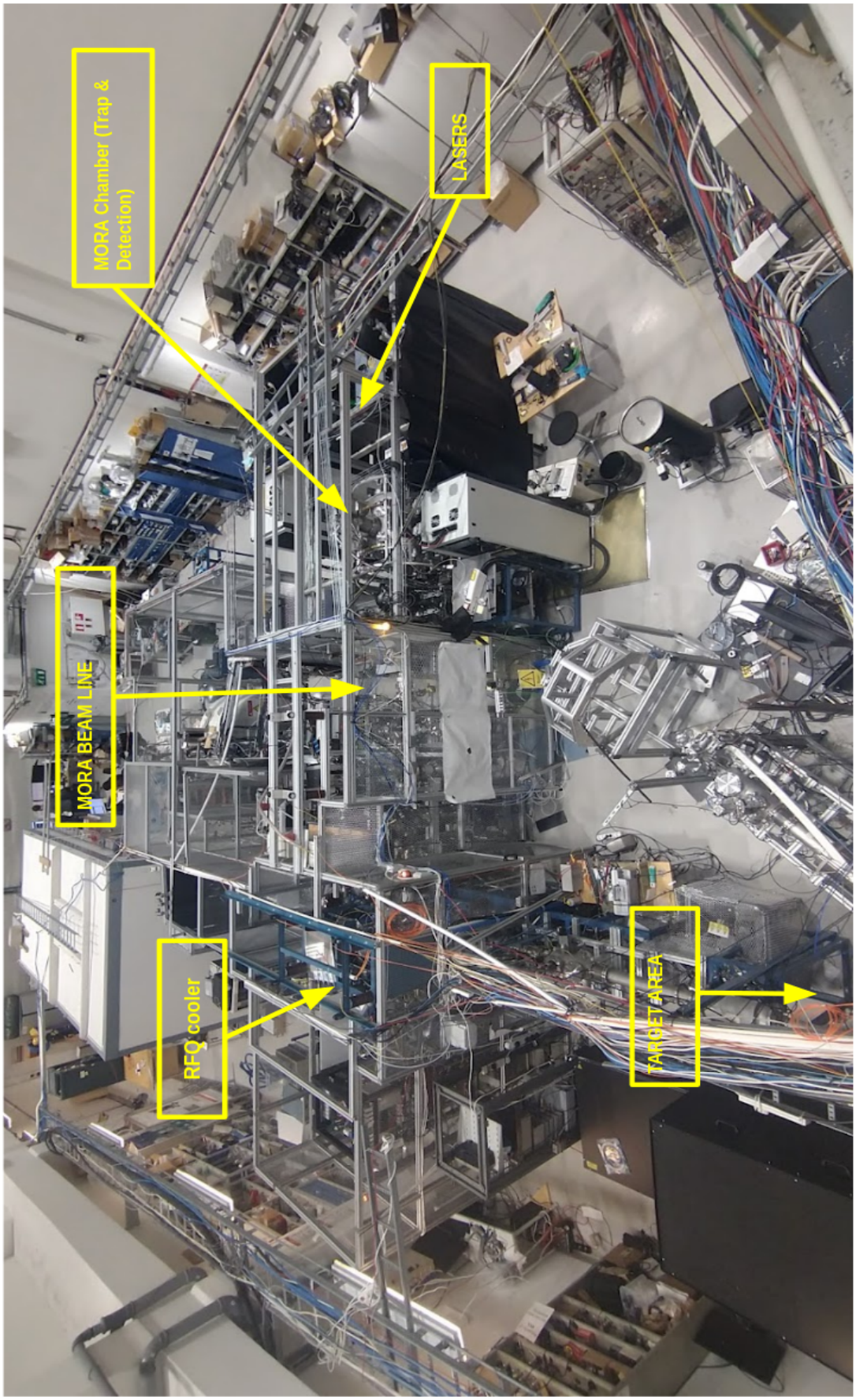

Figure 4.3 – Real Time picture of IGISOL facility, showing the RFQ cooler buncher, the line of MORA, detection chamber, and the laser table. This picture was taken after the first commissioning of the line and detection setup in Jan 2022.

screen can be switched on by applying an accelerating voltage to the secondary electrons in order to witness the ion bunch's position with the help of an installed CCD camera just above the screen. The camera is shrouded with black fabric in order to eradicate the external light. Rather than just affirming if any ions are coming, it also helps us monitor the beam shape, which is a very convenient option, especially when one measures an electric current on the first attenuator of the line of *MORA*, but no real confirmation of ions on the first MCP detector. The camera can also be used with a second diagnostic: a mirror can be inserted in the line, which takes the same spot as the MCP detector. Since it is coupled with the CCD camera, it can also monitor the laser alignment with the radioactive ion beam cloud in the trap's center.

The function of the PDTs is to slow down the ions. To implement this phenomenon, we use the following procedure, which involves

- Applying a positive voltage, using an independent power supply separated from the one of PDT1, which is plugged directly into the high-voltage beam line to fix it so as not to disturb the energy of the ion bunches delivered by the RFQ cooler buncher.
- As a result, the ions will enter inside the PDT1 the same way as they would continue their path through the line of *IGISOL* at about 2 keV.
- Once the ions are inside the PDT1, and as soon as they reach the middle point of the tube, we apply a negative value of the potential.
- Eventually, when the ions exit PDT1, they will see their kinetic energy reduced by the applied negative value of the potential.
- Switching down to a negative value has two objectives: Reduce the bunch's energy and aid the beam's focusing. Therefore, as the ions exit the PDT1, they are slowed to the kinetic energy of 1500 eV. The negative bias plays as a lens in addition to reducing the energy of the bunches.
- We use the MCP detector to perform the first diagnostic and monitor the number of ions. Thanks to the FASTER DAQ, we can observe the charge collection and TOF of ions coming onto this dedicated MCP, now addressed as MCP1 in the text.
- The PDT2 operates on the same principle where the ions are further slowed down to reach less than 100 eV energy. The ions are then stopped by pulsing one electrode of the MORAtrap to be efficiently captured.
- The vital point to be noted here is that we are constrained in terms of the time dispersion of the beam. The acceptance coming from PDT1 is defined by the time spent in the PDT1 by a beam of mass equivalent to 23 and 2000 eV of kinetic energy. It corresponds to 3.1 μs. To be accommodated and then further trapped, the ion bunches are supposed to be narrower than this above-mentioned acceptance value.

SIMION simulations of the MORA injection beam line were done to probe the correct trapping electrode voltages but, most significantly, to find the correct timings for switching the pulse drift tubes. These timings exist to slow down the ions efficiently and then eventually for trapping. These timings were calculated by considering the ions' mean Time Of Flight (TOF) in the middle of the PDTs. However, it is difficult to predict the beam behaviour through SIMION simulations as evident discrepancies come from unknown parameters of beam shape (emittance) or precise energy from the buncher. These simulations are being refined by LPC Caen's team to perform simulations of the trapped ion cloud phase space.

4.2.2 The laser Preparation

The laser polarization of the trapped ion cloud is achieved by shooting the laser light, in our case, the Ti:Sa laser, which passes through polarization optics (1 half-wave plate, one cube, and 1 quarter-wave plate) to reach 280 nm of wavelength (UV light) of circularly polarized light, which will probe the hyperfine structure of the radioactive ions cloud of ^{23}Mg. Additional manipulation of the beam optics installed on the laser table consisted in inserting or removing an additional half-wave plate to revert the polarisation of the laser beam. Before the first test run, a stable 90 mW laser beam with 280 nm and circularly polarized could be prepared and sent to the *MORA* chamber. See Fig. 4.4. As soon as the laser beam was aligned, we checked the detection system and observed no additional background on the detectors.

4.2.3 Production reaction

Two competitive reactions were considered initially for the first experimental campaign of *MORA* in *IGISOL*-4: ^{nat}Mg(p,d)^{23}Mg, with 30 MeV primary proton beam, and ^{23}Na(p,n)^{23}Mg with 10 MeV primary proton beam. Those were tested in 2018, i.e., before the *MORA* setup was built. For both the reactions, about 4.10^4 pps of ^{23}Mg could be produced with $\sim$ 1 μA of p, while for safe operation, the primary proton beam would be effectively limited to 10 μA.

With a ^{23}Na target, the second reaction resulted in a level of contamination from ^{23}Na at least one order of magnitude higher than for the first one: a few 10^8 pps compared to 10^7 pps, respectively. The stable Mg isotope target was eventually considered for the first experimental campaign we conveyed. As it will become clear, larger contamination levels than expected were obtained.

4.2.4 Comments about beam purity

From the beginning, it was anticipated that even by choosing the appropriate target, the contamination level can be challenging to handle in the *IGISOL* RFQ beam cooler, which is intended to prepare the ^{23}Mg bunches before their injection into the line of *MORA*. The mini-buncher of *IGISOL* has been shown to possess a standard capacity of $5{\cdot}10^5$ ions/bunch. In these conditions, the ^{23}Mg injected in the trap was assumed to be limited to about 10^3 ions/bunch. We intended to reduce the contamination as much as possible by using a new reliable RF sextupole ion guide to extract

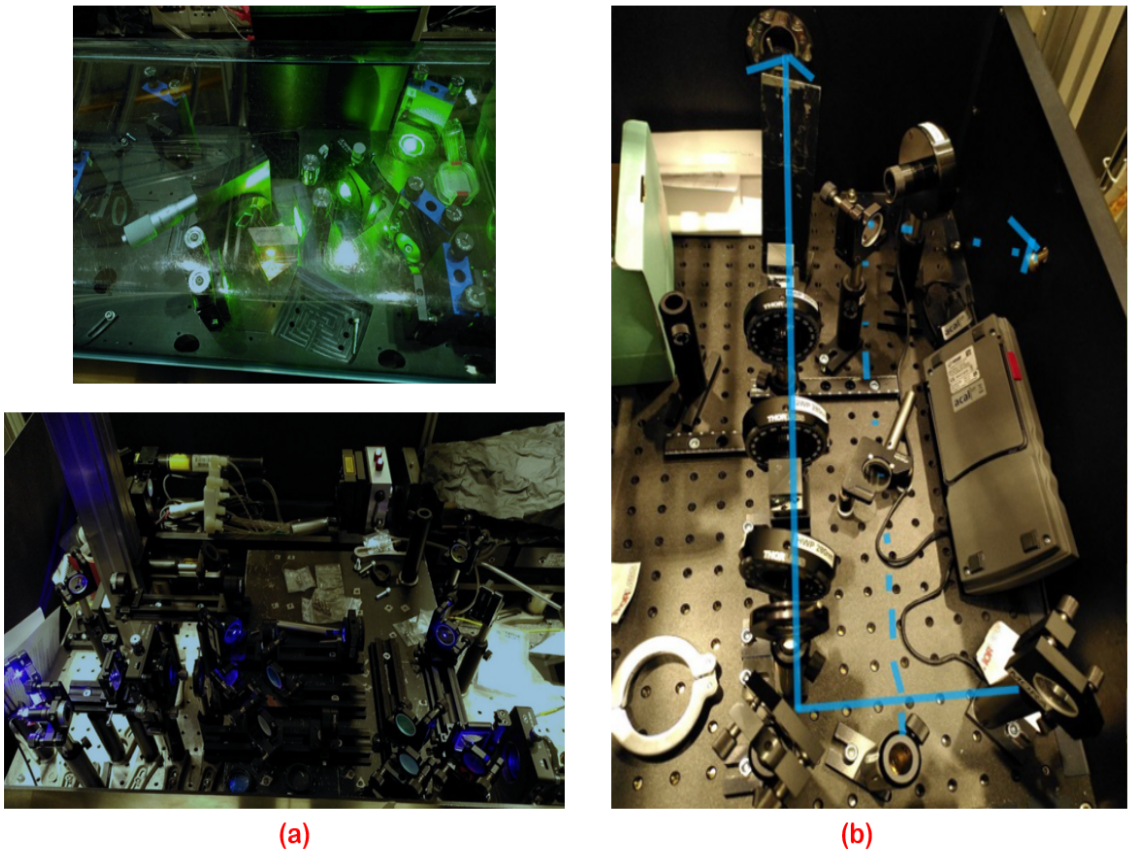

Figure 4.4 – (a) A stable 90 mW laser beam is 280 nm and circularly polarized, prepared to be sent to the MORA chamber, (b) suitable beam optics installed just after the laser table, switching the polarization cube by 90° directly from the optics table reverts the polarisation of the laser beam.

the beams from *IGISOL*, aiming eventually to trap 2.10^4 $^{23}Mg^+$ ions per cycle. An optimized version of the RF amplifier circuit was also used to achieve the highest space-charge capacity in the mini-buncher. The MR-ToF-MS facility necessitating bunched beams from the mini-buncher can separate the Mg beam from Na to inject a pure beam into *MORA*. But this separation happens too late in the beam manipulation to relax the main bottleneck limiting the number of Mg trapped ions injected in *MORA*: the space charge limitation of the mini-buncher combined with a high contamination rate.

4.3 Progresses in the beam time

Here we would like to discuss the progress made during the first two allocated beam times at *IGISOL*, followed by the latest run, which resulted in the first data-taking with the functional setup of *MORA*.

The first two test runs were mainly committed to optimizing the parameters in terms of ion bunching, transmission from the *IGISOL* line to the injection line of *MORA*, and further transmission of ion bunches through the line of *MORA* until the center of the trap, also in the meantime, considerable significant modifications/progress were made with some of the detectors as well.

The campaign of *MORA* so far has been organized in three phases. We dedicated the period from Jan 16-Feb 13 of 2022 for the preparation of the beamline, followed by the first test run for three days. We managed to seize another beam time three months later for a week. With the progress in these allocated beam times, we managed to have our latest run with more optimized parameters and a sufficient window for the first data-taking process.

4.4 First run *(Feb 13^{th}-15^{th}, 2022)*

4.4.1 Beam Purity

We successfully produced a ^{23}Mg beam ($\sim 10^5$ ions/s) with only 1 μA of the primary proton beam. However, during the first run, we identified considerable contamination from ^{23}Na equivalent to 0.5 nA with 10 μA of primary beam intensity even with a clean sextupole ion guide (SPIG). This has posed a concern as the buncher delivered wider bunches in these conditions. The *Na* contamination appeared instantly with the beam and increased gradually. A ratio of ^{23}Na:^{23}Mg of $\sim$ 20,000 was observed first, dropping to 2,000 with significant optimization. We measured this ratio using the Faraday cups and Si detectors installed in the *IGISOL* line during the experiment.

4.4.2 Bunching

Optimizing with the advanced technique of bunching through a mini buncher was challenging for the light mass equivalent to A=23. A significant amount of work has been carried out to decouple the RF of the segments of the mini buncher to make more efficient tuning. In the later stage, we used the standard "endplate" mode, which provided us with long bunches ranging from 20 to 100 μs, see Fig. 4.5.

As mentioned earlier, these long bunches were challenging to accommodate in the pulsed drift tubes because of the PDT's acceptance value. We encountered significant losses in total transmission from the buncher to the trap of *MORA* varying from 10^{-4} to 10^{-5}, and we ended up with a few tens of ions per bunch in our trap.

4.4.3 Trapping

During the first offline test, we managed to trap the first stable ^{23}Na ions from the buncher, and also, we could optimize in terms of slowing down the ions to 100 eV ions to be trapped adequately in the trap. We gained efficiencies ranging from 5 to 50% for trapping up to 500 ms during the beam time for ions that had passed successfully the PDT2.

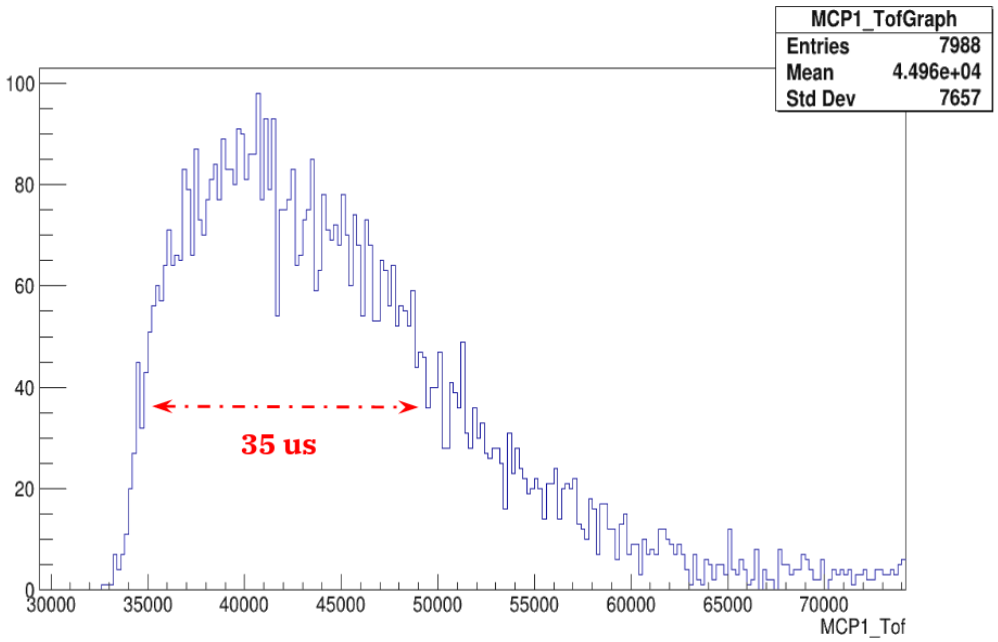

Figure 4.5 – Long ion bunches ranging from 20 to 100 μsec during the first run utilizing only the standard "endplate" mode of bunching.

Technically a tiny fraction of ^{23}Mg was supposed to be considered as trapped (10^{-5} to 10^{-4}), as verified by the Na ions from our first testing with the spark source detected on our MCP2 (off-axis MCP detector) after ejection following the trapping cycle.

4.4.4 Detection setup

As already been addressed in chapter 2, we could find the source of the mysterious persistent background on the RIDE detectors, which was found to be wrongly aligned channels of the MCPs, displaying the accumulated background. Switching the MCP plates (front with the back) helped the recoil ion detectors work nominally before the beam time.
With optimized trapping parameters, we observed the silicon and phoswich detectors working nominally. One can see an example of a slow and fast response from the phoswich detection system as illustrated using Fig. 4.6 obtained during the first run.

High background issues with RF on

In the meantime, we have witnessed the detectors immensely polluted by the switching of the trapping electrodes, as observed/confirmed from FASTER's RHB visualization. The effect of the pulse coming from the switching, most specifically, the R3 trapping electrode, has been handled initially during the first run through offline data analysis and further implemented in the FASTER configuration to see the cleaned spectra from each detector. We briefly discussed this process in section 4.5.4, dedicated to the detection system progress during the second run.

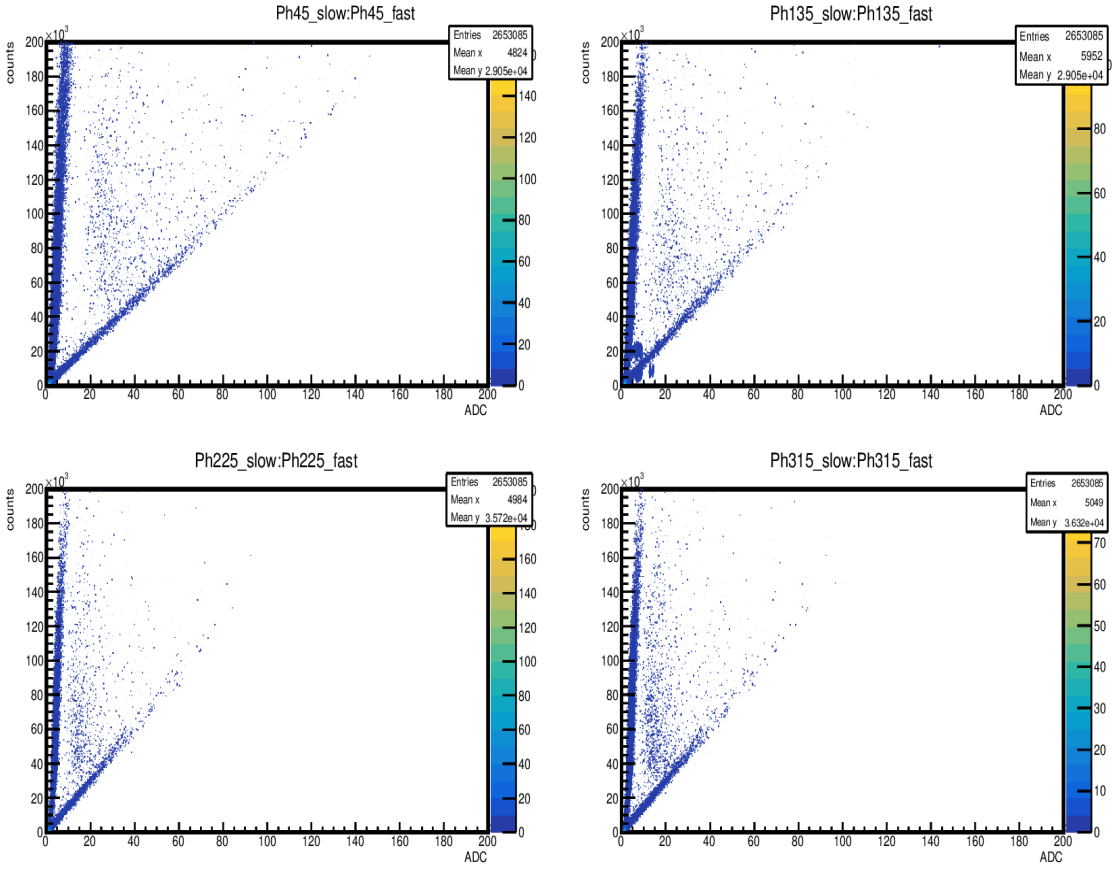

Figure 4.6 – Slow vs. fast response obtained from each phoswich detection system installed at 45°, 135°, 225°, and 315° respectively during the first online beamtime.

However, we observed a very high background on the RIDE detectors as soon as we started the RF for trapping. Unexpectedly the RIDE detectors were polluted with a high noise caused by the RF (at a few 100kHz), see Fig. 4.7. This was unexpected because it was verified that a low pass filter just before the RIDE detectors efficiently suppressed this noise before the *MORA* setup departed from LPC Caen. All the necessary tests involving the beamline and detector tests were done before the final departure of the *MORA* setup.

The exact reason for this high noise was investigated more extensively. The possible assumptions included that, during the initial testing of detectors in LPC, Caen, before their final departure to the *IGISOL* facility, we had calibration masks on the recoil ion detectors, which shielded the RF noise. Despite using a more drastic RF filter during the recent measurements, the noise was still present on all the detectors. Moreover, even more surprisingly, the noise was still present on some detectors despite unplugging the RF electrodes. We assumed the generator produced the noise, and the detector cables picked it up. Several ideas were proposed, which included some significant modifications:

- Replacing the RF amplifier with the refurbished one from the LPCTrap experiment as the RF amplifier was operational and visibly gives a smoother RF signal

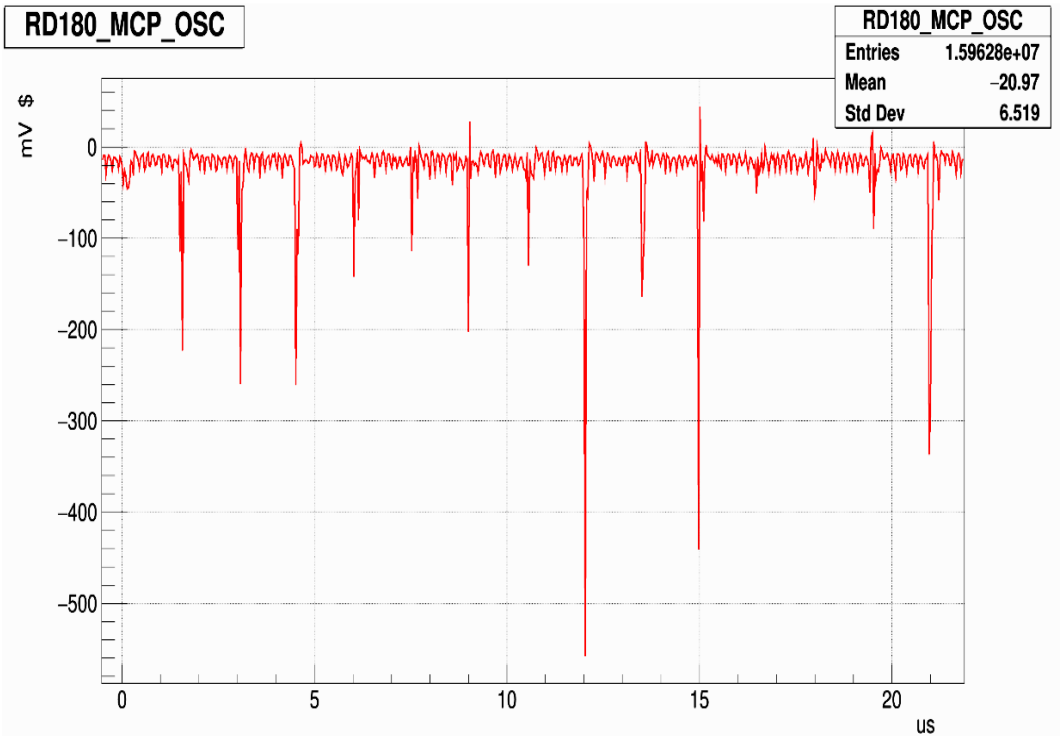

Figure 4.7 – High RF background observed on the RIDE detectors during the first run, which forbade recording the beta-recoil coincidences.

than the currently used CGC one.

- We machined the supports for the fast amplifiers of RIDE detectors so they can be placed as close as possible to the detector outputs.

We could still measure a feeble beta activity in the trap on silicon and phoswich detectors in these challenging conditions. Nevertheless, as we had to turn the recoil ion detectors off because of the high RF noise, we ultimately could not manage to record beta–recoil ion coincidences.

4.4.5 Summary of the first run

Optimistically, tremendous progress was made, including some accomplishments before (first assembly of *MORA* setup) and during the first beamtime (to trap the first ions and get all the detectors working correctly). With reliable production of the Mg beam and bunching techniques and attainable transmission efficiency through the line of *MORA*, we could attain an efficiency as high as 50% with trapping for ions after PDT2 during the beam time. Nevertheless, the technical side was more challenging as we identified a few points, on which we had to improve a lot, which will be mentioned in a later section of the second phase of the *MORA* campaign. Additionally, the reliable evidence of trapped ^{23}Mg ions from the radioactivity of ions seemed to be missing at that point because of the absence of coincidences due to high

background issues of the RIDE detectors. The next beam time was more precisely aimed at resolving part of these issues as well.

4.5 Second run (*May 27^{th}-31^{st}, 2022)*

At the beginning of the beam time, we started by investigating how to clean and bake out the sensitive parts heated by the beam, as it was confirmed that the major source of contamination was the stable Mg target itself. In particular, the target and ion guide head were treated first with demineralized water and in the ultrasound bath. As discussed during the first run, the RIDE detectors were relieved from the noise issues. We finally installed a new FALCO amplifier, eradicating the RF's sharp edges. We observed that this newly employed RF amplifier did not create any noise in contrast with the former CGC RF generator. Only the switching noise generated during the trap electrode switches at injection and extraction remained. But those noises can easily be suppressed by time gating on the cycle, as was applied during the experiment on RHB visualization. Also, the unknown source of background on all MCPs, including the RIDE detectors, could be reduced by the installation of an FTA 820 preamplifier close to the detectors. The overall related progresses during the second run is discussed in this section.

4.5.1 Beam Purity

The ^{23}Na:^{23}Mg ratio varied slightly based on the experimental prerequisites. At the very best, we acquired a ratio varying from 2000 to 500, which was a factor of 2 to 4 times less at most than the previous beam time. During this run, special care was taken in preparing the target. Extensive cleaning of all parts, including the target head and SPIG, did not prove sufficient to suppress the Na contamination.
It was advanced that the origin of the contamination could be two-fold: one which comes from the target when the proton beam hits it, and the other one from the SPIG itself (maybe some sizeable fraction of the $\sim$100pA observed on the switchyard Faraday cup when we used 10 μA of primary proton beam on the target). Using the MR-ToF-MS to scan the composition of the beam as a function of the platform voltage, it was found that both Na and Mg ions were originating from the *IGISOL* target, excluding thereby a major source of contamination coming from the SPIG, situated at a lower potential.

4.5.2 Bunching

The mini buncher technique is an advanced and recent addition to the *IGISOL* RFQ cooler. For this second beam time, the buncher was equipped with a mighty RF generator (400Vp-p 3 MHz). Ultimately, we worked to prepare very short bunches, see Fig. 4.8: Bunches smaller than 500 ns FWHM were sent to our trap instead of 100 μs, using the standard endplate bunching method during the first test run. The narrow bunches were very efficiently transported through the PDTs, with a fixed energy spread and distribution centroid. However, as described above, we suffered from the saturation of bunches from the mini-buncher. We found out that we had a

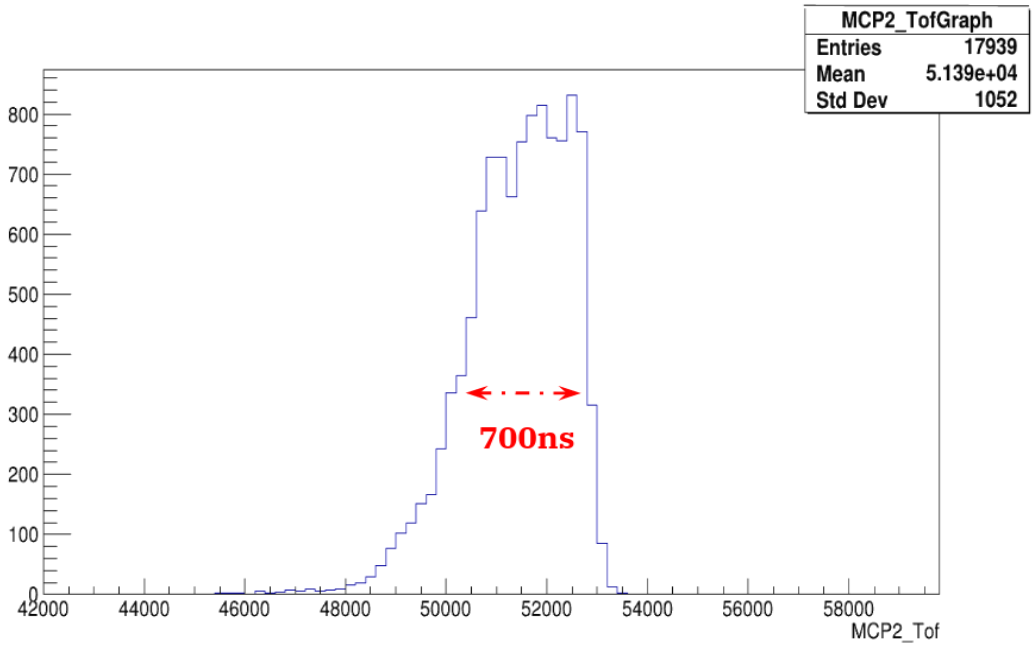

Figure 4.8 – Improved short ion bunches ranging from 500 to 700 ns during the second run utilizing only the advanced technique "Minibuncher" from the RFQ cooler buncher.

saturation regardless of the cycle time at a value of 10^5 ions, which is comparatively lower than the typical value from other traps. This saturation was undoubtedly a consequence of the large contamination coming from Na.

4.5.3 Trapping

Thanks to the Minibuncher, we made tremendous progress on our setup as we got a nearly nominal operation for our trap, up to 5% total efficiency, see Fig. 4.9. However, the main problem stayed the same: the beam contamination with ^{23}Na, only manifesting differently (space charge limitation in the mini-buncher vs. tiny beam acceptance in the PDTs). Based on the statistics obtained above for beam purity and saturation of the mini-buncher, The ratio of ^{23}Mg:^{23}Na being combined with the saturation of the mini-buncher gave us an estimate of about 100 trapped $^{23}Mg^+$ ions per bunch at maximum in *MORA*, which is at minimum $\sim 10^2$ times less than the targeted number. During the tests performed with the MR-TOF, about 10 $^{23}Mg^+$ ions per bunch were observed on MCP1 after purification, which unfortunately couldn't be an option to use due to the saturation of the Minibuncher. The modifications to achieve the target value were considered and listed for the next run time.

4.5.4 Progresses with the Detection setup

The high background on the detection system coming during the trapping period was tackled during the offline data analysis. Thanks to the time cycle information, constructed using the extraction pulse from the trap as a trigger in FASTER, one can only consider the good events by time-gating these noise pulses. An example of the

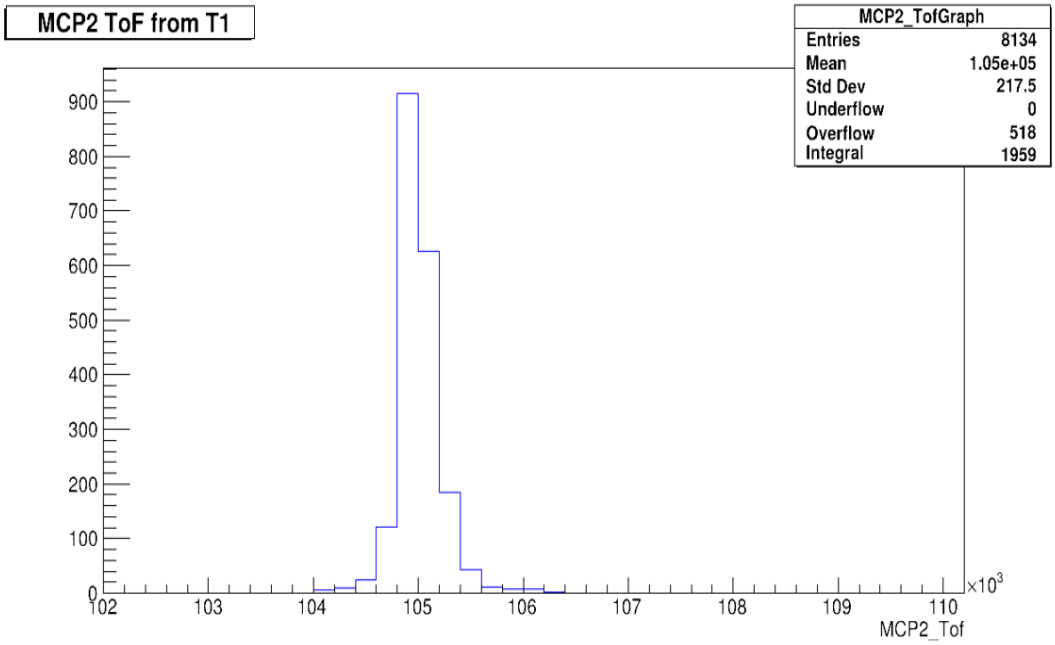

Figure 4.9 – First online trapped ions visible on MCP2, the energy of the ions is 115 eV, with a rate of 10 counts/s considering a trapping time of 60 μs.

applied method is illustrated using Fig. 4.10, where we see the time cycle utilized in

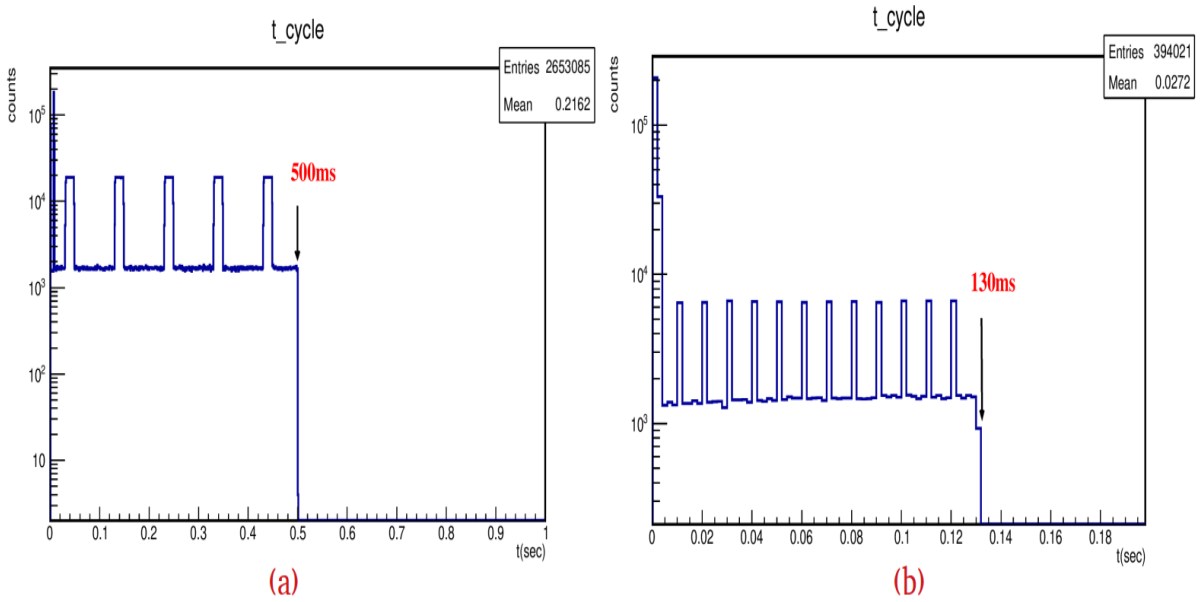

Figure 4.10 – Time cycle information concerning two initial runs of MORA campaign corresponding to (a) 500ms and (b) 130ms, respectively.

two runs of *MORA*. In Fig. 4.11 and 4.12, we can see silicon and phoswich detectors' cleaned spectrum.

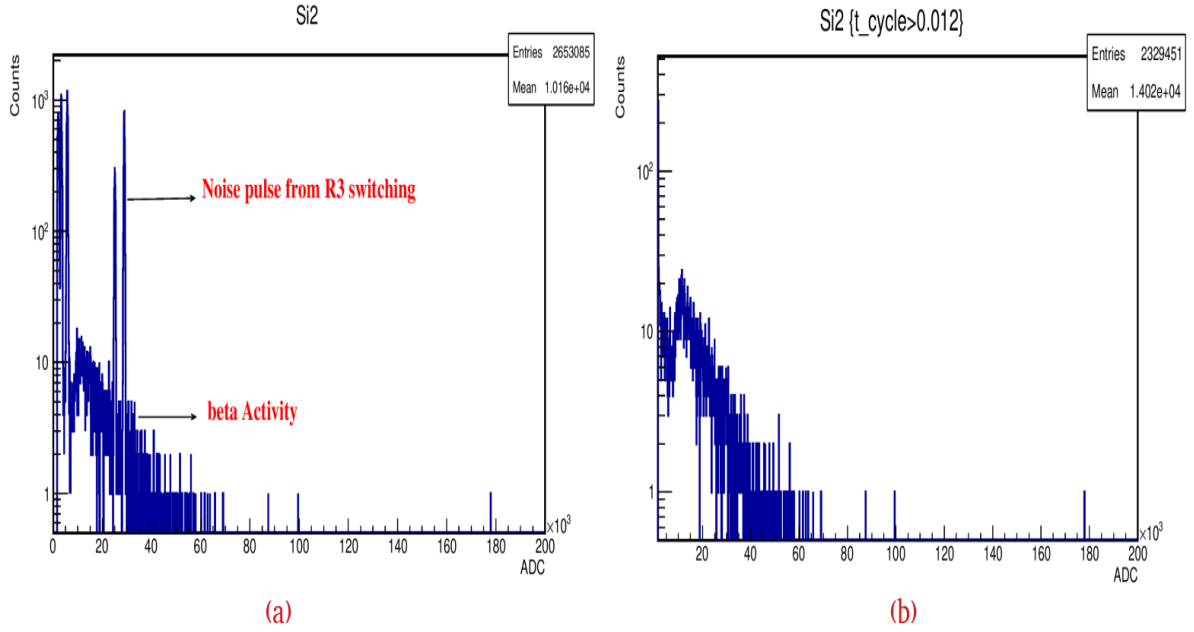

Figure 4.11 – Illustration of the obtained online spectrum with silicon detectors (a) before and (b) after the treatment for cleaning the noise pulses arising due to the switching of trapping (R3) electrode.

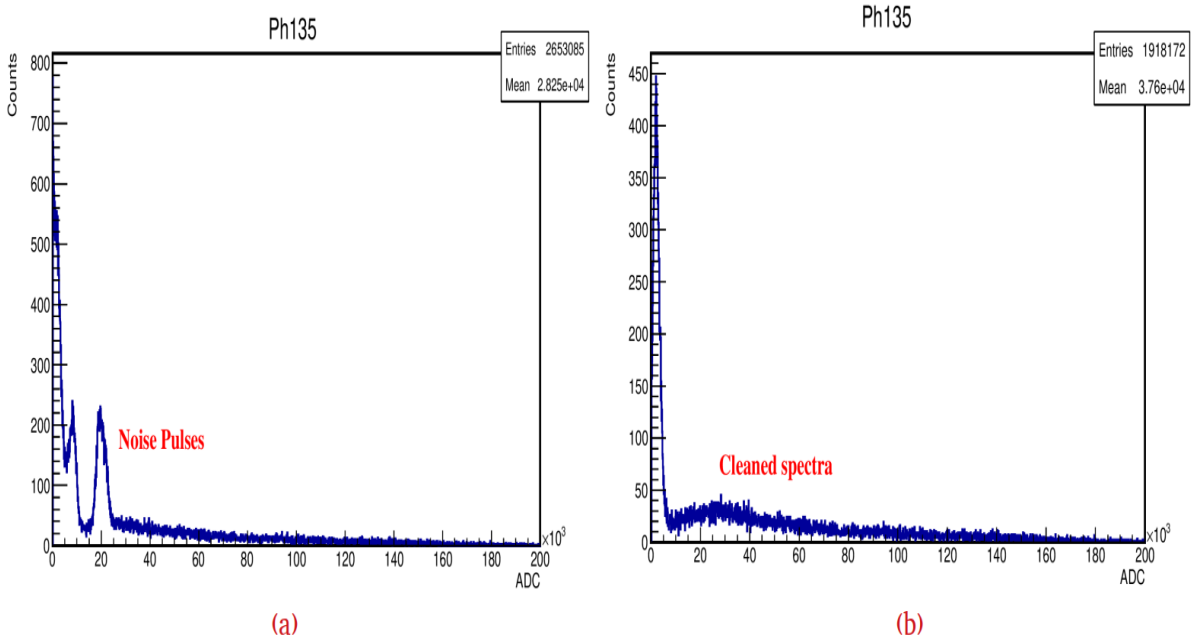

Figure 4.12 – Illustration of the obtained online spectrum with phoswich detectors (a) before and (b) after the treatment for cleaning the noise pulses arising due to the switching of trapping (R3) electrode.

4.5.5 Resulting optimized operation and associated efficiencies

These above-mentioned settings made a nearly optimal operation of the *MORA* PDTs, and a conceivable trap. We got good RF characteristics, eventually making the trapping rather efficient.

The efficiencies were measured by comparing bunch intensities after trapping at MCP2 with currents measured at the attenuation grid installed in the injection line of *MORA* or using FCQ5 (Faraday cup installed in the *IGISOL* line just after the RFQ cooler buncher) or count rates at MCP1.

1. **From Minibuncher to *MORA* trap (global efficiency)**: we typically obtained 1 – 5 % efficiencies with some assumptions to be verified on the correspondence of current measurement on plates/FC and count rate on MCPs.

2. **From slowed down PDT1 ions to *MORA* trap:** up to 10% trapping of the beam measured at MCP1 after being slowed down by our first PDT.

3. **From slowed down PDT2 ions to *MORA* trap:** 30% to 100% trapping of the beam measured at MCP2 after being slowed down by our second PDT.

4. **Trapping times:** 500 ms without losses.

4.6 The latest run *(Nov 11^{th}-14^{th},2022)*

The main objectives before the commencement of the latest beam time during Nov 11^{th}-14^{th} were:

- **Reliability of estimates:** More reliable efficiency estimates with the help of newly installed silicon detectors coming from mini-buncher and the trap of *MORA*, rather than using the standard method of using the MCPs in the line of *MORA*.

- **Longer trapping duration:** In offline and online testing cases, we focused more on attaining the prolonged trapping times close to 11s, corresponding to the half-life of ^{23}Mg (11.3s).

- **First proof of polarization:** Lastly, we attempted the first proof of polarization with an estimation of polarization degree.

4.6.1 Beam purity

A natural Mg target was used as in the other beam times, so no special progress was expected concerning the beam purity. We, however, measured the $^{23}Mg^{2+}$ beam current, which could have provided us with a technique to reduce the contamination since the contamination primarily consists of surface-ionized Na^{1+} ions. In beam production, unlike the last two runs, we could only achieve the ^{23}Mg intensity of the order 2×10^5 ions/s (about a factor of two less than expected) with 10 μA of the primary proton beam. The primary contaminant, Na^{1+}, decreased eventually from 80 pA to 27 pA, while the Mg intensity decreased significantly.

4.6.2 Trapping progress

During the offline testing period, we could trap the ions for the first time at *IGISOL* up to ∼3s, without any substantial losses but with some losses for longer trapping time like 11s. At last, we optimized the trapping with 3s cycles, including 2s of trapping time, during the beamtime, without any loss. As *MORA* eventually targets trapping 10^4 Mg ions in the cloud, more than 10^4 Mg ions in the mini buncher were considered as a target to achieve. With the persisting level of contamination, the number of Mg ions in the MORATrap was less than 2 orders of magnitude.

4.6.3 Acquired Efficiencies

Table 4.1 shows a summary of the results obtained in the 3 beam times. During the

From IGISOL target (pps)	Cooler efficiency	Efficiency due to space-charge limit	PDT efficiency	Trapping efficiency	Total No. of trapped ions/cycle
Feb, 2022					
1,000,000	0.1	1	0.01	0.01	10
May, 2022					
1,000,000	0.1	0.01	1	0.1	100
Nov, 2022					
200,000	0.1	0.05	1	0.1	100

Table 4.1 – Tabulated illustration of trapping progresses considering each contributing factor during two experimental runs, conducted in Feb 2022, May 2022, and Nov 2022 at the IGISOL facility.

last beamtime, the mini buncher delivered up to 4×10^5 ions/bunch. A 10% transmission efficiency from the front end to the Si installed at the entrance of *MORA* could be measured when the mini buncher of *IGISOL* was not saturated. The efficiencies decrease when in saturation. With the contamination observed (Na:Mg∼1000), the mini buncher saturated at about 200 Mg ions per bunch. The trapping efficiency was re-measured with MCPs and the segmented Si detectors surrounding the MORATrap. The MCP efficiencies were challenging to rely on.

To estimate the efficiencies, we compared the rate of MCP2 after trapping with the rate of MCP1 just after the Si detector at the entrance of our beamline. The two MCPs were found to react quite differently to our attenuation meshes. According to the configuration, efficiency estimates for the trapping varied between 1% and 15%. The Si detectors with online visualization showed activity consistent with about 10% efficiency, i.e., 20 Mg ions trapped per bunch, which is more realistic than the optimistic value shown in 4.1, based on the lowest contamination ratios observed.

4.6.4 Data taking, progress on the setup

We started acquiring the data when the optimization for the trapping parameters reached its nominal value. All in all, we dedicated 72 hours to the online experiment and a few hours to offline calibration and tests for detectors. Around 4h30m was dedicated for background measurement.

The measurements were taken with lasers ON (with σ^+ and σ^- laser polarization) and OFF. We also have improved with laser power as compared to the last run, we used 130 mW laser power at 280 nm, and it was steadily delivered to our trap for polarization. The number of ions captured in the trap was relatively steady, apart from occasional losses due to unexplained instabilities in our first PDT. The latter could be fixed by switching on and off the HV supplies. A $\sim$20% decrease in the yield in two days and drifts of optimal tensions in the front end were observed, but those could eventually be handled.

We used buffer gas cooling for the last ten hours. He cooling was not used before because it was found to be detrimental to the trapping half-life during early tests in LPC Caen. The ion cooling method requires a careful choice of the thermalization gas: the atoms of buffer gas must be much lighter than the ion to be cooled (here, we use ^4He for fast, efficient cooling. With 10^{-5} mbar of He in the trap, the trapping efficiency was reduced by 10 - 20%. In this regard, we investigated each detector extensively. The injection of He mainly affected the background on MCP data, as discussed in the following.

4.6.5 Data analysis and first preliminary results

Our latest online beamtime was carried out with optimized trapping parameters and the nominal working of our detectors. The first estimate of the polarization degree was therefore investigated, which requires a sizeable asymmetry between the two silicon detectors for monitoring ion bunches' polarization.

We accumulated 30h of data for the polarization measurement. In the analysis, we only used the 10h with He cooling, as cooling is expected to increase the polarization rapidity. The He cooled data was taken under three different conditions, alternating runs of 1h of the different types.

1. The first type of run was taken for 3h with He buffer gas injection in the presence of lasers and by inserting the half-wave plate in the path of the circularly polarized laser beam.

2. Another set of runs in the presence of lasers but without inserting the half-wave plate to reverse the polarization direction, again for 3h.

3. The last set of runs was taken without the lasers ON (no polarization) during the decay of trapped ion bunches for 2h, still in the presence of He.

Before initiating the investigation of asymmetry observed on the silicon detectors, we confirmed the ion's trapping with activity observed in RIDE detectors, as illustrated with Fig. 4.13. This figure was taken with He injection. The cycle starts with the trigger of FASTER, which corresponds to the ejection of the cloud. An overall background, consisting of off-trap decays and other events due to the environment of the detectors (He atoms triggering the MCPs, ions created in the vicinity of Penning gauges), is measured during 1s. During the next 2s, a new bunch is injected and trapped. An increase in the activity measured by the RIDE detectors can be observed. As was eventually understood, this activity is mainly due to the evaporation of the

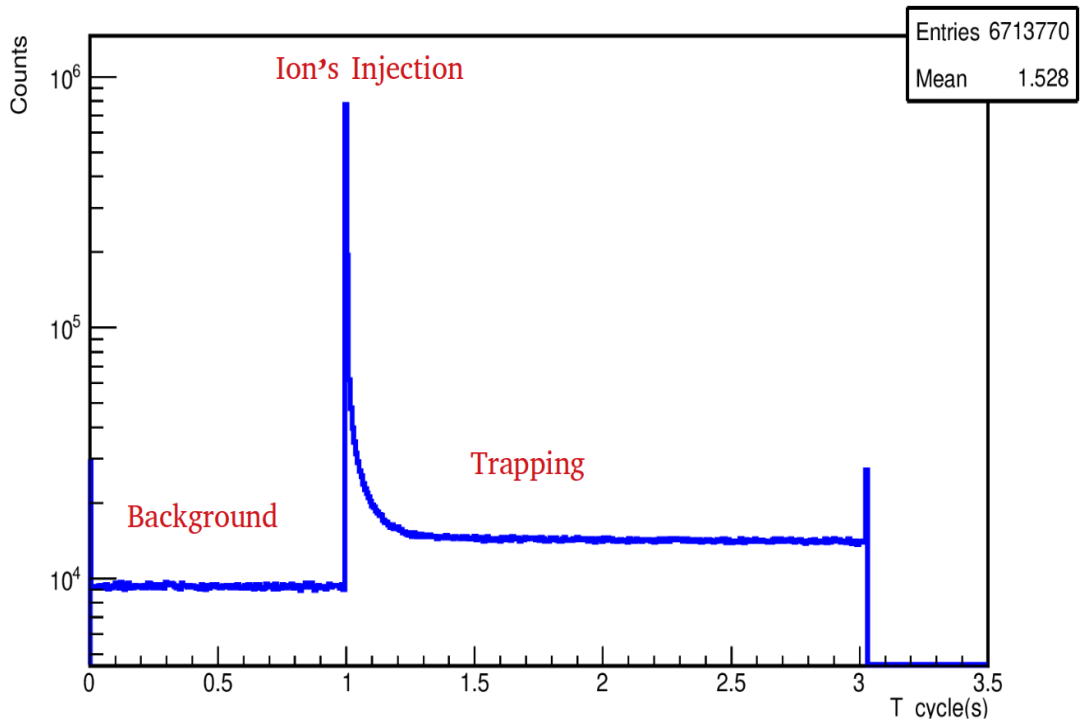

Figure 4.13 – RIDE counts with respect to the cycle time of 3 sec, illustrating 2 sec of trapping time, a considerable difference in the count rate during the trapping is observed.

ion cloud and not to recoils from the decay of ^{23}Mg ions. The same activity was actually measured without He cooling. We can see a considerable difference in the rate with respect to with and without the He injection, as illustrated using Fig. 4.14. This figure presents the count rate on RIDE detectors during the trapping cycle only (from 1s to 3s, see 4.13), with He and without He cooling. The rate is integrated on 1h for both configurations and subtracted from the background measured after ejection of the cloud on MCP2 (0 to 1s on Fig. 4.13).

The recorded events are interpreted in Fig. 4.14 as ions evaporated and not recoils because of their high rate (a much higher rate than what is seen with betas detected on phoswich) and because of their characteristic decay times (too short or too long compared to the half-life of ^{23}Mg). The comparison of black and blue curves attests to hot ions in the bunch/cloud, which eventually boil off from the trap. Without He injected, the evaporation rate decreases over the whole trapping time. With He injection, evaporation follows the same trend as without He, but after 200 ms, it reaches a steady state, with a very slight decrease. This decrease can be fitted with an exponential half-life of several min (4$\pm$1min). The latter is way longer than the ^{23}Mg half-life (about 11s). This constant evaporation is interpreted as the result of the thermal agitation sustained by collisions, which eventually brings ions out of the trap. It should also be noted that the cloud is mainly composed of ^{23}Na stable nuclei. The

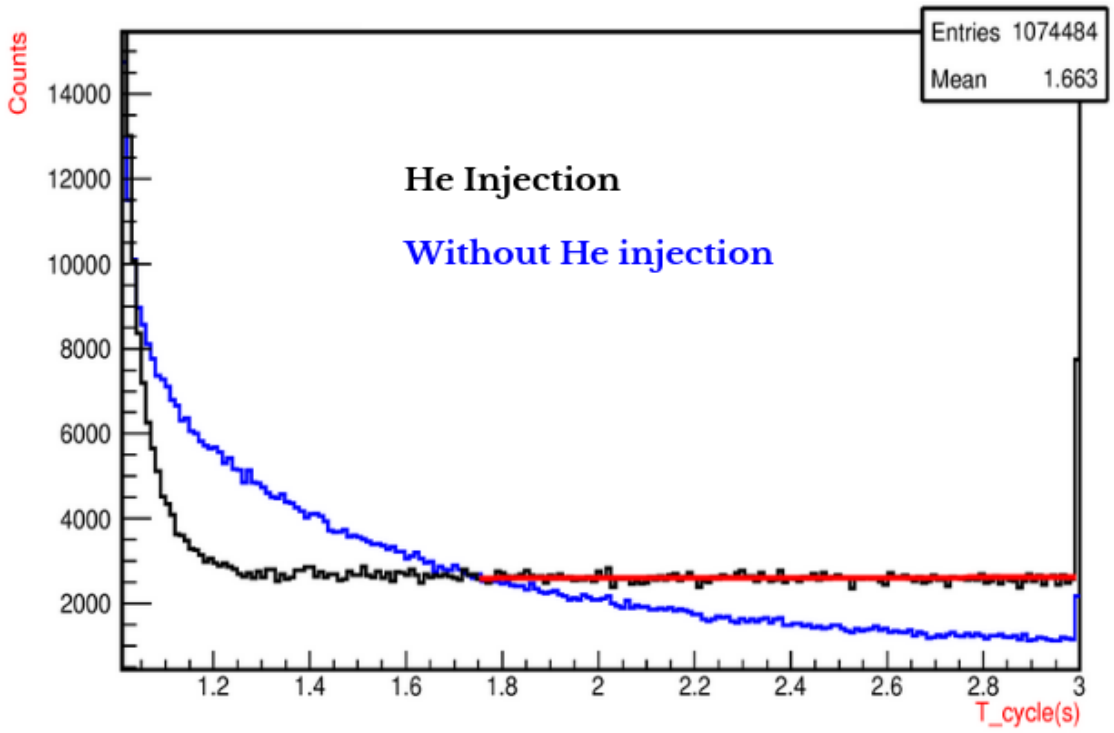

Figure 4.14 – Ion's evaporation observed during the cycle time corresponding to 3sec (blue) in the presence of He gas injection, (black) in the absence of He gas injection. This data corresponds to integrated count rates on RIDE detectors for a period of 1h.

evaporation must be proportional to the number of ions in the trap. In contrast, evaporation should stop in the absence of He gas once the hot ions have left the trap's fringe fields. The core of the cloud, cold enough and in a region where the field is quadrupolar, should remain trapped. This is the behaviour that is suspected in the case of the blue curve: would the cycle be longer by a few s, the evaporation should tend to 0.

In the case of He cooling, as the evaporation is supposed to be proportional to the number of trapped ions, the fitted half-life should correspond to the trapping half-life. The latter is actually much longer than the trapping half-life measured without cooling by ejecting the ion cloud on MCP2 (5 to 10s). It should therefore be confirmed by a direct measurement before the next experiment. But this observation readily gives hope for a very long trapping half-life with He cooling.

We focussed first on single β events that the annular silicon detectors should observe. However, we compromised because of some evident noisy sectors out of eight sectors in one silicon. In the meantime calibrating the detectors in the same environment was one of the foremost requirements. We had to perform the calibration again, as mentioned while concluding the chapter 3 dedicated to silicon detectors. Many modifications were done after the detector's installation in the MORA chamber while

testing them during the online beam time. We lost the calibration, as it was evident from the raw data that the detector's gain was manipulated by changing the shaping time of the spectra in the FASTER acquisition system. The FASTER acquisition parameters were most often manipulated due to the observed high background.

The calibration of all the silicon sectors, obtained with the offline radioactive finger having a radioactive source of Sr-90, has shown to be difficult because of not having a discrete peak structure in the decay spectrum. We carried out PENELOPE simulations, to analyze the results, as shown using Fig. 4.15.

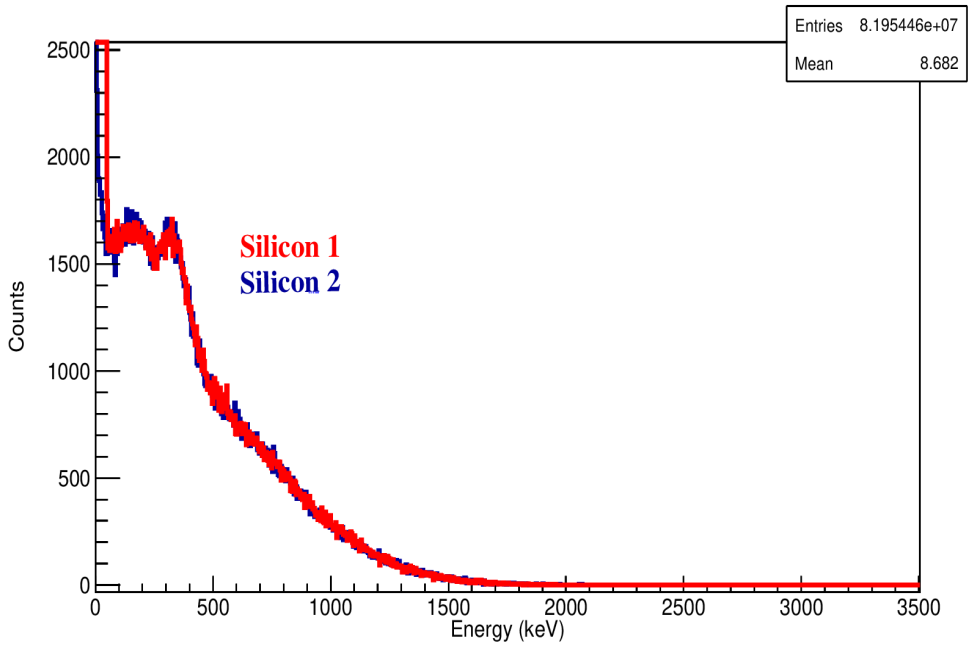

Figure 4.15 – PENELOPE simulations done for beta decay spectrum of ^{90}Sr for two annular silicon detectors installed in the trap axis of MORA.

The steps taken into account were the following:

- We first calibrated the detectors with the Sr-90 source using chi-2 minimization for each sector individually. We then produced the calibrated online spectra by cleaning the pulses from electrode R3 using time gating.
- The specific methodology adapted to only consider the good events during the trapping period also required subtracting the events coming from off-trap decays, time gating on the first second of the cycle as seen by FASTER.
- One can see an example of the calibrated, cleaned, background subtracted spectrum obtained in the case of Si2 in the presence of lasers (σ^+ polarization) illustrated using Fig. 4.16. This data can be used for the determination of the polarization degree using the beta asymmetry 3.2.

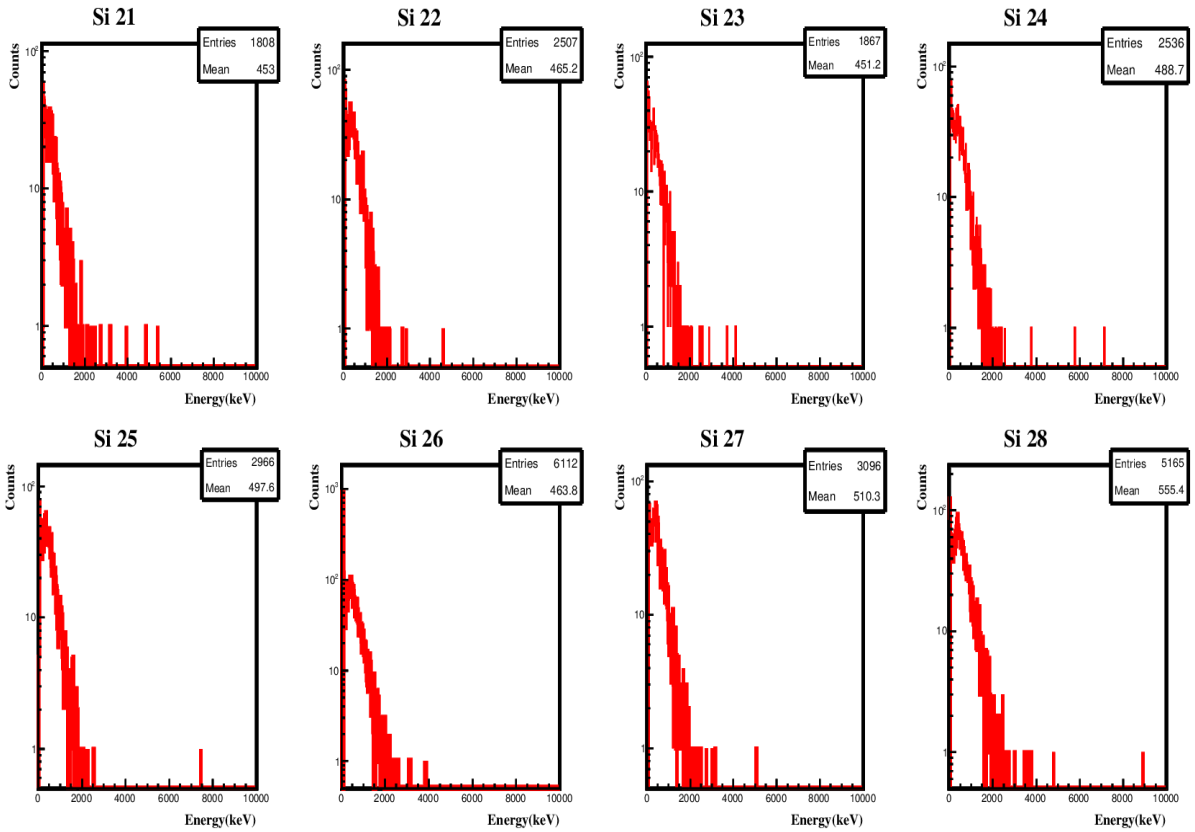

Figure 4.16 – Cleaned, background subtracted and calibrated online spectrum obtained in the case of Si2 in the presence of lasers (σ^+ polarization) for the total of 8 sectors

- Another way of determining the P value is by assessing the observed coincidence with recoil ions, thanks to the RIDE detectors in this scenario, which eventually helps to minimize the high background. Then, in this case, the symmetry can be reformulated as a linear combination of the β and neutrino asymmetry coefficients (see eq. 3.2).

- Regarding coincidences, we considered the coincidence time window of 5μs between a detected recoil by the RIDE detectors and β's detected on silicon detectors, which has been specifically selected in this case because of the typical time-of-flight of ions to their detectors.

As said earlier, the entire cycle considered during this run is equivalent to 3.03 sec, constituting 2 sec of trapping time and 1 sec of off-trap decays at the beginning of the cycle, see Fig. 4.17.

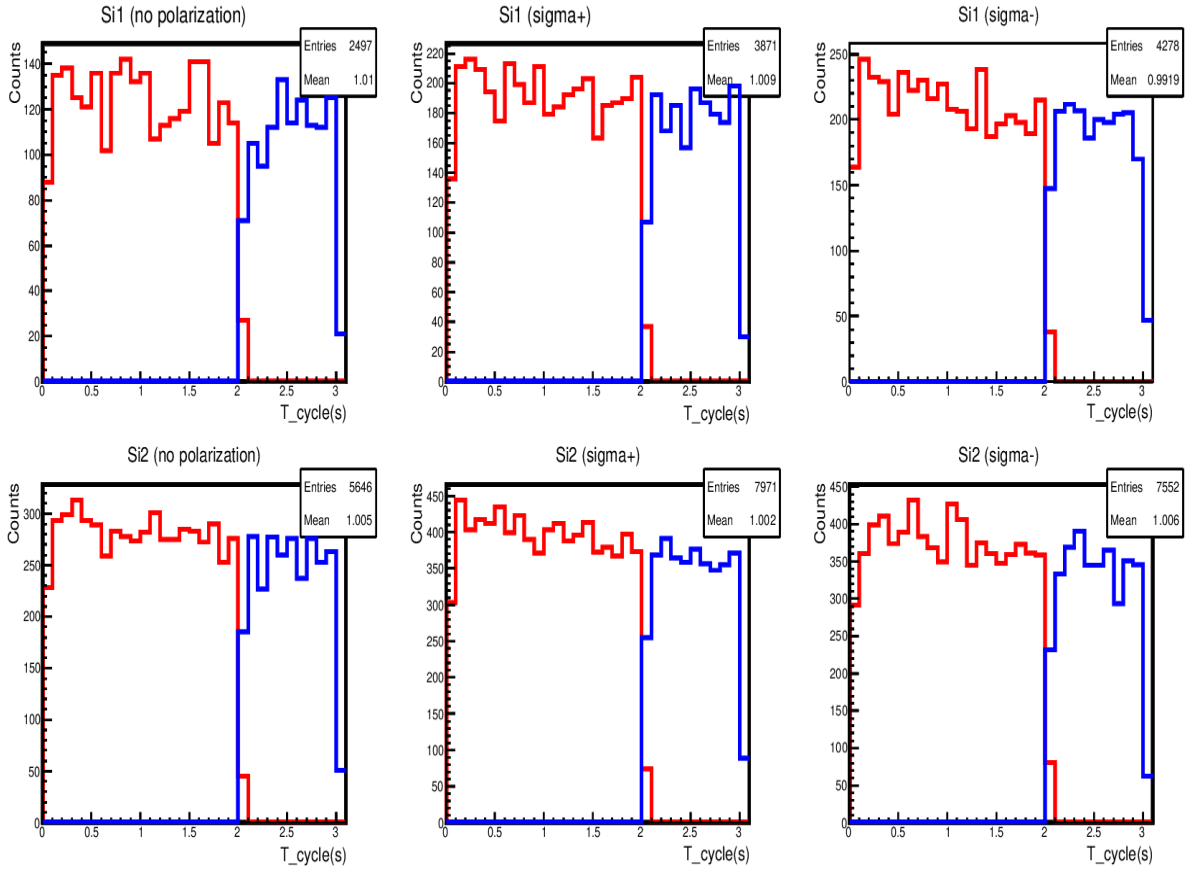

Figure 4.17 – Comparison of in-trap decays (red) during the trapping time of 2 sec and off-trap (blue) decays during the period of 1 sec, taking into account the singles β events observed with each sector of the silicon detector.

To subtract the off-trap background during the trapping period, we take into account the normalization factor

$$factor = \frac{e^{-\lambda t_{(0)}} - e^{-\lambda t_{(1)}}}{e^{-\lambda t_{off(0)}} - e^{-\lambda t_{off(1)}}} \cdot \frac{1}{e^{-\lambda t_{cycle}}} = \frac{N(t = t_{(0)}) - N(t = t_{(1)})}{N(t = t_{off(0)}) - N(t = t_{off(1)})} \times \frac{1}{N(t = t_{cycle})} \tag{4.1}$$

λ being the radioactive decay constant,

$$\lambda = \frac{\log 2}{T_{1/2}(^{23}Mg)} \tag{4.2}$$

where, t_{cycle} corresponds to the total bunching cycle of **3.03s**,
$t_{(0)}$ is the initial timing of the trapping period equivalent to **1.03s**
$t_{(1)}$ is the final timing of the trapping period equivalent to **3.02s**
$t_{off(0)}$ corresponds to the beginning of the bunching cycle **0.1ms**
$t_{off(1)}$ corresponds to the end of off-trap decays and the beginning of the trapping

cycle, **0.99s**

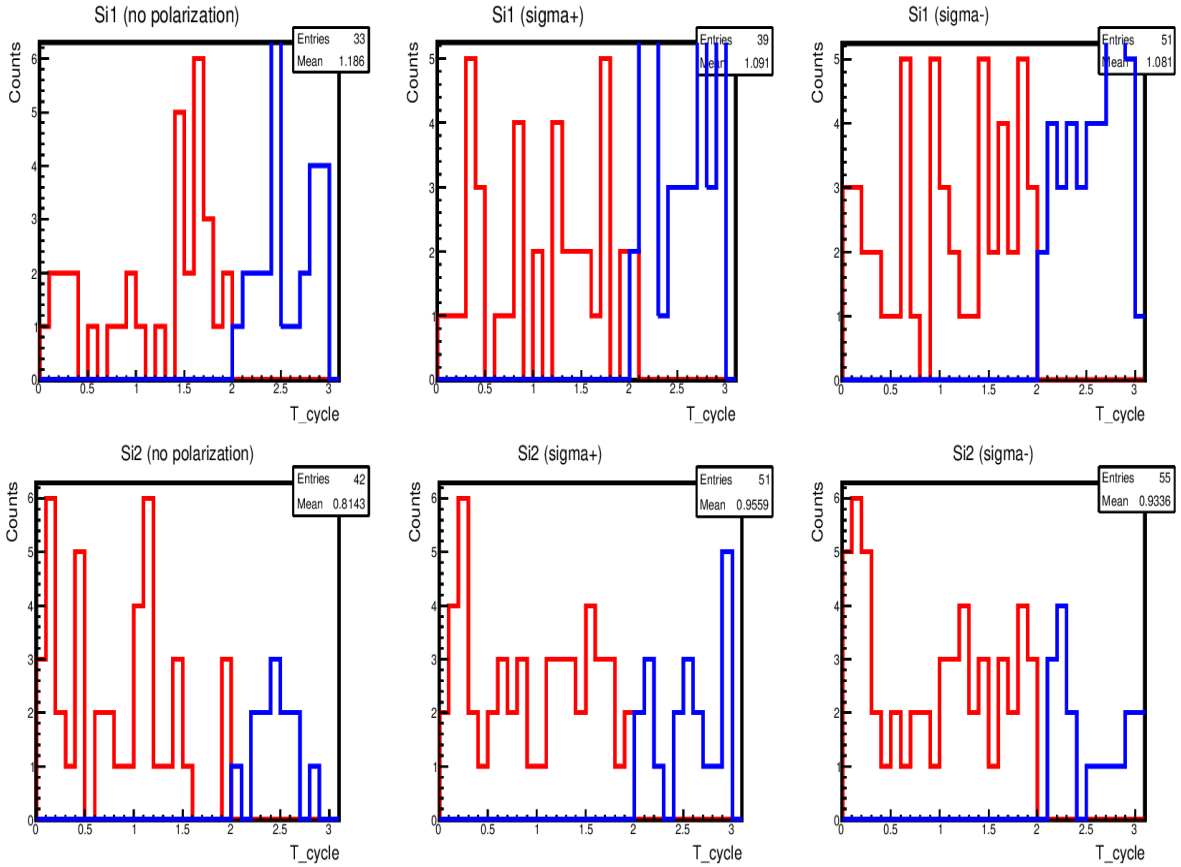

Figure 4.18 – Comparison of in-trap (red) decays during the trapping time of 2sec and off-trap (blue) decays during the period of 1sec, taking into account the coincidence with β events observed with each sector of the silicon detector and the recoil ions with RIDE detectors.

Using these calculations allows us to obtain the absolute number of counts on both silicon detectors during polarization in one direction and after reversing the polarization. We presented the whole process of the determination of the experimental asymmetry by tabulating the relevant statistics in Table 4.2 and 4.3. This process is duplicated in the case of single beta events and recorded coincidences. A varying threshold on the energy spectrum obtained with the annular silicon detectors is applied. To be consistent, we excluded the same sectors of Si2 as the noisiest sectors of Si1 (2, 4, and 8) from the analysis. The tables illustrate the unfavorable signal-to-noise ratio (1:100). Many detected events come from off-trap decays. In comparison, a very small number of trapped ions is observed. After background subtraction, this number is sometimes even negative. The computed asymmetries and associated error bars have no physical meaning.

According to Monte-Carlo simulations, assuming a full polarization of the cloud, an absolute value of about 0.5 is expected for asymmetries using single events and

about 0.2 for those using coincidences. We also computed the total number of estimated trapped ions/bunches using the eq. (4.3) based on observed statistics after the offline data analysis.

$$N_{ions(trapped)} = \frac{\frac{N_{(Si1,Si2)}}{\Omega} \times \frac{T_{1/2}}{\log(2)} \times \frac{t_{cycle}}{t_{trap}}}{T} \tag{4.3}$$

where:
$N_{ions(trapped)}$ is the number of trapped ions in a bunch
$N_{(Si1,Si2)}$ is the total number of counts on Si1+Si2.
$T_{1/2}$ is the ^{23}Mg half-life which corresponds to **11.3 s**
t_{cycle} is the total cycle of **3.03 s**
t_{trap} is the trapping time of **2 s** out of the total cycle
Ω is the detection solid angle for Si1 & Si2 (between 0 and 1)
T is the duration of the measurement (3 hours).

The total counts on the silicon detectors shown in the tables correspond to T =3h of data taken with polarization and a detection solid angle of $\Omega = 0.05$ determined from simulations in the case of two silicon detectors. Using $N_{(Si1,Si2)}$ = 500 single betas detected, this gives about 30 ^{23}Mg ions trapped par bunch.

If one considers the number of recorded coincidences, one needs to account for other efficiencies:

- The MCP detector efficiency due to a geometrical factor (the so-called open area ratio) which corresponds to 50%.
- An 8% of solid angle coverage in the octagonal arrangement of MORA
- The shake-off process (50% of ions after the decay, the others are neutral),

We obtain a total efficiency of 2% for detecting ions. With about 20 coincidences for 3h of data taking, we estimate about 60 ^{23}Mg ions trapped par bunch. This number has to be compared with the 30 ^{23}Mg ions trapped par bunch calculated with the single betas. These orders of magnitude are proven to be insufficient for a sound asymmetry determination with the current accumulated data.

4.6.6 Outline of the Last Run

With the last online beam run and preliminary data analysis, we could not estimate the polarization degree due to too low statistics, as, with current observations, we see a feeble signal. Therefore, no clear conclusions could be drawn on the polarization degree. However, the data analysis is still in progress.

Few suppositions to consider

1. While building the asymmetry for the P degree estimate in the case of silicon detectors, we assumed the efficiency should be the same as we have identical

Polarization	**Si1**		**Si2**	
Without background subtraction				
	Trapping	*Background*	*Trapping*	*Background*
σ^+	5459	2537	10994	5011
σ^-	6106	2772	10503	4799
No polarization	3576	1657	7803	3573
With environmental background subtraction				
	Trapping	*Background*	*Trapping*	*Background*
σ^+	4385	2006	9455	4213
σ^-	5032	2241	8964	4001
No polarization	2860	1303	6777	3041
With off trap decays subtraction (background measured after the ejection of ion cloud)				
σ^+	-38(169)		166(227)	
(N_{Si2}-N_{Si1})	-204(283)			
Observed asymetry (N_{Si2}-N_{Si1})/(N_{Si1}+N_{Si2})	-1.58(4.14)			
σ^-	91(175)		142(224)	
(N_{Si2}-N_{Si1})	-51(284)			
Observed asymmetry (N_{Si2}-N_{Si1})/(N_{Si1}+N_{Si2})	-0.22(1.24)			
No polarization	-13(128)		72(180)	
(N_{Si2}-N_{Si1})	-85(221)			
Observed asymmetry (N_{Si2}-N_{Si1})/(N_{Si1}+N_{Si2})	-1.43(6.49)			

Table 4.2 – Tabulated count rates in Si1 and Si2 during ($\sigma^+\sigma^-$) and in the absence of polarization. The table shows the raw count rates measured during trapping and after the ejection of the cloud. They are followed by count rates corrected from the environmental background (middle). The environmental background has been measured after the beamtime (without ^{23}Mg injection). At the bottom, the count rates corrected from off-trap decays allow us to calculate asymmetries with their associated uncertainties.

Polarization	**Si1-RIDE(coinc.)**		**Si2-RIDE(coinc.)**	
Without Background subtraction				
	Trapping	*Background*	*Trapping*	*Background*
σ^+	302	100	77	23
σ^-	328	106	72	21
No polarization	231	82	65	13
With environmental background subtraction				
	Trapping	*Background*	*Trapping*	*Background*
σ^+	154	54	65	23
σ^-	106	37	54	21
No polarization	83	36	52	13
With off trap decays subtraction (background measured after the ejection of ion cloud)				
σ^+	35(39)		14(15)	
(N_{Si2}-N_{Si1})	21(42)			
Observed asymetry (N_{Si2}-N_{Si1})/(N_{Si1}+N_{Si2})	0.42(0.92)			
σ^-	24(50)		8(15)	
(N_{Si2}-N_{Si1})	17(52)			
Observed asymetry (N_{Si2}-N_{Si1})/(N_{Si1}+N_{Si2})	0.52(1.84)			
No polarization	4(37)		24(12)	
(N_{Si2}-N_{Si1})	-21(39)			
Observed asymetry (N_{Si2}-N_{Si1})/(N_{Si1}+N_{Si2})	-0.74(1.74)			

Table 4.3 – Tabulated coincidence count rates with Si1 and Si2 during ($\sigma^+\sigma^-$) and in the absence of polarization. The coincidences are conditioned by detecting an ion in a RIDE detector in a 5 μs window following the detection of a beta. The table shows the raw count rates measured during trapping and after the ejection of the cloud. They are followed by count rates corrected from the environmental background (middle). The environmental background has been measured after the beamtime (without ^{23}Mg injection). At the bottom, the count rates corrected from off-trap decays permit the calculation of asymmetries with their associated uncertainties.

scenarios for both the silicon detectors in terms of geometry, configuration, and the possible effect of backscattering.

2. Suppose the point mentioned earlier is not the case here. In that possibility, another way of probing the value of P is by assessing self asymmetries by considering the difference of detected beta events in one silicon detector with and without the spin-flip.

3. In the current status of the data analysis, such self-asymmetries give a similar result: no evidence of polarization yet, due to insufficient statistics. According to the simulation, the expected asymmetries should be ± 0.5 for singles and ± 0.2 for coincidences. However, suppose one refers to the tabulated data in Table 4.2 and 4.3. In that case, we see that the observed asymmetry has too large error bars to give any indication and even to have physical meaning (asymmetries have to be comprised between -1 and 1).

4. A few assumptions were made to explain the overwhelming background during our first investigation. This background is probably because we implant some ions close to the detectors during the injection or ejection phase. For single events, we see a higher background on the detector, which is placed in the direction of the beam while ejecting the ion bunches on MCP2.

5. We also see a non-negligible background of off-trap events, even for coincidences. These coincidences are most likely fortuitous. The number of real coincidences coming from trapped ions is probably overestimated. During trapping, the probability of fortuitous events is expected to increase because of the higher count rate on the RIDE detectors (see Fig. 4.14).

4.7 Conclusion and envisioned improvements

To enable the proof-of-principle of the polarization technique, as the first step towards a precise measurement of the D correlation, substantial measures must be taken to improve beam purity to obtain cleaner Mg ion bunches. Longer trapping times for ion bunches can help decrease the off-trap background. Acquiring the data for extended periods should also help to determine the trapped cloud's polarization degree.

1. **Reaction mechanism and hot cavity**: Some dedicated efforts to purify the beam are to be pursued. A new approach can also be considered for beam production, which can provide a long-term solution: employing another reaction mechanism to change target components. One could use a fusion evaporation reaction. (like 12C+12C) in a hot cavity. The hot cavity should permit eliminating the Na contamination by going to high temperatures for an extended period (>1500°C to desorb any Na from the target ion source).

2. **Purified bunched beams with the MRTOF:** In our initial tests, we attempted to purify the bunches delivered from the mini buncher. After a few ms of trapping in the MRTOF, and irrespective of the intensity of the bunch (from a

few 100 to 10^5 ions/bunch), the Mg could be efficiently separated (almost with $\sim$100% efficiency). This was a phenomenal result and gave us credit for a future re-bunching/accumulation scenario, where mass-separated bunches would be stacked at a relatively high frequency (100 Hz) in a dedicated buncher to be inserted between the MR-ToF-MS and MORA. On the other hand, it did not improve the situation in our case effectively, as this separation was done after the mini-buncher.

3. **Modified Mg target**: A new production test with a modified Mg target has also been scheduled during the mid of 2023, as beam purity remained the primary concern in our case. This target should be coated with a thin Ba layer to suppress Na's surface ionization by decreasing the emitting surface's work function.

Conclusion and future Perspective

In this thesis work, we predominantly have focussed on the dedicated new detection setup of MORA, consisting of beta and recoil ion detectors for measuring the D correlation parameter in the trapped ion's decay of ^{23}Mg.

We developed the new Recoil detection system (RIDE), which includes the usage of a reflective anode (PTFI) used for determining the x and y position. We applied a higher-order correction algorithm in image reconstruction up to third order followed by obtaining a resolution of 0.8 ± 0.4 mm in x and 0.9 ± 0.4 mm in y with a position accuracy of better than 80μm in the center part of the detector image. We also acquired an absolute detection efficiency by taking advantage of techniques like offline ion sources for efficient transport of ions, together with fast switching techniques. These techniques assisted in determining the detection efficiency as a function of the energy of the incident ions. An ideal efficiency reaching the maximum limit at 45 %, saturating at ion energies ranging from 3.5 to 5 keV, was measured with our detection setup.

A set of annular segmented silicon detectors should allow us to study the acquired degree of polarization of trapped ion bunches in detail. Successful testing of our detectors was made while making progress on reducing the different noise sources, with many modifications introduced in the setup and electronics. We selected the best preamplification system during the characterization process. We tested each of the detectors individually in the presence of alphas and electrons with and without the aluminum protection cover protecting the active surface of the detectors from laser light reflections. An attenuation of $\sim$40 keV was observed in the latter case. The detectors were tested successfully and simulated with the PENELOPE code in both cases. We achieved a detector resolution of 25-30 keV in the presence of electrons and 30-34 keV in the presence of alphas.

The campaign of MORA so far has been organized in three phases. The first installation of the MORA setup was done at the beginning of 2022 at the IGISOL facility of Jyväskylä, followed by the first proof-of-principle experiment. Excellent progress was made during the MORA setup's first assembly and beamtime to see the first trapped ions and get all the detectors functioning correctly. With reliable production of the ^{23}Mg beam and despite a low transmission of the beam through the pulsed drift tubes, because of the bunching technique employed, we could attain an efficiency as high as 50% with trapping for bunches passing through PDT2 during the first run.

The main objectives in the next beamtime were thoughtfully listed; on the technical side, we made much progress, more related to the high background problems arising from the RF generator. The newly employed FALCO amplifiers helped to eliminate the RF's sharp edges. A high reduction of background with the RIDE detectors followed this improvement. The ^{23}Na:^{23}Mg ratio was improved from the factor 2000 to 500, 2 to 4 times less at most than the previous beamtime. The beam purity was improved by extensive cleaning of sensitive heated parts by the primary beam, the target, and the havar windows of the ion guide in particular. Eventually, during this period, we could use the advanced technology of the Minibuncher of the IGISOL RFQ. Significant progress was made thanks to sub-microsecond bunching. The overall trapping efficiency was estimated to reach 5 to 10%, with$\sim$100 Mg ions/bunch in a cycle.

During the last run, we focussed on attaining more reliable efficiency estimates from the Minibuncher and the trap of MORA using Si detectors as diagnostics rather than using the standard method of using MCPs of the beam line. All the detectors worked nominally with no significant observations of background as observed in the past due to many technical reasons. Alongside, we reached the prolonged trapping times close to the half-life of ^{23}Mg (11.3s). Lastly, we attempted the first proof of polarization by estimating the polarization degree.

We recorded data for a longer trapping time equivalent to 3 s for the first time at IGISOL, with improved trapping efficiency estimates, thanks to newly installed silicon detectors just before the line of MORA. The data was accumulated for 30 hours for the first polarization test. The measurements were taken in the presence of lasers (with σ^+ and σ^- polarized light) with an improved laser power of 130 mW at 280 nm compared to the last two runs delivered to our trap. A few runs were also taken without lasers for a reliable comparison. Initiation of the analysis started with the calibration of silicon detectors. We calibrated the individual sectors using a Sr-90 radioactive source in the MORA chamber. We used time gating to subtract the pulsed background from trapping from the charge spectrum. We subtracted the events from off-trap decays only to consider the good events during the trapping period. We estimated that we could trap $\sim$30 ^{23}Mg ions per bunch. In another approach to assess the P degree, we considered the observed coincidences with recoil ions using RIDE detectors, which also helps to reject the higher background.

In both cases, we observed an asymmetry with large error bars preventing any conclusion drawn on the degree of polarization. The obtained orders of magnitude are demonstrated to be insufficient for a sizeable asymmetry determination with the current accumulated data. However, on the bright side, we still can improve on many factors, as discussed while concluding the chapter 4, which will help us in future experiments. Different means were envisaged to produce the Mg beam with a widely suppressed contamination coming from the primary contaminant of Na in the current scenario.

Bibliography

[1] P Delahaye, E Liénard, I Moore, M Benali, ML Bissell, L Canete, T Eronen, A Falkowski, X Fléchard, M Gonzalez-Alonso, et al. The MORA project. *Hyperfine Interactions*, 240:1–13, 2019.

[2] N Severijns, M Tandecki, T Phalet, and IS Towner. ft values of the T= 1/2 mirror β transitions. *Physical Review C*, 78(5):055501, 2008.

[3] S Matsuura, S Umebayashi, C Okuyama, and K Oba. Current status of the micro channel plate. *IEEE Transactions on Nuclear Science*, 31(1):399–403, 1984.

[4] R Hong, A Leredde, Y Bagdasarova, X Fléchard, A García, P Müller, A Knecht, E Liénard, M Kossin, MG Sternberg, HE Swanson, and DW Zumwalt. High accuracy position response calibration method for a micro-channel plate ion detector. *Nuclear Instruments and Methods in Physics Research Section A: Accelerators, Spectrometers, Detectors and Associated Equipment*, 835:42–50, Nov 2016.

[5] V Chisté, M M Bé, C Dulieu, et al. Table of radionuclides (vol. 4-a= 133 to 252). *Bureau International Des Poids Et Mesures, Sfievres, France*, 2008.

[6] http://www.lnhb.fr/nuclear-data/.

[7] A Ceccucci. The ckm quark-mixing matrix. Lawrence Berkeley National Laboratory, 2008.

[8] M Kobayashi and T Maskawa. CP violation in the renormalizable theory of weak interaction. *Progress of theoretical physics*, 49(2):652–657, 1973.

[9] Y Ne'eman and Dj Šijački. Unified affine gauge theory of gravity and strong interactions with finite and infinite GL(4, R) spinor fields. *Annals of Physics*, 120(2):292–315, Aug 1979.

[10] G Arnison, A Astbury, B Aubert, C Bacci, G Bauer, A Bezaguet, R Bock, TJV Bowcock, M Calvetti, P Catz, et al. Further evidence for charged intermediate vector bosons at the SPS collider. *Physics Letters B*, 129(3-4):273–282, 1983.

[11] Y Nambu. Axial vector current conservation in weak interactions. *Physical Review Letters*, 4(7):380, 1960.

[12] P Delahaye, G Ban, M Benali, D. Durand, X Fabian, X Fléchard, M Herbane, E Liénard, F Mauger, A Méry, Y Merrer, O Naviliat-Cuncic, G Quéméner, B M Retailleau, D Rodriguez, J C Thomas, and P Ujic. The open LPC Paul trap for

precision measurements in beta decay. *The European Physical Journal A*, 55(6), Jun 2019.

[13] J C Hardy and I S Towner. Superallowed 0+→ 0+ nuclear β decays: A new survey with precision tests of the conserved vector current hypothesis and the standard model. *Physical Review C*, 79(5):055502, 2009.

[14] M B Schneider, F P Calaprice, A L Hallin, D W MacArthur, and D F Schreiber. Limit on Im($C_S C_A^*$) from a Test of T Invariance in ^{19}Ne Beta Decay. *Physical Review Letters*, 51(14):1239, 1983.

[15] K K Vos, H W Wilschut, and R G E Timmermans. Symmetry violations in nuclear and neutron β decay. *Rev. Mod. Phys.*, 87:1483–1516, Dec 2015.

[16] P Herczeg and I B Khriplovich. Time-reversal violation in decay in the standard model. *Physical Review D*, 56(1):80–89, Jul 1997.

[17] A Falkowski and A Rodríguez-Sánchez. On the sensitivity of the d parameter to new physics. *The European Physical Journal C*, 82(12):1134, 2022.

[18] H P Mumm, A Garcia, L Grout, M Howe, L P Parazzoli, et al. emiT: An apparatus to test time reversal invariance in polarized neutron decay. *Review of Scientific Instruments*, 75(12):5343–5355, Dec 2004.

[19] T E Chupp, R L Cooper, K P Coulter, S J Freedman, B K Fujikawa, A. García, G L Jones, H P Mumm, J S Nico, A K Thompson, C A Trull, F E Wietfeldt, and J F Wilkerson. Search for a-even triple correlation in neutron decay. *Physical Review C*, 86(3):035505, Sep 2012.

[20] F P Calaprice. The use of atomic beam and optical methods in the study of fundamental symmetries. *Hyperfine Interactions*, 22(1-4):83–93, Mar 1985.

[21] L Canetti, M Drewes, and M Shaposhnikov. Matter and antimatter in the universe. 14(9):095012.

[22] S Dodelson and L Knox. Dark energy and the cosmic microwave background radiation. *Physical Review Letters*, 84(16):3523, 2000.

[23] R B Partridge. *3K: the cosmic microwave background radiation*, volume 393. Cambridge University Press Cambridge, 1995.

[24] A Coc, E Vangioni-Flam, P Descouvemont, A Adahchour, and C Angulo. Updated big bang nucleosynthesis compared with Wilkinson Microwave Anisotropy Probe observations and the abundance of light elements. *The Astrophysical Journal*, 600(2):544, 2004.

[25] A D Sakharov. Violation of *CP* invariance, *C* asymmetry, and baryon asymmetry of the universe. 34(5):392–393.

[26] J M Cline. Baryogenesis. *arXiv preprint hep-ph/0609145*, 2006.

[27] S Staggs, J Dunkley, and L Page. Recent discoveries from the cosmic microwave background: a review of recent progress. *Reports on Progress in Physics*, 81(4):044901, 2018.

[28] G D Barr, P Buchholz, R Carosi, D Coward, D Cundy, N Doble, L Gatignon, V Gibson, P Grafström, R Hagelberg, et al. A New measurement of direct CP violation in the neutral kaon system. *Physics Letters B*, 317(1-2):233–242, 1993.

[29] G R Farrar and M E Shaposhnikov. Baryon asymmetry of the Universe in the standard model. *Physical Review D*, 50(2):774, 1994.

[30] A Yu Ignatiev, N V Krasnikov, V A Kuzmin, and A N Tavkhelidze. Universal CP-noninvariant superweak interaction and bayron asymmetry of the universe. *Physics Letters B*, 76(4):436–438, Jun 1978.

[31] K Kajantie, M Laine, et al. The electroweak phase transition: a non-perturbative analysis. *Nuclear Physics B*, 466(1-2):189–258, 1996.

[32] F J Gilman and Y Nir. Quark mixing: the CKM picture. *Annual Review of Nuclear and Particle Science*, 40(1):213–238, 1990.

[33] K Abe, N Akhlaq, R Akutsu, A Ali, C Alt, C Andreopoulos, M Antonova, S Aoki, T Arihara, Y Asada, et al. Improved constraints on neutrino mixing from the t2k experiment with 3.13$\times$ 10 21 protons on target. *Physical Review D*, 103(11):112008, 2021.

[34] M A Acero, P Adamson, L Aliaga, T Alion, V Allakhverdian, N Anfimov, A Antoshkin, Enrique Arrieta-Diaz, A Aurisano, A Back, et al. New constraints on oscillation parameters from ν e appearance and ν μ disappearance in the nova experiment. *Physical Review D*, 98(3):032012, 2018.

[35] B Aubert, D Boutigny, J-M Gaillard, A Hicheur, Y Karyotakis, J P Lees, P Robbe, V Tisserand, A Palano, G P Chen, et al. Observation of CP violation in the B0 meson system. *Physical review letters*, 87(9):091801, 2001.

[36] K Abe, R Abe, I Adachi, Byoung Sup Ahn, H Aihara, M Akatsu, G Alimonti, K Asai, M Asai, Y Asano, et al. Observation of large CP violation in the neutral B meson system. *Physical review letters*, 87(9):091802, 2001.

[37] A D SAKHAROV. VIOLATION OF CP-INVARIANCE, c-ASYMMETRY, AND BARYON ASYMMETRY OF THE UNIVERSE. In *In the Intermissions...*, pages 84–87. WORLD SCIENTIFIC, Nov 1998.

[38] C S Wu, E Ambler, R W Hayward, D D Hoppes, and R P Hudson. Experimental test of parity conservation in beta decay. *Physical review*, 105(4):1413, 1957.

[39] T D Lee and C N Yang. Question of parity conservation in weak interactions. *Physical Review*, 104(1):254–258, Oct 1956.

[40] J H Christenson, J W Cronin, V L Fitch, and R Turlay. Evidence for the 2π Decay of the K_2^0 Meson. *Phys. Rev. Lett.*, 13:138–140, Jul 1964.

[41] G C Branco, L Lavoura, and J P Silva. *CP violation*. Number 103. Oxford University Press, 1999.

[42] J D Jackson, S B Treiman, and H W Wyld. Coulomb corrections in allowed beta transitions. *Nuclear Physics*, 4:206–212, Aug 1957.

[43] X Fléchard, P Velten, E Liénard, A Méry, D Rodríguez, G Ban, D Durand, F Mauger, O Naviliat-Cuncic, and J C Thomas. Measurement of the β–ν correlation coefficient a$\beta\nu$ in the β decay of trapped $^{6}He^{+}$ ions. *Journal of Physics G: Nuclear and Particle Physics*, 38(5):055101, 2011.

[44] J A Behr and G Gwinner. Standard model tests with trapped radioactive atoms. *Journal of Physics G: Nuclear and Particle Physics*, 36(3):033101, 2009.

[45] V Vorobel, C Briançon, V Brudanin, V Egorov, J Deutsch, R Prieels, N Severijns, Y Shitov, C Vieu, T Vylov, et al. Beta-neutrino angular correlation in the decay of ^{14}O: Scalar coupling and interatomic interaction. *The European Physical Journal A-Hadrons and Nuclei*, 16:139–147, 2003.

[46] V Egorov, C Briançon, V Brudanin, J Dionisio, J Deutsch, V Gorozhankin, Y Gurov, R Prieels, V Sandukovsky, N Severijns, M Simoes, Yu Shitov, C Vieu, V Vorobel, T Vylov, I Yutlandov, and S Zaparov. Beta-neutrino angular correlation in the decay of ^{18}Ne. 621(3):745–753.

[47] E G Adelberger, C Ortiz, A García, H E Swanson, M Beck, O Tengblad, M J G Borge, I Martel, H Bichsel, and the ISOLDE Collaboration. Positron-Neutrino Correlation in the $0^{+} \rightarrow 0^{+}$ Decay of ^{32}Ar. *Phys. Rev. Lett.*, 83:1299–1302, Aug 1999.

[48] M G Sternberg, R Segel, N D Scielzo, G Savard, J A Clark, PF Bertone, F Buchinger, M Burkey, S Caldwell, A Chaudhuri, et al. Limit on tensor currents from ^{8}Li β decay. *Physical review letters*, 115(18):182501, 2015.

[49] Sternberg, M G and Segel, R and Scielzo, N D and Savard, G and Clark, J A and Bertone, P F and Buchinger, F and Burkey, M and Caldwell, S and others. Limit on Tensor Currents from ^{8}Li β Decay. *Phys. Rev. Lett.*, 115:182501, Oct 2015.

[50] N Severijns, M Beck, and O Naviliat-Cuncic. Tests of the standard electroweak model in nuclear beta decay. 78(3):991–1040.

[51] D Melconian, A Gorelov, M Trinczek, J M D'Auria, P Dubé, U Giesen, O Häusser, T Swanson, G Ball, J A Behr, et al. Detection system for a β^+-ν correlation experiment in a magneto-optical trap. In *APS Division of Nuclear Physics Meeting Abstracts*, pages F7–09, 1998.

[52] O Häusser and A Gorelov. Simulations of β^+-ν Correlation Experiments in ^{38m}K and ^{37}K . In *APS Division of Nuclear Physics Meeting Abstracts*, pages AD–11, 1997.

[53] E Lienard, G Ban, C Couratin, P Delahaye, D Durand, X Fabian, B Fabre, X Fléchard, Paul Finlay, F Mauger, et al. Precision measurements with lpctrap at ganil. *Hyperfine Interactions*, 236:1–7, 2015.

[54] X Fléchard, P Velten, E Liénard, A Méry, D Rodríguez, G Ban, D Durand, F Mauger, O Naviliat-Cuncic, and J C Thomas. Measurement of the β-ν correlation coefficient in the β decay of trapped $^{6}He^{+}$ ions. 38(5):055101.

[55] D Atanasov, F Cresto, L Nies, M Pomorski, M Versteegen, P Alfaurt, V Araujo-Escalona, P Ascher, B Blank, L Daudin, et al. Experimental setup for weak interaction studies with radioactive ion-beams WISArD. *Nuclear Instruments and Methods in Physics Research Section A: Accelerators, Spectrometers, Detectors and Associated Equipment*, page 168159, 2023.

[56] P Alfaurt, P Ascher, D Atanasov, B Blank, F Cresto, L Daudin, X Fléchard, M Gerbaux, J Giovinazzo, S Grévy, et al. WISArD: Weak Interaction Studies with ^{32} Ar Decay. *Particles and Nuclei*, 5:10, 2021.

[57] M Gonzalez-Alonso and O Naviliat-Cuncic. Kinematic sensitivity to the Fierz term of β-decay differential spectra. *Physical Review C*, 94(3):035503, 2016.

[58] M Kanafani, X Fléchard, O Naviliat-Cuncic, G D Chung, S Leblond, E Liénard, X Mougeot, et al. High-precision measurement of the he 6 half-life. *Physical Review C*, 106(4):045502, 2022.

[59] T Ohtsubo, S Roccia, N J Stone, J R Stone, C Gaulard, U Köster, J Nikolov, G S Simpson, and M Veskovic. The on-line low temperature nuclear orientation facility NICOLE. *Journal of Physics G: Nuclear and Particle Physics*, 44(4):044010, 2017.

[60] F Wauters, V De Leebeeck, I Kraev, M Tandecki, E Traykov, S Van Gorp, N Severijns, and D Zákouckỳ. β asymmetry parameter in the decay of ^{114}In. *Physical Review C*, 80(6):062501, 2009.

[61] B Fenker, J A Behr, D Melconian, R M A Anderson, M Anholm, D Ashery, R S Behling, I Cohen, I Craiciu, J M Donohue, et al. Precision measurement of the nuclear polarization in laser-cooled, optically pumped ^{37}K. *New Journal of Physics*, 18(7):073028, 2016.

[62] F Fang, D J Vieira, and X Zhao. Precision polarization measurements of atoms in a far-off-resonance optical dipole trap. *Physical Review A*, 83(1):013416, 2011.

[63] J A Behr and A Gorelov. β-decay angular correlations with neutral atom traps. *Journal of Physics G: Nuclear and Particle Physics*, 41(11):114005, 2014.

[64] K Blaum. High-accuracy mass spectrometry with stored ions. *physics Reports*, 425(1):1–78, 2006.

[65] G Bollen and S Schwarz. Ion traps for radioactive beam manipulation and precision experiments. *Nuclear Instruments and Methods in Physics Research Section B: Beam Interactions with Materials and Atoms*, 204:466–473, 2003.

[66] F Wauters, I Kraev, D Zákouckỳ, M Beck, M Breitenfeldt, V De Leebeeck, V V Golovko, V Yu Kozlov, T Phalet, S Roccia, et al. Precision measurements of the Co 60 β-asymmetry parameter in search for tensor currents in weak interactions. *Physical Review C*, 82(5):055502, 2010.

[67] G Soti, F Wauters, M Breitenfeldt, P Finlay, P Herzog, A Knecht, U Köster, I S Kraev, T Porobic, P N Prashanth, et al. Measurement of the β-asymmetry parameter of ^{67}Cu in search for tensor-type currents in the weak interaction. *Physical Review C*, 90(3):035502, 2014.

[68] B R Holstein. Precision frontier in semileptonic weak interactions theory. *Journal of Physics G: Nuclear and Particle Physics*, 41(11):114001, 2014.

[69] J Beringer, J F Arguin, R M Barnett, K Copic, O Dahl, D E Groom, C J Lin, J Lys, H Murayama, C G Wohl, et al. Review of particle physics. *Physical Review D*, 86(1), 2012.

[70] B Fenker, A Gorelov, D Melconian, J A Behr, M Anholm, D Ashery, R S Behling, I Cohen, I Craiciu, G Gwinner, et al. Precision Measurement of the β Asymmetry in Spin-Polarized ^{37}K Decay. *Physical Review Letters*, 120(6):062502, 2018.

[71] D Melconian, J A Behr, D Ashery, O Aviv, P G Bricault, M Dombsky, S Fostner, A Gorelov, S Gu, V Hanemaayer, K P Jackson, M R Pearson, and I Vollrath. *Physics Letters B*.

[72] M Kreuz, T Soldner, S Baeßler, B Brand, F Glück, U Mayer, D Mund, V Nesvizhevsky, A Petoukhov, C Plonka, et al. A measurement of the antineutrino asymmetry B in free neutron decay. *Physics Letters B*, 619(3-4):263–270, 2005.

[73] V Cirigliano, S Gardner, and B R Holstein. Beta decays and non-standard interactions in the LHC era. *Progress in Particle and Nuclear Physics*, 71:93–118, 2013.

[74] M González-Alonso and O Naviliat-Cuncic. Prospects for precision measurements in nuclear beta decay at the LHC era, 2013.

[75] P Delahaye, E Liénard, I Moore, M Benali, M L Bissell, L Canete, T Eronen, A Falkowski, X Fléchard, M Gonzalez-Alonso, W Gins, RP De Groote, A Jokinen, A Kankainen, M Kowalska, N Lecesne, R Leroy, Y Merrer, G Neyens, F De Oliveira Santos, G Quemener, A De Roubin, B-M Retailleau, T Roger, N Severijns, J C Thomas, K Turzo, and P Ujic. The MORA project. 2018.

[76] G Neyens, M Kowalska, D Yordanov, K Blaum, P Himpe, P Lievens, S Mallion, R Neugart, N Vermeulen, Y Utsuno, and T Otsuka. Measurement of the Spin and Magnetic Moment :Evidence for a Strongly Deformed Intruder Ground State. *Physical Review Letters*, 94(2):022501, Jan 2005.

[77] M Kowalska, DT Yordanov, K Blaum, P Himpe, P Lievens, S Mallion, R Neugart, G Neyens, and N Vermeulen. Nuclear ground-state spins and magnetic moments of ^{27}Mg, ^{29}Mg, and ^{31}Mg . *Physical Review C*, 77(3):034307, 2008.

[78] D Yordanov. *From ^{27}Mg to ^{33}Mg : transition to the Island of inversion*. Phd thesis, Leuven, 2007. Available at `https://cds.cern.ch/record/1476054`.

[79] I D Moore, P Dendooven, et al. The igisol technique—three decades of developments. *Three decades of research using IGISOL technique at the University of Jyväskylä: A Portrait of the Ion Guide Isotope Separator On-Line Facility in Jyväskylä*, pages 15–60, 2014.

[80] C G Callan and S B Treiman. Lower Bound on the decay rate for $\eta \to \mu^+ + \mu^-$. *Phys. Rev. Lett.*, 18:1083–1084, Jun 1967.

[81] P Herczeg. The T-Odd R and D correlations in beta decay. *Journal of Research of the National Institute of Standards and Technology*, 110(4):453, Jul 2005.

[82] C G Callan and S B Treiman. Electromagnetic simulation of T violation in beta decay. 162(5):1494–1496.

[83] S Ando, J A McGovern, and T Sato. The D coefficient in neutron beta decay in effective field theory. *Physics Letters B*, 677(1-2):109–115, Jun 2009.

[84] J C Brodine. Electromagnetic Final-State Interactions and Tests of Time-Reversal Invariance in Nuclear Beta Decay. *Physical Review D*, 1(1):100–106, Jan 1970.

[85] M Benali, G Quéméner, P Delahaye, X Fléchard, E Liénard, and BM Retailleau. Geometry optimisation of a transparent axisymmetric ion trap for the MORA project. *The European Physical Journal A*, 56(6):163, 2020.

[86] D H Wilkinson. The phoswich—a multiple phosphor. *Review of Scientific Instruments*, 23(8):414–417, Aug 1952.

[87] A Falkowski, M González-Alonso, and O Naviliat-Cuncic. Comprehensive analysis of beta decays within and beyond the Standard Model. *Journal of High Energy Physics*, 2021(4), Apr 2021.

[88] B Cheal, K Baczynska, J Billowes, et al. Laser Spectroscopy of Niobium Fission Fragments: First Use of Optical Pumping in an Ion Beam Cooler Buncher. *Physical Review Letters*, 102(22):222501, Jun 2009.

[89] Jürgen E, Giovanna M, Ferdinand S-K, and Rainer B. Laser cooling of trapped ions. *Journal of the Optical Society of America B*, 20(5):1003, May 2003.

[90] https://faster.in2p3.fr.

[91] http://faster.in2p3.fr/index.php/rhb.

[92] https://root.cern/.

[93] J L Wiza. Microchannel plate detectors. *Nuclear Instruments and Methods*, 162(1-3):587–601, Jun 1979.

[94] https://www.photonis.com/.

[95] Microchannel plates-rp photonics.https://www.rp-photonics.com.

[96] Microchannel plates-del mar photonics. http://dmphotonics.com.

[97] G A Feofilov, O I Stolyarov, F A Tsimbal, F F Valiev, and L I Vinogradov. Position-sensitive MCP-based detectors with high timing resolution: some results and perspectives. *Nuclear Instruments and Methods in Physics Research Section A: Accelerators, Spectrometers, Detectors and Associated Equipment*, 367(1-3):402–407, Dec 1995.

[98] https://simion.com/info/.

[99] N Severijns, L Hayen, V De Leebeeck, S Vanlangendonck, K Bodek, D Rozpedzik, and I S Towner. ft values of the mirror β transitions and the weak-magnetism-induced current in allowed nuclear β decay. *Physical Review C*, 107(1):015502, 2023.

[100] X Fléchard. Recoil Ion Momentum Spectroscopy in Atomic and Nuclear Physics: Applications to low energy ion-atom/molecule collisions and to β-ν angular correlation measurements in decay. 2012.

[101] G F Knoll. *Radiation Detection and Measurement, 3rd ed.* John Wiley and Sons, New York, 3rd edition edition, 2000.

[102] U Fano. On the theory of ionization yield of radiations in different substances. *Physical Review*, 70(1-2):44, 1946.

[103] U Fano. Ionization yield of radiations. II. The fluctuations of the number of ions. *Physical Review*, 72(1):26, 1947.

[104] https://www.mesytec.com/products/nuclear-physics/mpr-16l.html.

[105] https://physics.nist.gov/physrefdata/star/text/estar.html.

[106] A Singh. *Metrological study of the shape of beta spectra and experimental validation of theoretical models*. Phd thesis, 09 2020.

[107] I D Moore, T Eronen, D Gorelov, J Hakala, A Jokinen, A Kankainen, V S Kolhinen, J Koponen, H Penttilä, I Pohjalainen, et al. Towards commissioning the new IGISOL-4 facility. *Nuclear Instruments and Methods in Physics Research Section B: Beam Interactions with Materials and Atoms*, 317:208–213, 2013.

[108] E Kugler. The ISOLDE facility. *Hyperfine interactions*, 129(1-4):23–42, 2000.